Experimental investigation of particle concentration profiles in a turbulent channel flow

by

Saqeeb Islam

A thesis submitted in partial fulfillment of the requirements for the degree of

Master of Science

Department of Mechanical Engineering
University of Alberta

Abstract

The purpose of this thesis is to obtain a better understanding of the behavior of particles within a particle-laden turbulent channel flow, as well as evaluate the suitability of the flow facility to measure particle-laden flows. Suitability of the flow loop for measurements of particle-laden flows is determined by whether there is significant error in the loops ability to produce a consistent flow field. Particle-laden flows are prevalent across many industries, and so knowing how the particles act within the flow can aid in increasing process accuracy and efficiency. For this thesis the target of analysis is the concentration profile of the particles in the flow, and how the profile varies with Stokes number. To start, the streamwise and wall-normal velocity profiles for the unladen flow were measured using particle image velocimetry at Reynolds numbers starting from 10 000 up to 80 000. The velocity profiles were measured at the midplane of the channel, as well as at 30mm and 45mm offsets from the midplane in both spanwise directions of the channel, and finally at a midplane location upstream of the test section. These velocity profiles were plotted against the channel height and were used to evaluate the flow conditions with respect to the existing literature. This study examined the concentration profiles of three different types of spherical particles; 420µm polystyrene particles (Stokes numbers from 0.218 to 1.74), 420µm glass particles (Stokes numbers of 0.549 to 4.39), and 1.2mm polystyrene particles (Stokes numbers from 1.86 to 14.9). The polystyrene particles were approximately neutrally buoyant, while the glass particles have a density of approximately 2511 kg/m^3. For all particle types, multiple particle concentrations were considered across the same Reynolds numbers as the unladen flow. Observations at the channel midplane for the 420µm glass particles show a general trend that most of the particles accumulate near the bottom of the channel even as the Stokes number is increased. This is contrary to the 420µm polystyrene particles. For all Stokes numbers these particles demonstrate a core-peaking

profile for low concentrations and an upper wall peak for the higher 0.5% concentration. Lastly, the 1.2mm particles also show a similar trend at all Stokes numbers, with the plots showing a core peaking profile at lower concentrations, and an upper wall-peaking profile as the concentration is increased.

In addition to the measurements at the channel midplane, the concentration profiles for the 420μm polystyrene particles were also measured at 30mm and 45mm offset locations in each spanwise direction, at a concentration of 0.1%. The observations generally show a core peaking profile as well in the positive spanwise direction, but a wall-peaking profile in the negative spanwise direction for all Stokes numbers, indicating some variation in the particles detected along the spanwise direction. Finally, the 1.2mm particles were measured at the midplane of the test section, as well as a section further upstream. In the test section, for most concentrations, the concentration profile peak moves towards the top of the channel as the Stokes number is increased. At the upstream channel location, for a concentration of 0.1% the concentration profiles were consistently flatter for all Stokes numbers. These observations indicate that the flow loop is suitable for particle laden flow measurements, and the results obtained here are consistent with other observations discussed in various literature.

Preface

The studies conducted for this thesis were completed under the supervision of Dr. Sina Ghaemi from the Department of Mechanical Engineering at the University of Alberta.

The polystyrene particles used in this experiment were obtained from the Saskatchewan Research Council.

The code used for the detection of particles in the images was developed by Dr. Sina Ghaemi using MATLAB.

Instructions on the proper operating procedures of the flow facility, as well as the plotting and formatting of figures and graphs were assisted by the direction of Lucas Warwaruk.

Acknowledgements

First, I would like to thank Dr. Sina Ghaemi for letting me work under his guidance for this degree. He has been an excellent teacher and mentor and has pushed me to learn great things both about this subject as well as myself.

Second, I would like to extend my thanks to Lucas Warwaruk. His guidance with learning the operations of the flow facility were crucial for the data I collected.

Finally, I want to thank my parents. It is their persistence and support that pushed me to work hard and complete this thesis. Their steadfast belief in me is what helped me get through to the end.

Table of Contents

Abstract ii

Preface iv

Acknowledgements v

Table of Contents vi

List of Tables ix

Table of Figures x

Chapter 1. Introduction 1

Chapter 2. Literature Review 5

2.1 Turbulent Channel Flow 5

2.1.1 Mass and Momentum Equations for Turbulent Channel flow 5

2.1.2 Fully Developed Turbulent Channel Flow 12

2.1.3 Reynolds Shear Stress 15

2.1.4 Zones of turbulent wall flows 16

2.1.5 Derivation of friction law for channel flow 19

2.2 Particle Laden Flows 22

2.2.1 Investigations of particle laden flows 24

Chapter 3. Experimental Setup 30

3.1 Horizontal Channel Flow 30

3.2 Particle Laden Flow 37

3.3 Particle Image Velocimetry 41

3.4 Particle Tracking Velocimetry 46

Chapter 4. Unladen Flow 53

4.1 Friction Factor 53

4.2 Mean Velocity Profile 57

Chapter 5. Particle Laden Flows 68

5.1. Particle Distributions 68

5.1.1. 420μm Polystyrene Particles 69

5.1.2. 1.2mm Polystyrene Particles 72

5.1.3. 420μm Glass Particles 76

5.1.4. Effect of Measurement Location 80

5.1.5. Channel Upstream 85

5.2. Particle Laden Velocity Profiles 88

5.2.1. 420μm Polystyrene Particles 90

5.2.2. 1.2mm Polystyrene Particles 91

5.2.3. 420μm Glass Particles 93

5.2.4. Effect of Measurement Location 95

5.2.5. Channel Upstream 97

5.2.6. Wall-Normal Velocity Profiles 99

Chapter 6. Conclusion 107

Future Work 110

References 111

List of Tables

Table 1: Summary of studies related to particle laden flows. 29

Table 2: A table summarizing the particle parameters that were used for this experiment. 40

Table 3: Stokes numbers for particles considered in this experiment. 41

Table 4: Stokes numbers for tracer particles at each Reynolds Number. 42

Table 5: Bulk flow velocities at their respective Reynolds numbers..... 60

List of Figures

Figure 1: An isometric view of the rectangular test section. 6

Figure 2: The different sublayers displayed in a turbulent channel flow. 19

Figure 3: A schematic of the flow loop used in these experiments, Ahmadi et al (2020). 31

Figure 4: A zoomed in schematic of the test section with coordinate system labelled. 37

Figure 5: An image showing the optical setup used to capture images. 43

Figure 6: (a) Raw image file captured with camera. (b) Detected particles after being processed with MATLAB code. 48

Figure 7: A schematic outlining the laser sheet positions for the different fields of view used to capture images. 51

Figure 8: A schematic indicating the position of the upstream channel laser sheet. 52

Figure 9: A plot showing the calculated friction factor as a function of Reynolds number for various unladen flow tests, with lines for Dean's correlation and the friction factor for channel flow shown for comparison. 57

Figure 10: The streamwise velocity profiles for the (a) Midplane, (b) +0.25*b*, (c) +0.375*b*, (d) -0.25*b*, (e) -0.375*b* laser positions along the *z*-axis, (f) and the channel upstream position. 59

Figure 11: The normalized streamwise velocity profiles of the unladen flow at a *Re* = 10 000. . 61

Figure 12: The normalized streamwise velocity profiles of the unladen flow at a *Re* = 40 000. . 61

Figure 13: The normalized streamwise velocity profiles of the unladen flow at a *Re* = 70 000. . 62

Figure 14: The normalized streamwise velocity profiles for the test section midplane and channel upstream midplane locations at *Re* = 10 000. 64

Figure 15: The normalized streamwise velocity profiles for the test section midplane and channel upstream midplane locations at *Re* = 40 000. 64

Figure 16: The normalized streamwise velocity profiles for the test section midplane and channel upstream midplane locations at *Re* = 70 000. 65

Figure 17: The wall-normal velocity profiles for the (a) midplane, (b) +0.25*b*, (c) +0.375*b*, (d) -0.25*b*, (e) -0.375*b* laser sheet locations along the *z*-axis, (f) and the upstream position. 67

Figure 18: The 420µm particle distribution plots. 71

Figure 19: The normalized 420µm particle distribution plots. 72

Figure 20: The 1.2mm particle distribution plots. 75

Figure 21: The normalized 1.2mm particle distribution plots. 76

Figure 22: The 420µm glass particle distribution plots. 79

Figure 23: The normalized 420µm glass particle distribution plots. 80

Figure 24: The 420µm particle distribution plots with the laser pointing from the top. 84

Figure 25: The normalized 420µm particle distribution plots with the laser pointing from the top. 85

Figure 26: The particle distribution plot for the upstream channel section. 87

Figure 27: The normalized particle distribution plot for the upstream channel section. 88

Figure 28: The streamwise velocity profiles for the 420µm particle case. 91

Figure 29: The streamwise velocity profiles for the 1.2mm particle case. 93

Figure 30: The streamwise velocity profiles for the 420µm glass particle case. 95

Figure 31: The streamwise velocity profiles for the 420µm particle case with the offset laser sheet positions. 97

Figure 32: The streamwise velocity profiles of the upstream channel section. 98

Figure 33: The wall-normal velocity profiles for the 420µm particle case. 101

Figure 34: The wall-normal velocity profiles for the 1.2mm particle case. 102

Figure 35: The wall-normal velocity profiles for the 420µm glass particle case. 103

Figure 36: The wall-normal velocity profiles for the 420µm particle case with the offset laser sheet positions. 105

Figure 37: The wall-normal velocity profiles for the channel upstream section. 106

Chapter 1. Introduction

Particle laden flows are prominent in many industrial applications. One such industry where this is prevalent is the oil sands mining industry, a key contributor to the Albertan economy. This process is used to extract bitumen, which is refined to be used for a variety of things ranging from gasoline in cars, to jet fuel, to everyday cosmetic products. The bitumen that is mined from the ground is mixed with sand and thus needs to be processed. To transport the bitumen-sand mixture, water is added to the mixture in the transport pipeline to aid in pumping the bitumen to a processing facility. This instance of particle laden flows is what this thesis aims to study. Understanding the behavior of the particles in the flow can help with increasing the efficiency of the transport. An example of how this might be affected is that the impacts of the particles in the flow with the walls of the pipe can lead to erosion of the pipeline (Dai et al. 2018). If the erosion in the pipe becomes too severe, it may threaten the integrity of the pipeline, and would eventually cause a structural failure of the pipe. Understanding the distribution of the particles in the flow can aid in determining how the pipe integrity would be affected.

The properties of the particles themselves within the flow can have an affect on the behavior of the flow. Some of these properties are particle size, shape, density, and concentration among others. Most of the transport pipelines used in the oil and gas industry are oriented horizontally, which means that the flow is perpendicular to the flow of gravity. In horizontal turbulent pipe or channel flows, the effect of gravity pulling particles down counteracts the turbulent eddies that cause the particles to move away from the direction of gravity, which is mentioned in Ahmadi et al (2020). Based on these factors, the concentration profile across the height of the channel may vary, which could influence the transport of the fluid. Another effect described in Ahmadi et al (2020) is the effect of particle-wall lubrication, which is a phenomenon that occurs in the near wall

region. As particles move towards the wall, they experience a repulsive force due to the increase in pressure between the particle and the wall. Particles moving away from the wall feel an attractive force back towards the wall caused by the decrease of pressure between the particle and the wall. This effect coupled with inter-particle collisions in the near wall vicinity causes the particles to group up near the wall, creating a concentration peak close to the wall.

Previous investigations have examined concentration profiles for different particle sizes and densities. One such example is Zade et al. (2018) which examined neutrally buoyant particles in both Newtonian and viscoelastic fluids. Their observations for Newtonian flows show a gradual core-peaking profile at low particle concentrations, with the peak increasing as the concentration increases. However, at higher concentrations, a smaller peak starts to form in the near wall vicinity, indicating an accumulation of particles which could be due to the particle wall lubrication. Fong et al. (2019) examined the behavior of heavier glass particles in a vertical channel where the flow was downwards, along the direction of gravity. In this study, the particles were shown to have a wall-peaking concentration profile, with the maximum concentration at the wall being significantly higher than the mean concentration across the channel and note that the peak at the wall is within the viscous sublayer. Both examples show the importance of understanding the behaviour of particles within particle laden flows and demonstrates how the concentration profile can vary based on particle properties.

The purpose of this thesis is to investigate the behaviour of different types of particles in particle laden flows at various concentrations. In addition to particle concentrations, multiple Reynolds numbers were also measured to observe the particle behaviour at different velocity regimes. Previous studies have investigated different particle types as well as different concentrations of a specific particle type. This study aims to combine both variables and observe the behaviour of

particle laden flows with variations of both the particle type and concentration. Additionally, another goal of this thesis is to evaluate the suitability of the flow loop facility to obtain accurate measurements of particle laden flows. The suitability of the flow loop will be determined by whether the flow loop apparatus and the measurement system can obtain accurate and consistent data of the turbulent particle laden flow. To evaluate this, the concentration profiles should be consistent with existing literature, indicating that the neutrally buoyant particles should be distributed evenly across the channel, whereas the glass particles should exhibit a wall peaking profile. If the error in the measurements is significant, meaning that the concentration profiles are not recorded accurately or consistently, then it will be determined that the flow loop is not suitable for measurements of particle-laden flows. In the rectangular channel section measurements for the velocity profile and the particle concentration profiles were taken at various locations to characterize the flow in as many places as possible. These different locations include the midplane of the channel, offset locations from the midplane along the width of the channel, as well as a location directly following the transition region where the loop changes from a pipe flow to a channel flow. Evaluating these measurements along with the existing literature are intended to determine if the flow in the loop is being measured accurately. All these locations are discussed in further detail in Chapter 3.

The topics of each chapter in this thesis are briefly described in the following list:

Chapter 2. Literature Review: This chapter describes the fundamental principles which dictate the behaviour of turbulent flows and particle laden flows. It describes the behaviour of the flow within a channel and includes a derivation for the friction factor of a channel flow. At the end of the section studies conducted by other authors which explore particle laden flows are investigated.

Chapter 3. Experimental Setup: This chapter describes the experimental apparatus used to conduct measurements for this experiment. In addition to the description, figures are also included to show a 3-D model of the flow loop used to conduct the experiment, as well as detailed figures of the test section, where the measurements were taken. Also included is an uncertainty analysis for the values measured in the experiment, along with a detailed description of the imaging apparatus used to calculate the unladen velocity profiles.

Chapter 4. Unladen Flows: This chapter consists of measurements conducted on the unladen flow. These include plots for the friction factor in the channel, as well as the streamwise and wall normal velocity profiles in the test section for the various Reynolds numbers. The velocity profile plots are intended to be used as a baseline to be compared to the particle laden flows.

Chapter 5. Particle Laden Flows: Finally, in this chapter the measurements conducted with the various particles in the turbulent flow are discussed in two sections. The first section examines the particle concentration profiles and the other section examines the velocity profiles of the particles in the fluid. Each of those sections are further subdivided into the different particle types, where each particle type has multiple plots for the various particle concentrations considered in each case.

Chapter 6. Conclusion: This chapter summarizes the observations made in this experiment, and what conclusions can be derived from this thesis. It also briefly discusses potential avenues for future work to expand on the experiments.

Chapter 2. Literature Review

This section establishes the fundamental aspects regarding the subject of this thesis. The first section outlines some of the physics related to turbulent channel flow. Next, the second section provides a description of particle laden flows, and some examples of how they have been studied previously. Lastly, the final section explores different observation and data collection methods found in the literature.

2.1 Turbulent Channel Flow

Turbulent flows exist in many different forms and permeate all aspects of our lives from complicated engineering applications, to flows found in nature itself. As such, investigating turbulent flows is vital to understanding how to develop better engineering technologies. Kundu et al., (2012) defines turbulence very plainly as "a dissipative flow state characterized by nonlinear fluctuating three-dimensional vorticity." These fluctuations can exist in the form of velocity, pressure, and temperature fluctuations. Because of the chaotic nature of turbulent flows, it is difficult to predict them analytically, and so often experimental procedures are undertaken to try to understand these flows.

2.1.1 Mass and Momentum Equations for Turbulent Channel flow

As previously stated, there are many different forms of turbulent flows that may be of interest. For engineering purposes, it is often beneficial to try to understand and analyze the turbulent behavior of flow in channels, as many modern-day engineering processes require the use of transporting multiphase flows, such as the transport in slurry pipelines. Rectangular channels, such as those used for heating and cooling are of particular interest because they have certain advantages when compared against a pipe. In addition to a reduced cost for manufacturing and installing, they also

take up less space due to the cross-section shape, Cengel and Cimbala (2014). For a rectangular channel, the cartesian coordinates x, y, and z are used. Figure 1 below is a schematic of a rectangular channel like the one used in this experiment along with the coordinate system defined for the derivations of the equations of motion.

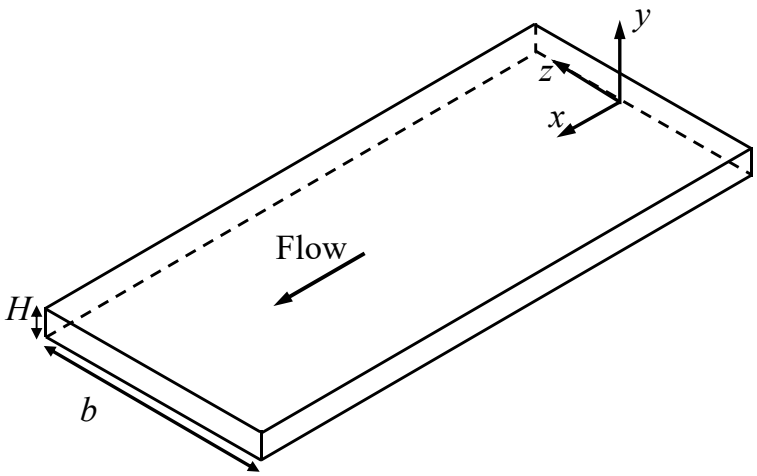

Figure 1: An isometric view of the rectangular test section.

In Figure 1 H represents the channel height and b represents the channel width. The coordinate system defined is as follows; the x-coordinate is in the direction of flow (streamwise), the y-coordinate is the direction normal to the wall (wall normal), and the z-coordinate is along the width of the channel (spanwise). Of note the y-coordinate starts from the bottom wall of the channel, which is how figures in the following sections will be oriented. To analyze the flow inside of a channel, experiments are focused on the fully developed region of flow in the channel. As the flow enters the channel, the boundary conditions imposed by the walls alters the flow. This region is known as the flow development region. In this region, the flow velocity profile varies in the direction of the flow. After this region, the flow does not vary in the streamwise direction anymore, therefore it is fully developed. In terms of mathematics, fully developed means that the derivative

of the velocity with respect to the streamwise direction, in this case the x-direction, is 0. In other words, $\partial/\partial x = 0$. Additionally, for channels with an aspect ratio of $b/H \gg 1$ the side walls of the channel have little impact on the flow statistics (Pope 2000). Studies by Knight and Patel (1985) tested aspect ratios ranging from 1 to 10 and showed that an aspect ratio of at least 5 is required to reduce the effects of the shear force acting on the side walls. Rhodes and Knight (1994) tested much larger aspect ratios, ranging from 15 to 50, which also show a decrease in the percentage of shear force acting on the walls as the aspect ratio is increased. By minimizing the effect of the side walls, the derivative of the velocity in the z-coordinate can also be considered 0, which can be shown as $\partial/\partial z = 0$. The result of these two assumptions is that the flow is only a function of y, making it a one-dimensional flow which can be expressed as $U = f(y)$, where U is the velocity field. A common parameter used to define turbulent flows is the Reynolds Number, which can be described as the ratio of inertial forces divided by the viscous forces of the fluid. This equation is given as

$$Re = \frac{\rho \bar{U} H}{\mu}, \tag{1}$$

where ρ is the fluid density, $\bar{U}$ is the bulk velocity, which is the average velocity across the channel height, and μ is the dynamic viscosity of the fluid. For a turbulent flow, the Reynolds Number must be greater than 1800, although the transitional regime does not have a static boundary so some transitional effects may still be present for Reynolds Numbers slightly higher than this.

One key equation when characterizing turbulent flows is the continuity equation, obtained from conservation of mass, which is derived as

$$\frac{\partial \rho}{\partial t} + \nabla \cdot \left(\rho \vec{U}\right) = 0. \tag{2}$$

The velocity vector $\vec{U}$ consists of three different components. These components are *U*, *V*, and *W* shown in equation 3, and they represent the components of the velocity vector in the *x*, *y,* and *z* directions, respectively. Furthermore, the equation can be simplified by assuming that the fluid is incompressible. This eliminates the first term in the equation which includes the density, and the remaining velocity vector is shown with its cartesian components to be,

$$\frac{\partial U}{\partial x} + \frac{\partial V}{\partial y} + \frac{\partial W}{\partial z} = 0. \tag{3}$$

Characterizing turbulent flows at higher Reynolds numbers is difficult because of the various length and time scales that require resolution. In most cases, understanding the average of the whole turbulent flow is needed. To do this, the continuity equation for the mean flow can be derived. To obtain this, the velocities are decomposed into their mean and fluctuating components, and then time averaged, Kundu (2012). This process is called Reynolds decomposition. For example, the instantaneous streamwise velocity *U* can be broken up as shown below,

$$U(x,t) = \langle U(x,t) \rangle + u'(x,t). \tag{4}$$

Where the term in the angled brackets, ⟨ ⟩, indicate the mean component, and the lowercase letter with the apostrophe indicates the fluctuating component. This decomposition applied to all three terms of the continuity equation is shown as

$$\frac{\langle U \rangle}{\partial x} + \frac{\partial u'}{\partial x} + \frac{\partial \langle V \rangle}{\partial y} + \frac{\partial v'}{\partial y} + \frac{\partial \langle W \rangle}{\partial z} + \frac{\partial w'}{\partial z} = 0. \tag{5}$$

The whole equation is then time averaged. Time-averaged values of the fluctuating components are equal to zero, while the time-averaged values of the mean components stay the same. This simplifies the equation and results in the continuity equation for the mean flow shown as

$$\frac{\partial \langle U \rangle}{\partial x} + \frac{\partial \langle V \rangle}{\partial y} + \frac{\partial \langle W \rangle}{\partial z} = 0. \tag{6}$$

Now the equation can be further simplified by applying certain assumptions. First, that the flow is fully developed, meaning that there is no variation in the flow along the *x*-direction, so that $\partial/\partial x = 0$. The next assumption is that there is no flow in the *z* direction, such that $\langle W \rangle = 0$. Using these assumptions, the continuity equation simplifies to

$$\frac{\partial \langle V \rangle}{\partial y} = 0. \tag{7}$$

From this relationship it is shown that our velocity field $\vec{U}$, is a function of *y* and only *y*.

To further understand the behavior of the fluid, Newton's second law is applied to a material element of the fluid. This gives the equation,

$$\sum \vec{F} = m\vec{a} = m\frac{D\vec{U}}{Dt} = \rho dxdydz\frac{D\vec{U}}{Dt} \tag{8}$$

where the arrows denote vectors. The summation of forces includes both body and surface forces. When looking at a control volume of dimensions *dx·dy·dz* of the fluid, the body forces are

$$\sum F_{x,body} = \sum F_{x,gravity} = \rho g_x dxdydz. \tag{9}$$

And the surface forces on the control volume are

$$\sum F_{x,surface} = \left(\frac{\partial}{\partial x}\sigma_{xx} + \frac{\partial}{\partial y}\sigma_{yx} + \frac{\partial}{\partial x}\sigma_{zx}\right) dxdydz. \tag{10}$$

Substituting these into Newton's second law, and dividing out *dxdydz* yields the momentum equation, also known as Cauchy's equation.

$$\rho\frac{D\vec{U}}{Dt} = \rho\vec{g} + \vec{\nabla}\cdot\sigma_{ij}. \tag{11}$$

This equation is not particularly useful as the stress tensor term σ_{ij} contains nine components, of which six are unknown. Fortunately, Cauchy's equation can be simplified further by assuming that the flow is incompressible and isothermal. Assuming in incompressible flow again means that the density is considered constant. Also, in this experiment, the only fluid being considered is a

Newtonian fluid, which means that the fluid stress is linearly proportional to the fluid strain, and thus the viscous stress tensor is linearly proportional to the strain rate tensor. This linear relationship is shown as

$$\tau_{ij} = 2\mu\varepsilon_{ij}. \tag{12}$$

Here τ_{ij} is the viscous stress tensor and ε_{ij} is the strain rate tensor. For a fluid in motion, the viscous stress tensor is related to the stress tensor by the relationship shown in Equation 13 as

$$\sigma_{ij} = \begin{pmatrix} \sigma_{xx} & \sigma_{xy} & \sigma_{xz} \\ \sigma_{yx} & \sigma_{yy} & \sigma_{yz} \\ \sigma_{zx} & \sigma_{zy} & \sigma_{zz} \end{pmatrix} = \begin{pmatrix} -P & 0 & 0 \\ 0 & -P & 0 \\ 0 & 0 & -P \end{pmatrix} + \begin{pmatrix} \tau_{xx} & \tau_{xy} & \tau_{xz} \\ \tau_{yx} & \tau_{yy} & \tau_{yz} \\ \tau_{zx} & \tau_{zy} & \tau_{zz} \end{pmatrix}. \tag{13}$$

While this does not reduce the number of unknowns in the equations, it relates the stress tensor term with the pressure field. By substituting the term for the viscous stress tensor, the stress tensor term written in cartesian coordinates becomes

$$\sigma_{ij} = \begin{pmatrix} -P & 0 & 0 \\ 0 & -P & 0 \\ 0 & 0 & -P \end{pmatrix} + \begin{pmatrix} 2\mu\dfrac{\partial U}{\partial x} & \mu\left(\dfrac{\partial U}{\partial y} + \dfrac{\partial V}{\partial x}\right) & \mu\left(\dfrac{\partial U}{\partial z} + \dfrac{\partial W}{\partial x}\right) \\ \mu\left(\dfrac{\partial V}{\partial x} + \dfrac{\partial U}{\partial y}\right) & 2\mu\dfrac{\partial V}{\partial y} & \mu\left(\dfrac{\partial V}{\partial z} + \dfrac{\partial W}{\partial y}\right) \\ \mu\left(\dfrac{\partial W}{\partial x} + \dfrac{\partial U}{\partial z}\right) & \mu\left(\dfrac{\partial W}{\partial y} + \dfrac{\partial V}{\partial z}\right) & 2\mu\dfrac{\partial W}{\partial z} \end{pmatrix}. \tag{14}$$

Next the Cartesian components in equation 14 can be substituted into Cauchy's equation in equation 11, with the corresponding Cartesian components. The obtained equations are the Navier-Stokes equations, derived as

$$\rho\frac{D\vec{U}}{Dt} = -\vec{\nabla}P + \rho\vec{g} + \mu\nabla^2\vec{U}. \tag{15}$$

The Navier-Stokes equations can describe the instantaneous behavior of the fluid flow. For turbulent flows, the time-averaged quantities are of interest. The same process of Reynolds

decomposition can be applied to the Naver-Stokes equations. By applying Reynolds decomposition to the Navier-Stokes equations and simplifying the mean value of the fluctuating component to be zero, a new set of equations is obtained, known as the Reynolds-Averaged Navier-Stokes equations (RANS) shown in equation 16 as

$$\frac{\bar{D}\langle U_j\rangle}{\bar{D}t} = \nu\nabla^2\langle U_j\rangle - \frac{\partial\langle u_i{'}u_j{'}\rangle}{\partial x_i} - \frac{1}{\rho}\frac{\partial\langle P\rangle}{\partial x_j}. \tag{16}$$

The variable ν is the kinematic viscosity, which is equal to $\nu = \frac{\mu}{\rho}$, the dynamic viscosity divided by the density of the fluid, and $\langle P\rangle$ is the mean component of the pressure term. Notably, the RANS equations are nearly identical to the Navier-Stokes equations. The only difference is the addition of the $\langle u_i{'}u_j{'}\rangle$ term, which is known as the Reynolds Stress. The Reynolds stresses are stresses that are a result of the fluctuating velocity field in a turbulent flow. The Reynolds stress will be discussed in further detail in the next section.

First it is useful to look at the expanded RANS equation in the *y*-direction.

$$\left(\frac{\partial\langle V\rangle}{\partial t} + \langle U\rangle\frac{\partial\langle V\rangle}{\partial x} + \langle V\rangle\frac{\partial\langle V\rangle}{\partial y} + \langle W\rangle\frac{\partial\langle V\rangle}{\partial z}\right) \tag{17}$$

$$= -\left(\frac{\partial\langle u'v'\rangle}{\partial x} + \frac{\partial\langle v'^2\rangle}{\partial y} + \frac{\partial\langle v'w'\rangle}{\partial z}\right) - \frac{1}{\rho}\frac{\partial\langle P\rangle}{\partial y}$$

$$+ \nu\left(\frac{\partial^2\langle V\rangle}{\partial x^2} + \frac{\partial^2\langle V\rangle}{\partial y^2} + \frac{\partial^2\langle V\rangle}{\partial z^2}\right).$$

Additionally, the RANS equation in the x-direction is shown as

$$\left(\frac{\partial\langle U\rangle}{\partial t}+\langle U\rangle\frac{\partial\langle U\rangle}{\partial x}+\langle V\rangle\frac{\partial\langle U\rangle}{\partial y}+\langle W\rangle\frac{\partial\langle U\rangle}{\partial z}\right) \tag{18}$$

$$=-\left(\frac{\partial\langle u'^2\rangle}{\partial x}-\frac{\partial\langle u'v'\rangle}{\partial y}-\frac{\partial\langle u'w'\rangle}{\partial z}\right)-\frac{1}{\rho}\frac{\partial\langle P\rangle}{\partial x}$$

$$+\nu\left(\frac{\partial^2\langle U\rangle}{\partial x^2}+\frac{\partial^2\langle U\rangle}{\partial y^2}+\frac{\partial^2\langle U\rangle}{\partial z^2}\right).$$

These equations can be further simplified for a fully developed turbulent channel flow to obtain equations describing the flow characteristics. These derivations are conducted in the following section.

2.1.2 Fully Developed Turbulent Channel Flow

The RANS equations can be simplified by making some assumptions about the flow. These assumptions are that the fully developed flow is steady, two-dimensional, meaning there is no variation of the flow in the *z*-direction, and there is only a pressure gradient in the direction of the flow. Starting with the RANS equation in the *y*-direction, with these assumptions the equation reduces to

$$0=-\frac{\partial\langle v'^2\rangle}{\partial y}-\frac{1}{\rho}\frac{\partial\langle P\rangle}{\partial y}. \tag{19}$$

By taking the integral of this equation across the half channel height, the obtained equation is

$$\langle v'^2\rangle\Big|_{y=H/2}-\langle v'^2\rangle\Big|_{y=0}=\frac{1}{\rho}\langle P\rangle\Big|_{y=0}-\frac{1}{\rho}\langle P\rangle\Big|_{y=H/2}. \tag{20}$$

This can be further simplified to

$$\langle v'^2\rangle+\frac{\langle P\rangle}{\rho}=\frac{\langle P_w\rangle}{\rho}, \tag{21}$$

where $\langle P_w \rangle$ represents the pressure at the wall where y=0. The other terms in the expression are at the location where $y = {}^{H}/_{2}$, as the value of $\langle v'^2 \rangle$ at the wall is zero. If this equation is then differentiated by the x-coordinate, the equation becomes

$$\frac{\partial \langle P \rangle}{dx} = \frac{\partial \langle P \rangle_w}{dx}. \tag{22}$$

This indicates that the streamwise pressure gradient at the wall is equal to the streamwise pressure gradient away from the wall, and thus is constant across the height of the channel in the y-direction. This relationship now be used in the simplification for the RANS equation in the x-direction. Using the same assumptions as before, the RANS equation in the x-direction can be reduced to the following equation.

$$0 = -\frac{\partial \langle u'v' \rangle}{\partial y} - \frac{1}{\rho}\frac{\partial \langle P \rangle}{\partial x} + \nu \frac{\partial^2 \langle U \rangle}{\partial y^2}. \tag{23}$$

To solve this equation, we again start with integrating it across the half channel height as the channel is symmetrical, and then apply boundary conditions for the variables. From this the obtained equation is

$$constant = -\rho \langle u'v' \rangle \Big|_{0}^{H/2} - \frac{\partial \langle P \rangle}{\partial x} y \Big|_{0}^{H/2} + \rho \nu \frac{\partial \langle U \rangle}{dy} \Big|_{0}^{H/2}. \tag{24}$$

At the channel centerline where $y = H/2$, the first boundary condition is that the total shear stress is equal to zero. The total shear stress is given in the equation

$$\tau = \rho \nu \frac{d\langle U \rangle}{dy} - \rho \langle u'v' \rangle = 0. \tag{25}$$

This eliminates two terms from the integrated equation, leaving only the pressure term and the constant shown as

$$constant = -y\frac{\partial\langle P\rangle}{\partial x}\bigg|_{H/2} = -\frac{H}{2}\frac{\partial\langle P\rangle_w}{\partial x}. \tag{26}$$

Next the boundary condition at the wall is applied. At the wall y=0 which eliminates the pressure term, and the Reynolds shear stress is zero due to the no-slip boundary condition. The resulting simplified equation is

$$constant = \mu\frac{\partial\langle U\rangle}{\partial y}. \tag{27}$$

The term on the right is the wall shear stress, which means that the constant can be written as τ_w. This means that equation 27 can be written as

$$\tau_w = -\frac{H}{2}\frac{\partial\langle P\rangle_w}{\partial x}. \tag{28}$$

However, it was derived in equation 22 that the pressure gradient at the wall is equal to the pressure gradient at any point away from the wall. This means that the wall-shear stress can be calculated in terms of the streamwise pressure gradient at any point along the channel, resulting in the final equation below

$$\tau_w = -\frac{H}{2}\frac{\partial\langle P\rangle}{\partial x}. \tag{29}$$

In addition to the wall-shear stress, it is important to define some more terms relating to the near wall region. Because viscous forces dominate near the wall, it is useful to define velocity and length scales for the near-wall region. These variables are the friction velocity and viscous length scale. The friction velocity is defined as

$$u_\tau = \sqrt{\frac{\tau_w}{\rho}}, \tag{30}$$

and the viscous length scale is

$$\delta_\nu = \nu\sqrt{\frac{\rho}{\tau_w}} = \frac{\nu}{u_\tau}. \tag{31}$$

Wall units define a distance from the wall in terms of viscous lengths, and are defined by

$$y^+ = \frac{y}{\delta_\nu} = \frac{yu_\tau}{\nu}. \tag{32}$$

These wall units will be used in a later section to define sublayers of the velocity profile near the wall, which exhibit different properties.

2.1.3 Reynolds Shear Stress

As stated in the previous section, Reynolds stresses put simply are average stresses that result from the turbulent behavior of a flow. These stresses can also be understood as the mean momentum transfer that is caused by the turbulent fluctuations. The Reynolds stresses can be derived by Reynolds Averaging the momentum equation. This process is briefly outlined in the previous section and shows that this process produces an additional term known as the Reynolds Stress Tensor, $\langle u_i u_j \rangle$, shown below as

$$-\langle u'v' \rangle = -\begin{pmatrix} \langle u'^2 \rangle & \langle u'v' \rangle & \langle u'w' \rangle \\ \langle u'v' \rangle & \langle v'^2 \rangle & \langle v'w' \rangle \\ \langle u'w' \rangle & \langle v'w' \rangle & \langle w'^2 \rangle \end{pmatrix}. \tag{33}$$

The diagonal components of the tensor describe the normal stresses, and the non-diagonal components describe the shear stresses. Most of the time, the Reynolds stresses are much larger than the viscous stresses. The exception occurs at the wall, where viscous stresses dominate and Reynolds stresses approach zero.

2.1.4 Zones of turbulent wall flows

When examining the velocity profile of a turbulent flow in a channel, one observation is that, like a laminar flow, the velocity profile is parabolic. Unlike laminar flows however, the slope of the turbulent velocity profile is much shallower, with a steep drop near the wall. The turbulent behavior in the region near the wall is divided into different layers based on the distance from the wall and is known as the law of the wall. The equation for the law of the wall is derived in (Pope 2000) as

$$u^+ = f_w(y^+), \tag{34}$$

where

$$f_w(y^+) = \int_0^{y^+} \frac{1}{y}\Phi_1(y)\,dy. \tag{35}$$

The variable u^+ is the nondimensionalized velocity, defined as

$$u^+ = \frac{\langle U \rangle}{u_\tau}, \tag{36}$$

which is the mean velocity normalized by the friction velocity. In these equations, Φ_1 is the universal function for the velocity gradient of a channel flow and y^+ is the distance from the wall normalized by a viscous length scale δ_v defined in the previous section as

$$\delta_v = \nu\sqrt{\frac{\rho}{\tau_w}} = \frac{\nu}{u_\tau}. \tag{37}$$

Viscous Sublayer

The viscous sublayer is a small region of an internal flow close to the wall. Within this region, the viscosity is the dominant factor that contributes to the shear stress. Subsequently, the Reynolds

stresses in this region are very small. The reason for this is because the wall eliminates the velocity component normal to the wall. At very high velocities (high Re), the viscous sublayer becomes very small. The result of the sublayer being very thin means that the viscous stresses can be approximated with the wall shear stress, and it is uniform over the sublayer. An expression for the wall shear stress can be shown as

$$\frac{\tau_w}{\rho} = \frac{\nu u}{y}. \tag{38}$$

As stated previously, the square root of the term τ_w/ρ is known as the friction velocity. With this, it can be shown that the velocity profile in this case is linear. This linear profile for the viscous sublayer is shown to be valid for $y^+ < 5$. Wall units were defined in the Reynolds Stresses section. The value of $y^+ < 5$ was determined empirically through experiments. With the no-slip condition, the law of the wall for the viscous sublayer can be shown in a normalized form as

$$u^+ = y^+, \tag{39}$$

which is a linear relationship.

Buffer Layer

The region outside of the viscous sublayer is known as the buffer layer. This layer is defined for wall units $5 < y^+ < 30$. This region is further from the wall, and thus viscous stresses are less prominent than the viscous sublayer. However, they are not negligible. Both Reynolds stresses and viscous stresses need to be considered in this region. Turbulence production is at a maximum in this region.

Log Layer (Overlap Layer)

Through experimental analysis, the velocity in the log layer was found to be proportional to the logarithm of the distance from the wall. As y^+ increases, the effect of viscosity becomes less

prominent. For the layer outside of the buffer layer, the fluid viscosity has little effect. Therefore, when considering the viscous terms in the law of the wall equation, the value of Φ_1 from the law of the wall is a constant. This yields an average velocity gradient of

$$\frac{du^+}{dy^+} = \frac{1}{\kappa y^+}. \tag{40}$$

Integrating yields the result of the nondimensionalized velocity,

$$u^+ = \frac{1}{\kappa} \ln y^+ + B. \tag{41}$$

This is known as the logarithmic law. Both κ and B are constants. K more specifically is called the von Kàrmàn constant. They are determined experimentally to be approximately

$$\kappa = 0.41 \; and \; B = 0.52. \tag{42}$$

Through experimental observation, the logarithmic law has been shown to be very accurate for $y^+ > 30$. This is useful because it can accurately describe the velocity profile in all areas aside from just near the wall, or near a pipe center for pipe flows. Because of this, the logarithmic law is called the universal velocity profile in turbulent pipe flows or turbulent flow over a surface. Figure 2 below displays the sublayers in a cross section of turbulent channel flow.

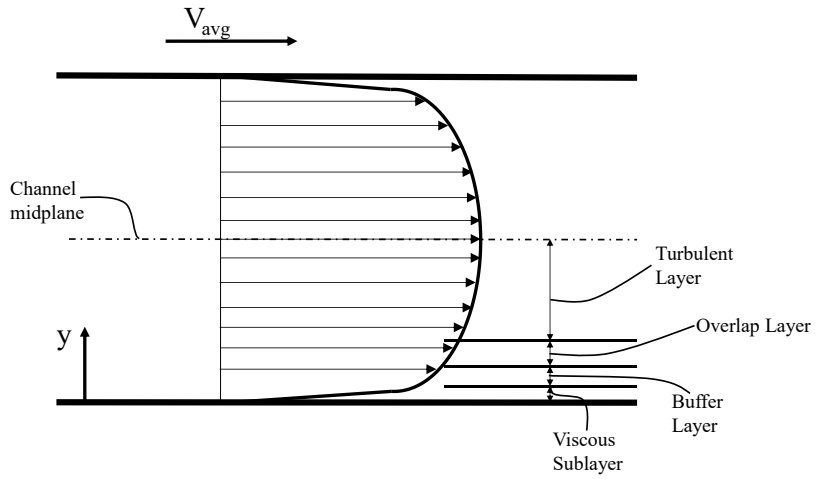

Figure 2: The different sublayers displayed in a turbulent channel flow.

2.1.5 Derivation of friction law for channel flow

The friction factor in a channel represents the pressure loss in the channel that results from interactions of the fluid with the channel. For turbulent pipe flows, Prandtl's friction law for pipes is a well-established equation used to estimate the friction factor. A similar process can be applied to derive the friction law equation for channel flows. This process starts by assuming that the mean velocity profile can be approximated over the entire channel using the log law outlined above. This equation, when normalized with the friction velocity is

$$\frac{\langle U \rangle}{u_\tau} = \frac{1}{\kappa} \ln y^+ + B. \tag{43}$$

The bulk velocity is given as the integral of the mean velocity over the height of the channel. Since the channel flow is symmetric, the integration can be taken from the wall up to the half-channel height, denoted as $H/2$ for this derivation. Substituting the equation for y^+ from equation 32 into equation 43 yields

$$\frac{\bar{U}}{u_\tau} = \frac{1}{H/2}\int_0^{\frac{H}{2}} \frac{1}{\kappa}\ln\left(\frac{yu_\tau}{\nu}\right)dy + B. \tag{44}$$

Using integration by parts, the integral is simplified to

$$\frac{\bar{U}}{u_\tau} = \frac{1}{H/2\,\kappa}\left[y\ln\left(\frac{yu_\tau}{\nu}\right)\Bigg|_0^{\frac{H}{2}} - \int_0^{\frac{H}{2}} dy\right] + B. \tag{45}$$

By integrating the second term, and factoring out *H/2* the equation simplifies to

$$\frac{\bar{U}}{u_\tau} = \frac{1}{\kappa}\left[\ln\left(\frac{Hu_\tau}{2\nu}\right) - 1\right] + B. \tag{46}$$

Next, the friction factor for a channel flow, based on the wall shear stress is given as

$$f = \frac{\Delta PH}{2L\frac{1}{2}\rho\bar{U}^2} = \frac{\Delta PH}{L\rho\bar{U}^2}. \tag{47}$$

From the previously derived RANS equations, a relationship for the wall-shear stress and the streamwise pressure gradient was obtained, shown in equation 29. A relationship for the friction velocity is also shown previously in equation 30. By substituting these two equations into equation 47, a relationship for the friction factor as a function of the bulk and friction velocities is obtained, which is expressed as

$$\frac{\bar{U}}{u_\tau} = \sqrt{\frac{2}{f}}. \tag{48}$$

This ratio can be set equal to equation 47 to obtain an equation for the friction factor of a channel flow that is in a form analogous to Prandtl's friction law, shown as

$$\sqrt{\frac{2}{f}} = \frac{1}{\kappa}\left[\ln\left(\frac{\delta u_\tau}{\nu}\right) - 1\right] + B. \tag{49}$$

Now all that is left to do are some mathematical simplifications. The factor of the square root of two is divided on both sides to obtain the equation in the form

$$\frac{1}{\sqrt{f}} = \frac{1}{\sqrt{2}\kappa}\left[\ln\left(\frac{\delta \bar{U}\sqrt{f}}{\nu\sqrt{2}}\right) - 1\right] + \frac{B}{\sqrt{2}}. \tag{50}$$

The Reynolds number for a channel flow is defined over the total channel height, 2δ, so the expression inside of the natural logarithm needs to be multiplied by a factor of $\frac{2}{2}$ which gives

$$\frac{1}{\sqrt{f}} = \frac{1}{\sqrt{2}\kappa}\left[\ln\left(\frac{2\delta \bar{U}\sqrt{f}}{\nu 2\sqrt{2}}\right) - 1\right] + \frac{B}{\sqrt{2}}. \tag{51}$$

Now the equation can be simplified to be expressed in terms of friction factor and Reynolds number, as well as the constants κ, the Von Karman constant, and B. This simplified equation is shown as

$$\frac{1}{\sqrt{f}} = \frac{1}{\sqrt{2}\kappa}\left[\ln\left(\frac{Re\sqrt{f}}{2\sqrt{2}}\right) - 1\right] + \frac{B}{\sqrt{2}}. \tag{52}$$

Finally, the expression inside of the natural logarithm can be simplified using mathematical rules to obtain the final equation,

$$\frac{1}{\sqrt{f}} = \frac{1}{\sqrt{2}\kappa}\left[\ln\left(Re\sqrt{f}\right) - \ln 2\sqrt{2} - 1\right] + \frac{B}{\sqrt{2}}. \tag{53}$$

Values of κ and B are not exact, as they are obtained experimentally and thus can assume a range of values. For this case, values of 0.41 and 5.2 have been assumed respectively (Pope 2000). Replacing these values and simplifying, the equation comes down to

$$\frac{1}{\sqrt{f}} = 1.72\ln\left(Re\sqrt{f}\right) + 0.159. \tag{54}$$

2.2 Particle Laden Flows

This experiment aims to examine the behavior of particles dispersed within a fluid flow, and how they react under different flow conditions. The type of flow in question is then referred to as a multiphase flow, and in this case the components, or phases, are the particles and the fluid containing them. Multiphase flows are present both in nature and in several industrial processes which makes understanding them crucial for engineering applications. The particles are known as the disperse phase, while the fluid containing them, in this case water, is called the continuous phase. There are several parameters that are used to characterize the behavior of particles in a multiphase flow. One of the most crucial parameters is the dimensionless Stokes number of the particle, defined as

$$St = \frac{\tau_p}{\tau_f}, \tag{55}$$

where τ_p is the particle response time and τ_f is the fluid response time, as stated in Aggarwal et al. (1994). The fluid response time represents the time required for changes to occur within the fluid, and the particle response time is the time required for the particle to react to the changes in the fluid. This means that if the Stokes number is much smaller than one, the particle reacts very quickly to changes in the flow, and thus closely follows the motion of the fluid, such as particles of smoke or dust in air. On the other hand, if the Stokes number is much larger than one, the particle does not react to the changes in the fluid fast enough, and so moves without the fluid. An example of this would be something like a heavy lead ball sinking in water, dominated by inertial forces or body forces like gravity and not the motion of the water around it. When considering a turbulent flow, multiple time scales are present as there is a wide range of eddy sizes present in the flow, which makes calculating the fluid response time τ_f a bit more complicated. In the range

of the largest eddies in the flow, the time scale considered is the integral time scale ($\tau_{f,\Lambda}$), and the smallest time scale when considering the smallest eddies is called the Kolmogorov time scale ($\tau_{f,\lambda}$). A Stokes number larger than one indicates that the motion of the particle is not greatly influenced by changes in the fluid flow and is instead dominated by body forces such as gravity. When a Stokes number smaller than one means that the movement of the particle is more greatly affected by changes in the fluid, and so it follows the flow closely.

Another important parameter is the dimensionless particle diameter, denoted in Ahmadi et al (2020) as d_p^+ and described as the equation

$$d_p^+ = \frac{d_p u_\tau}{\nu_f}, \tag{56}$$

where d_p is the particle diameter, u_τ is the friction velocity, and ν_f is the kinematic viscosity of the fluid. The dimensionless diameter helps express the magnitude of the particle diameter relative to other dimensional systems.

When considering the behavior of the particles themselves in the fluid, there are several factors at play. In a horizontal channel the most obvious is that of the force of gravity on particles. This effect is counteracted by turbulent suspension caused by the motion of the fluid, can be represented by the Rouse number. The Rouse number, P, is given as

$$P = {}^{v_s}/_{\kappa u_\tau}, \tag{57}$$

where v_s is the settling velocity, κ is the von Karman constant, and u_τ is the friction velocity. Particles within the flow will be fully suspended if the Rouse number is below 1.2, Ahmadi et al (2020). Another mechanism that affects particle distribution in the channel is particle-wall lubrication, which can cause particles to accumulate in the near wall region. Described in Picano et al (2015), particle layers form adjacent to the wall. This layer creates a local maximum in the particle concentration profile. As the overall concentration is increased, the magnitude of the local

maximum near the wall also increases, an observation also noted in Baker and Coletti (2019). This local peak was also observed to never exceed the magnitude of the bulk concentration in the channel. This accumulation occurs because as a particle moves closer to the wall, there is an increase in pressure in the region between the particle and the wall, creating a force of repulsion. Conversely, as a particle moves away from the wall, the pressure drops which creates a force of attraction. Picano et al (2015) states that these effects coupled with inter-particle collisions in the near wall region confines particles close to the wall, making it difficult for particles in this layer to move away from it. In certain vertical pipe flows, particles have been observed to preferentially accumulate near the channel center, such as in Shokri et al. (2017). This experiment observed glass particles dispersed in water flowing vertically upward, against gravity. The force of gravity pulling on the particles causes them to slow down and have a smaller velocity relative to the continuous phase. In the region away from the walls, this slip velocity contributes to a lift force which pushes particles towards the pipe centerline, resulting in a core peaking concentration profile. As a result, this transport mechanism is called shear-induced lift force and has been observed in both experimental studies and well as in numerical simulations.

2.2.1 Investigations of particle laden flows

Many studies have been conducted to better understand turbulent particle laden flows, which will be briefly explored here. There are many factors which can affect the turbulence of a particle laden flow, most of which are related to the properties of the particles. Some examples of these are the size, shape, concentration, and density of the particles. Changes in these properties can result in variations of the drag in the fluid, as well as the velocity fluctuations and the Reynolds Stresses. Some of these variations were observed by Gillessen et al. (2013), where a volume fraction of 0.125 of neutrally buoyant particles were studied in a Couette flow, with a Reynolds number of

approximately 13,300. They observed that in the far wall region (close to the channel center) the streamwise velocity fluctuations were augmented while the spanwise and wall-normal velocity fluctuations were attenuated. The inverse was true close to the wall; the streamwise fluctuations were attenuated and the spanwise and wall-normal fluctuations were augmented. This change is indicative of drag reduction, but they note that in contrast with polymer-induced drag reduction, the reduction here originates in the logarithmic region of the boundary layer, and that the drag is increased within the buffer layer.

Other studies look at the distribution of particles across the height of the channel, and how the distribution changes based on varying flow parameters, or particle characteristics, such as the study conducted by Fong et al. (2019). Their experiment looked at the behavior of glass spheres with a mean diameter of 50μm flowing through air in a vertical channel. The particles are injected at the top of the channel through a series of screens to ensure they are uniformly distributed throughout the flow. The test section is located at the bottom, with the channel above it being sufficiently long to allow the particles to achieve terminal velocity at approximately the halfway point from when the particles are released to the point where they enter the test section. Fong et al. (2019) notes that this flow orientation is of particular interest because of the potential effect that gravity can have on the behaviour of the particles and the flow. For their measurements, they divided the particles into a high Stokes number case, and a low Stokes number case. These cases were each then further divided into a low volume fraction case as well as a high-volume fraction case. From their observations, both Stokes number cases showed a peak of the particle concentration close to the channel wall, indicating a wall-peaking concentration profile. For both Stokes number cases, the high-volume fraction case showed a larger magnitude of particle concentration close to the wall compared to the low volume fraction case. The high and low volume fraction profiles cross at

location approximately equal to $y/H = 0.2$, such that the low volume fraction case creates a local maximum value at the channel centerline. This peak is smaller in magnitude compared to the peak at the wall, but it is still higher than the high-volume fraction case at the channel center, which levels off and remains flat. An argument of why the low volume fraction case behaves this way is that turbophoresis, the tendency of particles to accumulate near the wall, is driven by the wall normal r.m.s. (root mean square) velocity gradient as is observed by Young and Leeming (1997). The study by Young and Leeming (1997) derives a mathematical solution that relates the turbophoretic force to the gradient of the wall normal turbulence intensity. Fong et al (2019) affirms this by comparing the plot of the particle concentration with the plot for the wall normal r.m.s. velocity gradient. They note that the concentration follows the same shape as the r.m.s gradient plot. The concentration is a maximum at the wall, and drops off sharply within the visocus sublayer, and rises more gradually near the channel center. The same is true for the r.m.s. gradient, it is very sharp near the channel wall, and much shallower at the channel center. These concentration profiles were also compared against numerous other one-way coupled and two-way coupled direct numerical simulations. For both cases, the DNS studies found results like what they observed for their low volume fraction case with a small peak at the centerline. For the two-way coupled simulations however, this centerline peak was observed for an increased mass loading of particles.

In Ahmadi et al (2020) the behavior of glass beads at varying concentrations and Reynolds numbers were examined in a horizontal channel flow, like the experiment conducted in this paper. Their experiment looked at several factors, including the spatial distribution of the particles along the wall-normal direction of the channel. A total of three bulk concentrations were examined (0.05%, 0.15%, 0.27%) at three different Reynolds Numbers (20 200, 40 400, 60 500). From the

normalized distribution plots, a wall-peaking profile is observed across all concentrations for the Reynolds number case of 20 200, with the distribution decreasing towards the center of the channel. As the Reynolds number was increased to 40 400, the 0.05% concentration case displayed a bimodal distribution. This means that there was a concentration peak observed near the channel wall, then as the profile moves away from the wall the concentration starts decreasing before increasing again further away from the wall. On the contrary, the 0.15% and 0.27% cases start with a peak close to the wall, and steadily decreases to a minimum as the profile moved away from the wall. This same general trend is also observed for these concentrations at the Reynolds number of 60 500. Ahmadi (2020) state that these near wall peaks may be a result of particle-wall lubrication, which causes the wall-peaking concentration profile.

Another study by Zade et al (2018) looked at the behavior of spherical particles in both Newtonian fluids and drag reducing viscoelastic fluids. For a direct comparison with this experiment only observations in the Newtonian fluid are described. Their experiment involved neutrally buoyant hydrogel spheres flowing in a duct flow. The size of the particles is 5 ± 0.8mm and the concentrations considered were 5, 10, 15, and 20%. Plots of the particle concentration profiles were shown as a function of the wall-normal coordinate of the duct, normalized by the half channel height. From their observations at a Reynolds Number of approximately 11 000 the concentration profiles show that as the particle concentration is increased, the particles tend towards the core of the duct. At the lowest concentration of 5% the profile is relatively constant across the height of the duct, with the concentration approaching zero near the wall. However, at the concentration of 20% there is a distinct increase and maximum in the concentration profile at the core region. This magnitude of concentration increase near the core region correlates with the increase in the overall concentration of particles. What is also interesting is that at all concentration profiles of 10% and

above, a distinct local maximum at a wall-normal position of approximately $^{y}/_{H} = 0.1$ is also present. This local maximum indicates a layer of particles that accumulates near the bottom wall of the channel, creating a dual-peaking concentration profile. Zade et al (2018) reason that this preferential concentration of particles near the core could be due to either inertial shear induced migration or an imbalance in the wall-normal stresses.

This dual-peak concentration profile is also observed in a direct numerical simulation (DNS) study by Fornari et al (2016). This experiment looked at particle concentrations of 0.2%, 2%, 5%, and 20%, and particle density ratios including 1, 2, 4, and 10, defined as the particle density divided by the fluid density. For the set of measurements examining the concentration profiles, the mass fraction was held constant. The mass fraction χ, is defined as $\chi = \phi R$, where ϕ is the particle concentration and R is the density ratio. As the mass fraction was set constant at 0.2, as the concentration increased, the density ratio must also have decreased. From their observations it is shown that for all density ratios above 1 and concentrations above 0.2% there is a region near the bottom wall of the channel at approximately $y = 0.1$ where particles accumulate and create a local maximum in the concentration profile. The concentration profile then dips slightly as it moves away from the wall to produce a local minimum in the profile before eventually increasing to a maximum value at the channel centerline. This trend is present for particle concentrations of 2%, 5%, and 20%, and the magnitude of the local maximum peak relative to the local minimum trough increases with the increasing particle concentration. Relating to this, the profile for the 0.2% concentration case is almost flat, with the difference in the magnitude of the local maximum and local minimum near the channel wall being almost negligible.

Table 1 below summarizes the main points observed in each of the papers discussed in this section. While these various studies examine different types of particles and Reynolds numbers, they also

mostly only look at only on type or size of particles. Of course, the particle properties play an important role in determining their behavior on the flow, as well as their effect on the flow itself. Therefore, it is also useful to compare different particle types among each other to help determine how each of them behave in similar conditions. The focus of this study aims to examine how particle behavior differs based on size and density and compare them to one another. Table 1 summarizes the main components of the papers previously discussed. The nomenclature in the table is defined as: ρ_p is the particle density, ρ is the fluid density, d_p is the particle diameter, a is the particle radius, H is the full channel height, and h is the half channel height.

Table 1: Summary of studies related to particle laden flows.

Paper	Fong et al (2019)	Ahmadi et al (2020)	Zade et al (2018)	Fornari et al (2016)
Concentration Profile Shape	Wall-peaking	Wall-peaking	Dual peaking	Dual peaking
Type of Study	Experimental	Experimental	Experimental	DNS
Particle Density	ρ_p = 2500 kg m^{-3}	ρ_p = 2600 kg m^{-3}	$\rho_p/\rho = 1$	${}^{\rho_p}/_{\rho_f} = 1, 10, 1000$
Particle Size	d_p = 50µm	d_p = 210µm	$H/d_p = 10$	$a/h = 1/18$
Particle Size Normalized	d_p^+ = 0.78, 1.1	d_p^+ = 14.6, 27.6, 40.3	d_p^+ = 32.4	d_p^+ = 10
Stokes Numbers	St = 6.7, 11.5	St = 0.8, 1.4, 1.9	St = 6.1	St = 0.9, 8.8, 883

Chapter 3. Experimental Setup

This section outlines the experimental apparatus used to conduct the measurements. All the experiments conducted for this study used a horizontal slurry flow loop located in the Mechanical Engineering Building at the University of Alberta campus. 2D Particle tracking Velocimetry (2D-PTV) was used to track the motion of particles in the flow, and 2D Particle Image Velocimetry (2D-PIV) was used to determine the characteristics of the unladen flow. In addition to descriptions and schematics of the flow loop, this section also outlines the optical setup used to capture images of the flow, as well as a description of the code used to detect the particles in the images.

3.1 Horizontal Channel Flow

The apparatus consists of a channel flow loop with a visible test section, and a PTV/PIV imaging setup. The flow loop consists primarily of 2-inch inner diameter pipe comprised of PVC and stainless steel at varying locations, which are connected to an LCC-M 50-230 centrifugal pump from GIW Industries, and a mixing tank located directly upstream of the pump. Water as well as the particles are first introduced the tank before being fed into the flow loop. Removing air bubbles from the loop is essential to ensure accurate collection of data, thus the setup can be run in both open loop and closed loop configurations. When the flow loop is in open loop configuration, the water is stopped by a valve and directed up into the tank, which then feeds back into the loop downstream of the valve. Running in open loop configuration allows for the air inside of the loop to dissipate at the open surface inside the tank, as well as allow any particles that are added into the tank to sufficiently mix throughout the loop. Closed loop configuration consists of having the valve open to allow the water to bypass the tank, and flow solely through the loop only. A schematic of the flow loop is shown in Figure 3, which is the same schematic as the one used in

Ahmadi et al (2020). The process of adding the particles into the loop starts with adding the particles and water into the tank, then running the loop in open loop configuration for a short amount of time. Once it is seen visually that most of the bubbles have dissipated, the loop is switched to closed loop configuration. Any remaining air bubbles in the loop can still dissipate through the tank to the open surface as the valve below the tank, connecting back to the loop remains open.

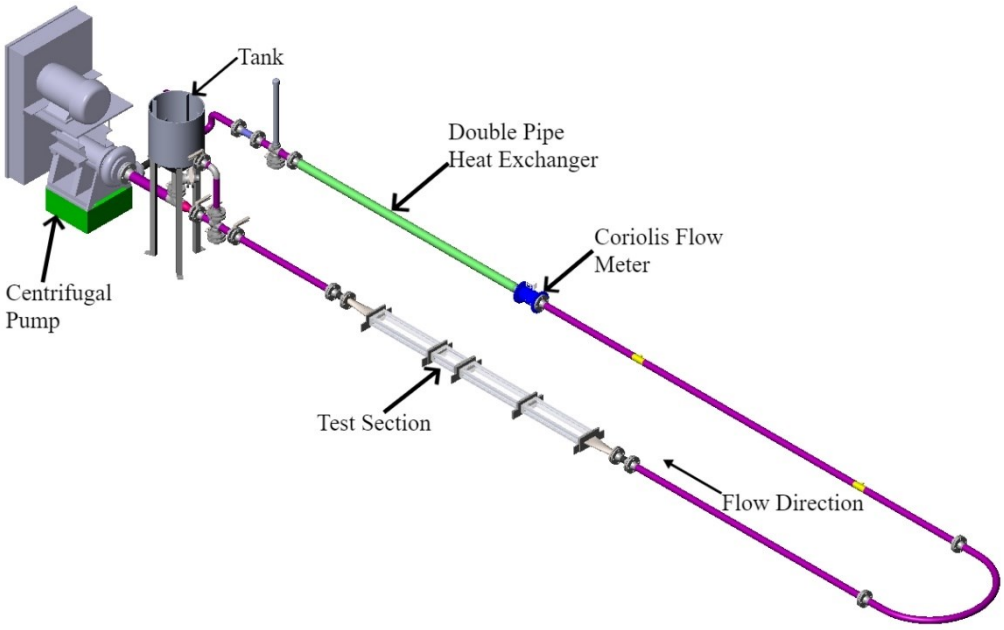

Figure 3: A schematic of the flow loop used in these experiments, Ahmadi et al (2020).

The rectangular channel section of the loop is comprised primarily of acrylic panels, while only the test section walls are comprised of glass panels reinforced with a steel frame. Having glass panels allows for better quality when viewing the flow from both the spanwise and wall-normal directions, as well as having less interference for the laser when forming a laser sheet. The test section makes up a small portion of the overall rectangular channel, having dimensions of $120\times15mm^2$ for the width and height, respectively, located at 1.65m downstream from the transition point of the circular pipe to rectangular channel. It is here where all the images of the

flow were captured. Another transition section is located downstream of the test section as well to go back to the circular pipe cross section. The 1.65m distance before the test section consists of two acrylic sections from the transition point and is required to ensure that the flow is fully developed by the time it reaches the test section. The entrance region required for the flow becomes fully developed is determined by the expression

$$\frac{L}{H} > 50 - 100, \tag{58}$$

where L is the length of channel before the test section, and H is the total height of the channel. In this experiment L is equal to 1.65m and H is equal to 0.015m, which results in a ratio of 110. This means that the length given to allow the flow to become fully developed is sufficient as the ratio is greater than the minimum value of 50. Each acrylic section adjacent to the test section has a pressure port in them, which are connected to a Validyne DP-15 pressure transducer with a 2-psi diaphragm. Once the loop is filled with water, the pressure transducer can be vented to remove any air that may be trapped in the tubes connecting it to the pressure ports. Removing the air from these tubes is important as having air within the tubes can introduce uncertainty into the pressure measurements. This pressure difference between the two tubes is recorded by the LabVIEW software as the pressure drop across the test section.

One section of the flow loop located upstream of the test section is covered by a jacket, which forms a double pipe heat exchanger that allows for the regulation of the temperature of water within the loop. For the experiments conducted in this study the temperature was held at approximately 25±0.3°C for all measurements. Directly downstream from the heat exchanger is an Emerson Micro Motion F200S Coriolis flow meter which measures the mass flow rate and temperature of the fluid inside of the pipes. The temperature measured by the Coriolis flow meter is supplementary to the temperature probe further downstream, which is what reads temperature

data and sends it to be recorded in the LabVIEW software. Finally, there is an air inlet valve with can blow pressurized air through the loop to assist in draining and cleaning the loop once one set of experiments are done.

Achievable Reynolds numbers within the loop can reach upwards of 100,000. Cengel and Cimbala (2014) define the Reynolds number as the ratio of the inertial forces divided by the viscous forces of the fluid. Turbulent flows have a high velocity, which means that the inertial forces dominate the flow, which allows more random fluctuations to occur in the flow. Conversely, in laminar flows the viscous forces are larger compared to the inertial, meaning that the turbulent fluctuations are suppressed, resulting in a more uniform flow. The equation for the Reynolds number based on the mass flow rate $\dot{m}$, dynamic viscosity μ, and channel width b, is shown in equation 59 below as

$$Re = \frac{\dot{m}}{\mu b}. \tag{59}$$

Knowing the uncertainty of the Reynolds number is useful to judge the accuracy of the results. Calculating the uncertainty interval of the Reynolds number can be done through the method of propagation of uncertainty and determining the uncertainty of each variable used to calculate Reynolds number and substituting them into the equation

$$\varepsilon_{Re} = \pm\left[\left(\frac{\dot{m}}{Re}\frac{\partial Re}{\partial \dot{m}}\varepsilon_{\dot{m}}\right)^2 + \left(\frac{\mu}{Re}\frac{\partial Re}{\partial \mu}\varepsilon_{\mu}\right)^2 + \left(\frac{b}{Re}\frac{\partial Re}{\partial b}\varepsilon_{b}\right)^2\right]^{\frac{1}{2}}. \tag{60}$$

In this equation, the variables $\varepsilon_{\dot{m}}$, ε_{μ}, ε_{b}, and ε_{Re} are the uncertainties for the mass flow rate, dynamic viscosity, channel width and Reynolds number respectively.

To start, the mass flow rate is measured by the Emerson Coriolis Flow Meter, which gives an uncertainty from the manufacturer of ±0.20%. The width measurement is accurate to the nearest half of a millimeter, giving an uncertainty of ±0.25mm. By dividing this value by the channel width, the uncertainty interval of the width can be determined, shown in equation 61,

$$\varepsilon_b = \pm\frac{0.25mm}{120mm} = \pm 0.002083\ or\ \pm 0.2083\%. \tag{61}$$

Next, the uncertainty of the dynamic viscosity needs to be determined. Because the dynamic viscosity varies with temperature, the uncertainty of the temperature is also required to obtain the uncertainty for the dynamic viscosity, which can be estimated by the equation

$$\varepsilon_{\mu(T)} = \pm\frac{\delta\mu}{\mu} = \frac{1}{\mu}\frac{d\mu}{dT}(\pm\delta T). \tag{62}$$

The thermocouple within the flow meter gives a temperature uncertainty of ±1°C. For the experiments in this paper, the temperature was held at 25°C, which gives a temperature range of 24°C-26°C. Using this range, the derivative in equation 62 can be calculated, shown in the equation below as

$$\begin{aligned}\frac{d\mu}{dT} &= \frac{\mu(26°C) - \mu(24°C)}{(26-24)°C} = \frac{0.0008693\frac{Ns}{m^2} - 0.0009096\frac{Ns}{m^2}}{2°C} \\ &= -2.015\times10^{-5}\frac{Ns}{m^{2}°C}.\end{aligned} \tag{63}$$

Now using this value, the uncertainty interval for the dynamic viscosity caused by the uncertainty of the temperature is also determined using the equation shown as

$$\begin{aligned}\varepsilon_{\mu(T)} &= \frac{1}{0.0008891\frac{Ns}{m^2}}\times\left(-2.015\times10^{-5}\frac{Ns}{m^{2}°C}\right)\times\pm1°C \\ &= \pm 0.02266\ or\ \pm 2.27\%.\end{aligned} \tag{64}$$

In addition to the temperature, the tabulated values of viscosity have some uncertainty as well, which can be assumed to be approximately ±1% as well. Then the overall uncertainty of the viscosity can be determined by taking the square root of the sum of the squares of these two uncertainties shown as

$$\varepsilon_{\mu} = \pm\left[\varepsilon_{\mu}^{2} + \varepsilon_{\mu(T)}^{2}\right]^{\frac{1}{2}} \pm [(0.01)^{2} + (0.02266)^{2}]^{\frac{1}{2}} = \pm 0.0247 \; or \; \pm 2.47\%. \tag{65}$$

The next part of the equation to solve are the partial derivative terms in equation 60. This can be done by simply taking the derivative of equation 59 multiple times with respect to each of the variables. Then once the derivatives are substituted into equation 60, the term inside the bracket can be simplified. Examples of this simplification are shown for each variable. First the partial derivative of the Reynolds number with respect to the mass flow rate is calculated shown in equation 66 as

$$\frac{\partial Re}{\partial \dot{m}} = \frac{1}{\mu b}. \tag{66}$$

Then, this can be substituted into the bracketed term in equation 60 to show how the expression is simplified to become

$$\left(\frac{\dot{m}}{Re}\frac{\partial Re}{\partial \dot{m}}\varepsilon_{\dot{m}}\right)^{2} = \left(\frac{\dot{m}}{Re}\frac{1}{\mu b}\varepsilon_{\dot{m}}\right)^{2} = \left(\frac{Re}{Re}\varepsilon_{\dot{m}}\right)^{2} = \varepsilon_{\dot{m}}^{2}. \tag{67}$$

A similar simplification can be done for the dynamic viscosity to obtain similar results. The only difference is that since the variable is in the denominator of the fraction, the $\frac{Re}{Re}$ term is negative. This ultimately is cancelled out when the whole term is squared, which gives the derivative with respect to viscosity

$$\frac{\partial Re}{\partial \mu} = -\frac{\dot{m}}{\mu^{2} b}, \tag{68}$$

and substituted into the second bracketed term of equation 60 gives

$$\left(\frac{\mu}{Re}\frac{\partial Re}{\partial \mu}\varepsilon_{\mu}\right)^{2} = \left(\frac{\mu}{Re}\frac{-\dot{m}}{\mu^{2} w}\varepsilon_{\mu}\right)^{2} = \left(\frac{-Re}{Re}\varepsilon_{\mu}\right)^{2} = \varepsilon_{\mu}^{2}. \tag{69}$$

Finally, the same process is done for the channel width as well, yielding similar equations shown in equation 70,

$$\frac{\partial Re}{\partial b} = -\frac{\dot{m}}{\mu b^2}, \tag{70}$$

and the final bracketed term as

$$\left(\frac{b}{Re}\frac{\partial Re}{\partial b}\varepsilon_b\right)^2 = \left(\frac{\mu}{Re}\frac{-\dot{m}}{\mu b^2}\varepsilon_b\right)^2 = \left(\frac{-Re}{Re}\varepsilon_b\right)^2 = \varepsilon_b^2. \tag{71}$$

Similarly, to the viscosity case, there is a factor of -1 in this derivative as the variable for the width is in the denominator. By substituting these values into equation 60, the equation for the uncertainty interval for the Reynolds number is simplified greatly. The resulting equation becomes the square root of the sum of the squares of each uncertainty. This method ultimately yields a result of an uncertainty of ±2.49% in the Reynolds number, with the calculation shown as

$$\begin{aligned}\varepsilon_{Re} = \pm\left[(\varepsilon_{\dot{m}})^2 + \left(\varepsilon_{\mu}\right)^2 + (\varepsilon_b)^2\right]^{\frac{1}{2}} &= [0.002^2 + 0.0247^2 + 0.002083^2]^{\frac{1}{2}} \\ &= 0.02486\ or\ \pm 2.49\%.\end{aligned} \tag{72}$$

For the experiments conducted here, the maximum mass flow rate that was measured was of 8.56kg/s, which translates to an approximate Reynolds number of 80 000. Control of the pump rpm and mass flow rate are dictated using the LabVIEW software developed for the loop. Once the desired flow rate was set, the LabVIEW software automatically adjusts the pump rpm to ensure that the flow rate remains steady. From the LabVIEW software other parameters such as temperature, pressure drop, and density can be observed and measured in addition to the pump rpm. Figure 4 shows a zoomed in schematic of the test section with the streamwise (*x*), wall-normal (*y*), and spanwise (*z*) coordinates labelled relative to the direction of the flow.

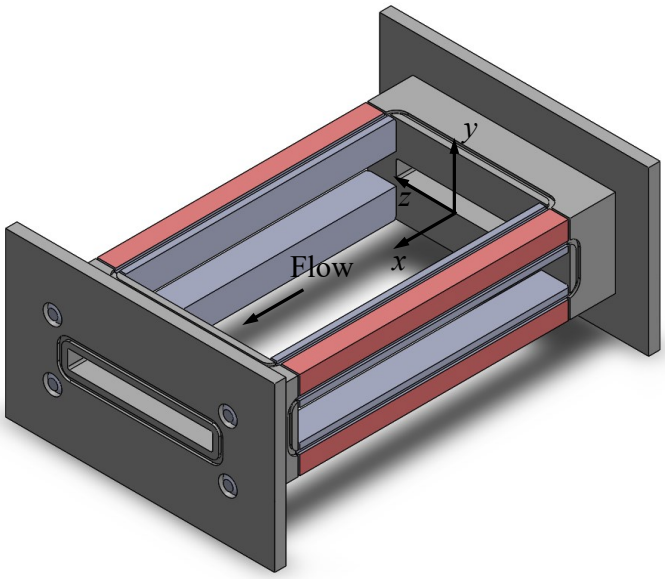

Figure 4: A zoomed in schematic of the test section with coordinate system labelled.

3.2 Particle Laden Flow

In these experiments, a total of three different types of particles were used. These consisted of approximately 420µm diameter polystyrene particles, 1.2mm polystyrene particles, and finally 420µm glass beads. Both polystyrene particles have a density close to that of water, while the glass particles have a much higher density. These densities are outlined in Table 2. All the particles were sieved using a Sieve Shaker from McMaster Carr to reduce variance among their sizes. Each set of particles were run at varying concentrations, with eight different Reynolds numbers for each concentration. These concentrations are defined as volume per volume and is calculated using the total fluid volume of 75L, which is consistent for all tests. To determine the mass of particles that needed to be added for each concentration, the volume required for each concentration was first determined. Then that value was multiplied by the particle density to give the mass of particles

required for each concentration. To further improve the consistency of the particles being measured, the particles were run through a sieve shaker to eliminate particles which deviated too far from the desired diameters.

When measuring the mass of the particles, the scale used is accurate to the nearest hundredth of a gram, and the uncertainty can be stated as ±0.01g. For the volume of water, the measurements of the tank are given by the manufacturer to the nearest inch, meaning the uncertainty interval for the radius to be ±0.5in or ±0.0127m. The height of water in the tank can similarly be taken to have this uncertainty as well. Using the method of propagation of uncertainties, the uncertainty of the concentration can be determined. The concentration most simply is calculated by dividing the mass of particles by the volume of water, which is determined by calculating the volume of a cylinder, shown as

$$Q = \pi r^2 h, \tag{73}$$

where Q is the volume of the cylinder, r is the radius of the cylinder, and h is the height of water in the cylinder. Similarly, to the process of determining the uncertainty for the Reynolds number, first the partial derivatives of the volume with respect to the radius and height variables are calculated. The partial derivative of the volume with respect to radius is

$$\frac{\partial Q}{\partial r} = 2\pi r h. \tag{74}$$

The partial derivative with respect to the height is shown as

$$\frac{\partial Q}{\partial h} = \pi r^2. \tag{75}$$

Calculating the uncertainty of the volume caused by each variable can now be determined. Equation 76 shows the equation for the radius,

$$\varepsilon_{Q(r)} = \frac{r}{Q}\frac{\partial Q}{\partial r}\varepsilon_r = \frac{r}{Q}2\pi rh\varepsilon_r = 2\varepsilon_r, \tag{76}$$

and the uncertainty for the height is shown in equation 77,

$$\varepsilon_{Q(h)} = \frac{h}{Q}\frac{\partial Q}{\partial r}\varepsilon_h = \frac{h}{Q}\pi r^2\varepsilon_h = \varepsilon_h. \tag{77}$$

Looking at the coefficients in these equations we can see that the uncertainty of the radius has a larger impact on the overall uncertainty than that of the height. The uncertainty of the volume can now be calculated with the uncertainty values stated above, shown as

$$\varepsilon_Q = \pm[(2\varepsilon_r)^2 + (\varepsilon_h)^2]^{\frac{1}{2}} = \pm[0.0127^2 + 0.0127^2]^{\frac{1}{2}} = \pm 0.01796 \; or \; \pm 1.80\%. \tag{78}$$

Using the uncertainties of mass and volume, the uncertainty of the particle concentration can be calculated as

$$\varepsilon_{conc} = \left[\varepsilon_m^2 + \varepsilon_Q^2\right]^{\frac{1}{2}} = [0.01^2 + 0.018^2]^{\frac{1}{2}} = \pm 0.0206 \; or \; \pm 2.06\%. \tag{79}$$

The concentrations run for each particle type are also outlined in Table 2. For most cases a total of 15000 images were collected for each Reynolds number aside from the initial test of the 420μm polystyrene particles, in which a total of 10000 images were captured. It was determined after this initial run to collect an extra 5000 images to ensure convergence and statistically significant data in the number of particles detected. Table 2 below summarizes all the parameters that were examined, where *C* is the particle concentration. To determine the density of the particles a fixed mass of the particles was first weighed. Then, those particles were added to a measured volume of water. The mass of the particles was divided by the change of volume of water that resulted from the addition of the particles, thus giving the particle density. This same procedure was conducted multiple times for each particle type to ensure accurate results.

Table 2: A table summarizing the particle parameters that were used for this experiment.

420µm Polystyrene Particles			1.2mm Polystyrene Particles			420µm Glass beads		
Re	*C* (%)	Density (kg/m^3)	*Re*	*C* (%)	Density (kg/m^3)	*Re*	*C* (%)	Density (kg/m^3)
10000	0.1	1070.92	10000	0.1	1042.24	10000	0.1	2511.25
20000	0.3		20000	0.3		20000	0.3	
30000	0.5		30000	0.5		30000	0.5	
40000			40000	0.7		40000	0.7	
50000			50000	0.9		50000	0.9	
60000			60000	1.1		60000		
70000			70000			70000		
80000			80000			80000		

The Stokes Number (*St*) is the non-dimensional value that describes the behavior of a particle within a fluid. The Stokes number is described in both Aggarwal et al. (1994) and Hamdi (2014) as a ratio of the particle relaxation time (τ_p) to the fluid characteristic time (τ_f). This ratio determines how quickly a particle's movement is affected by the movement of the surrounding fluid. Durham and Lundgren (1979) define the stokes number with the relaxation time variables broken down further, shown in as

$$St = \frac{C\rho_p U_b D_p^2}{18\mu_f D_h}, \tag{80}$$

where C is the Cunningham Correction Factor, ρ_p is the particle density, U_b is the fluid velocity, D_p is the particle diameter, μ_f is the fluid viscosity, and D_h is the hydraulic diameter. While the equation defined in Durham and Lundgren (1979) used the nozzle diameter in the denominator, here the hydraulic diameter is used as this experiment used a rectangular channel. The equation used to calculate the hydraulic diameter is shown in equation 81 as

$$D_h = \frac{2bH}{(b+H)}. \tag{81}$$

Using the values of 0.12m for b, the channel width and 0.015m for H, the channel height, the hydraulic diameter is calculated as 0.0267m. The Cunningham Correction Factor is defined in Tien and Ramarao (2007) as a variable meant to correct for the velocity slip that exists on the particle when the particle size is like that of the mean free path of the fluid. As the tracer particles used for PIV are very small, the Cunningham Correction Factor is close to one across all Reynolds numbers, and thus is omitted in the calculations for simplicity. Table 3 shows the stokes numbers for all the particle types considered at each Reynolds number, with the polystyrene particles abbreviated as PS in the table.

Table 3: Stokes numbers for particles considered in this experiment.

Re	**10000**	**20000**	**30000**	**40000**	**50000**	**60000**	**70000**	**80000**
420µm PS	0.218	0.436	0.653	0.871	1.09	1.31	1.52	1.74
420µm Glass	0.549	1.10	1.65	2.19	2.74	3.29	3.84	4.39
1.2mm PS	1.86	3.72	5.57	7.43	9.29	11.1	13.0	14.9

3.3 Particle Image Velocimetry

To characterize the unladen flow, Particle Image Velocimetry, or PIV, was applied. PIV works by observing small tracer particles that are added to the flow to determine the movement of the flow. Selection of these tracer particles is important as they must follow the fluid motion while not altering the flow or the movement of other particles, Westerweel (1994). The particles used in this experiment were 2µm diameter silver coated SG02S40 glass particles from Conduct-O-Fil. This particle size was chosen based on the Stokes Number (St), Table 4 shows a summary of the Stokes numbers for the tracer particles at each Reynolds number.

Table 4: Stokes numbers for tracer particles at each Reynolds Number.

Reynolds Number	10000	20000	30000	40000	50000	60000	70000	80000
Stokes Number $\times 10^{-3}$	0.035	0.058	0.080	0.10	0.12	0.14	0.16	0.18

To ensure that the particles follow the streamlines of the fluid, the particles must have a Stokes number that is less than one, meaning that the fluid characteristic time is larger than the particle relaxation time. This is because the particle relaxation time can be directly correlated to the difference in the path of the particle with the flow direction, Hamdi (2014). From Table 4 it is shown that for all Reynolds numbers, Stokes number is less than one for the seeding particles, thus the PIV process should achieve an accurate representation of the flow field.

A laser is used to illuminate a small portion of the channel in the form of a thin laser sheet, and a camera focused on this illuminated section to obtain images of the particles in the flow. The laser used here is a New Wave Research Solo PIV Nd:YAG laser which was mounted on rails at an elevation lower than that of the channel, pointing in the spanwise direction relative to the flow. To create the laser sheet in the channel, the laser was re-directed up into the channel via an optical setup consisting of a mirror angled at 45° and a series of lenses. First the laser hits the angled mirror, reflecting the beam 90° up into the bottom of the channel. Before the beam enters the channel, it passes through a series of three different lenses. The first lens it passes through is a concave spherical lens, with a focal length of -100mm. Next the laser passes though a spherical convex lens with f = 100mm. Finally, the laser passes through a concave cylindrical lens with f = -50mm. The combination of these lenses produces a laser sheet in the test section on which the camera is focused, illuminating any particles that pass through. This laser sheet is approximately 1mm thick in the spanwise direction and 2cm long in the streamwise direction. An image of the optical setup is shown in Figure 5.

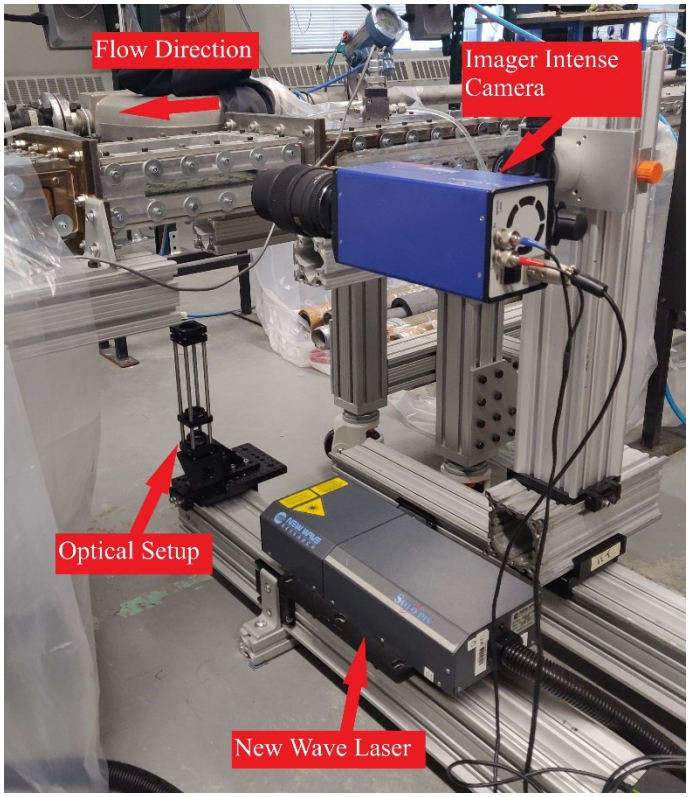

Figure 5: An image showing the optical setup used to capture images.

Images of the flow were taken with a LaVision Imager Intense camera which was also mounted on rails, this time level with the test section and pointed at the side glass panel of the channel, perpendicular to the direction of the flow corresponding to the spanwise direction. The pixels in the Imager Intense sensor have dimensions of 6.45µm × 6.45µm, with an overall sensor size of 1376 × 1040 pixels, resulting in a digital resolution of 155 pix/mm. This translates to a sensor height and width of 8.9mm × 6.7mm, respectively. The camera magnification is calculated by dividing the sensor height by the object height. In this case the object height is the 15mm height of the channel, which yields a magnification of 0.59. For the tests the camera f-number was set to 8.

Both the camera and laser are operated simultaneously using the DaVis software and a LaVision Programmable Timing Unit (PTU). To obtain an image pair, the laser flashes twice and the camera

simultaneously captures images while the laser sheet illuminates a section of the channel. The two pulses are set within a manually specified time interval. This time interval was adjusted for each Reynolds Number to ensure that the average particle displacement between the two frames was approximately 50 pixels. By dividing the displacement of the particles by the time difference between laser pulses the velocity of the fluid can be determined. The particle displacement is determined using a cross-correlation algorithm, Dabiri (2007), which starts with selecting an interrogation window at the same location on the two images of the image pair. Next, a fast-fourier transform cross-correlation algorithm is performed on the two interrogation windows which creates a correlation peak within the interrogation window. The location of the peak in the window indicates the average movement of particles in the direction from the center of the window to the peak location. This shift is then converted from a pixel domain to a physical domain to give a velocity vector within that interrogation window. The interrogation window is then shifted over, and the process is repeated to obtain velocity vectors across the whole image. To further increase the spatial resolution of the vectors, the interrogation windows often overlap with the previous window, Dabiri (2007). For this experiment, the vector calculation was refined by increasing the number of iterations of the cross-correlation in DaVis. By using a multi-pass process, the correlation peaks can be calculated across the image with a 64×64 pixel window, then further refined by repeating the cross-correlation across the image but this time with a 48×48 pixel window.

Understanding the uncertainty of the PIV process is crucial to recognize any variance that may be present in the measurements. Errors can be systemic, such as hardware timing and synchronization errors, or can be related to the image processing, such as changes in illumination or the interrogation algorithm, as stated in Sciacchitano (2019). Sciacchitano (2019) also summarizes

advantages and disadvantages with different methods of measuring uncertainty in PIV processes. These processes are intended to determine the local instantaneous uncertainty for each velocity vector. For an iterative multi-pass algorithm, such as the one used in this experiment, a direct method such as the correlation statistics method could be used. If the particles between interrogation windows match very closely, the cross-correlation peak will be sharp, in turn there will not be much uncertainty. When the particles between interrogation windows do not match, the cross-correlation peak is much broader. An asymmetric peak can also occur because of measurement error. This method looks at individual pixels in the interrogation windows and determines how much each pixel contributes to the asymmetry of the peak. The asymmetry is related to the uncertainty of the particle displacement. While the correlation statistics method can provide the uncertainty for each velocity component, it cannot determine the uncertainty of outliers, and thus those uncertainties cannot be considered. Sciacchitano (2019) state that an uncertainty of 5%-25% is present because of the finite number of particles available in the interrogation window. Another study by Westerweel (1997) stated that for a 32×32-pixel interrogation window the displacement uncertainty was approximately 0.1 pixels. While this assumption makes uncertainty calculations simple, it does not capture the whole picture, as PIV uncertainties will undoubtedly vary between experiments. Still, it could be useful to calculate this uncertainty to obtain a general idea. For a 64×64-pixel window we can assume that the uncertainty is 0.2 pixels. By dividing the channel height by the number of pixels in the sensor, then multiplying by the pixel uncertainty, and finally dividing by the time difference between frames, the uncertainty in terms of velocity can be obtained. An example is shown in equation 82 that uses the time difference for a Reynolds number of 50 000 to provide a median value for the uncertainty of the velocity as

$$\frac{\left(\frac{15mm}{1376pix} \times 0.2pix\right)}{(1000mm/m)(190 \times 10^{-6}s)} = 0.011\frac{m}{s}. \quad (82)$$

3.4 Particle Tracking Velocimetry

When analyzing the concentration profiles of the particle laden flows, Particle Tracking Velocimetry, or PTV was employed. The main difference in this method compared to PIV is that PTV focuses on tracking the movement of individual particles. By tracking the position of particles in the channel the distribution of the particle concentration across the channel height can be determined. Fortunately for this experiment, the same camera and laser setup that was used in PIV can also be used for PTV. With the flow seeded with particles, images are captured in a similar fashion to PIV. These images were then exported into a TIF (Tagged Image File) format and imported into a MATLAB code to detect the particles and their wall-normal position in the channel. This code was developed by Dr. Sina Ghaemi, which he iterated multiple times to optimize particle detection. The code first reads the TIF image files using the 'imread' function. Then, intensity coefficients were set manually and determined iteratively by viewing a sample of test images. These coefficients were chosen to maximize the number of particles detected, while also making sure that other bright spots caused by the channel wall or reflections were omitted. In certain cases, it was difficult to eliminate the background noise without also rejecting certain particles, so the code was designed to be more conservative as to not produce fake particles. Next the image was converted it to a binary image using the 'im2bw' function based on a threshold level of 0.5. This means that any pixel with an intensity lower than 0.5 are set to 0, or black, and any pixel with an intensity greater than 0.5 is set to 1, or white. After that, the function 'bwareaopen'

is used to remove clusters of components smaller than a specified number of pixels from the binary image. This allows us to remove any potential clusters smaller than the desired size of particles that are to be detected. Finally, particle detection is done using the function ‘imfindcircles’, which detects circles in the image based on a prescribed radius, and outputs the x and y coordinates of the circle center point in a two-column matrix. These coordinates are saved for both frame 1 and frame 2 of the image pair and are plotted against the y-coordinate of the channel to obtain the particle concentration profile across the height of the channel. Figure 6 shows a set of sample images to compare the raw image with which particles are detected.

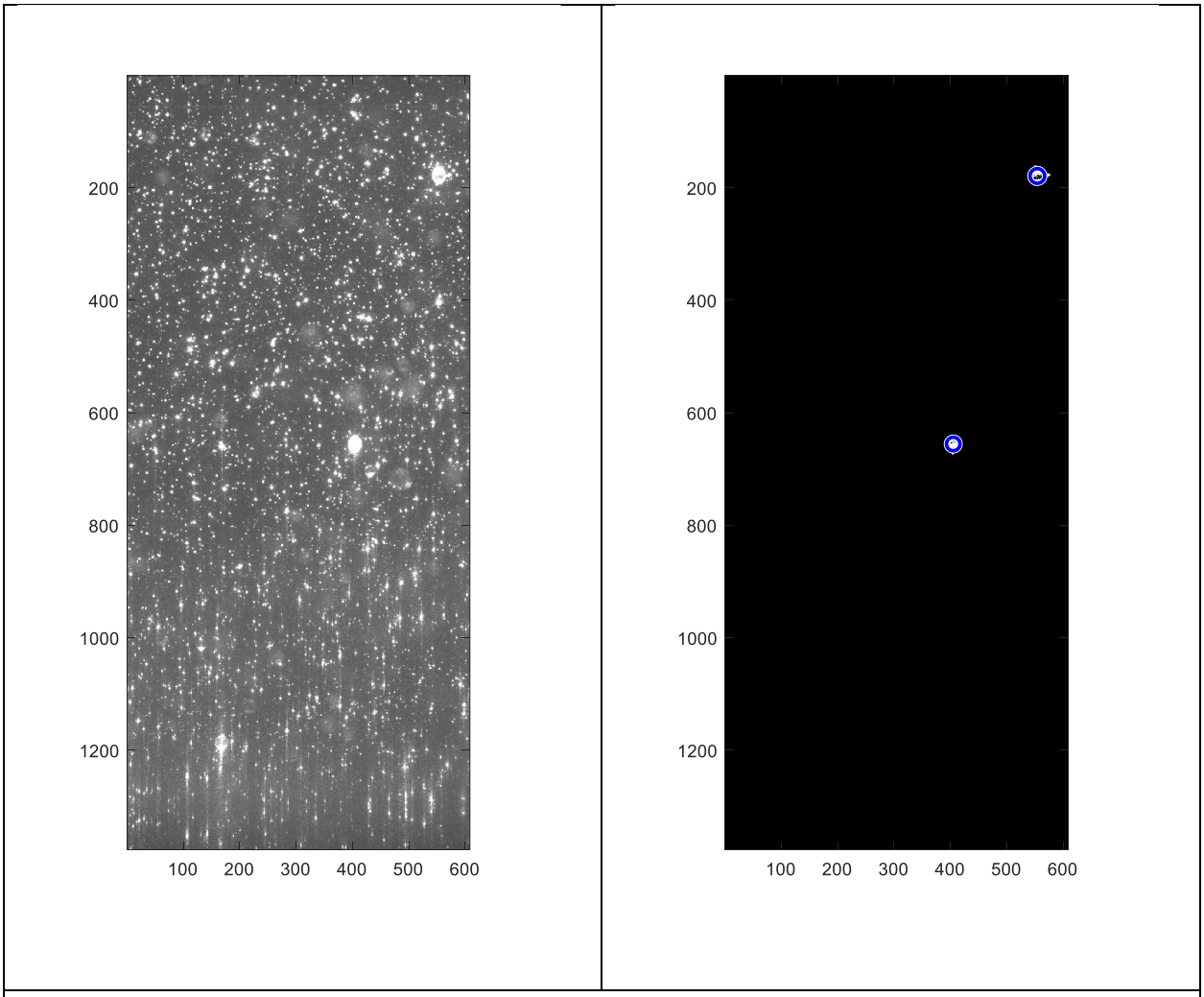

Figure 6: (a) Raw image file captured with camera. (b) Detected particles after being processed with MATLAB code.

Based on the change in position of the particle centers from frame 1 to frame 2, the streamwise and wall-normal velocities can be determined. These too, are plotted against the height of the channel to obtain figures of the streamwise and wall-normal velocity profiles. The image intensity coefficients were kept constant within a concentration, but they were adjusted between concentration sets to ensure that only particles were being detected, and any other erroneous bright spots were rejected.

As with all measurement methods, there is always an inherent error that exists in obtaining measurements using PTV. An example of such an error is the fact that the PTV method only records images of the particle location at distinct points in time, and there is of course a delay between each image. As a result, the location information of the particle between the two frames cannot be determined, which inherently causes some error, as it cannot be said what the path of the particle was between frames, Zeng et al (2022). Ambient light that is not properly blocked out of the measurement domain can cause a background intensity in the images. If there were too much light pollution in the images, the particles would not show up clearly in the images, and so they would not be able to be detected by the code. Additionally, the ambient light may make the code detect particles where there is simply a bright spot, creating false data. This was mitigated in this experiment by covering the test section with a cloth sheet to prevent outside light pollution, leaving very little room for the ambient light to reach the flow loop. Aside from excess light in the camera the algorithm must be tuned in such a way as to ensure that only the correct particles are detected. To refine the detection, the detection thresholds were adjusted through multiple iterations to try and reduce the error as much as possible. This was done by looking at a sample set of images, and adjusting the algorithm to make sure the highest number of particles were detected in each image. Errors in the particle detection would arise when particles across two different images could not all be detected by the same threshold, and so one of the images may have some particles that remain undetected. With a sample size as large as the one used in this experiment this source of error is present across multiple images. To try and further mitigate this in the future, as stated previously the ambient light that comes into the images could be reduced. The laser intensity could also be refined to obtain more consistency between image frames, which would help detection of the same particle between the frames.

To confirm the accuracy of the particle detection, a second set of images were captured with the laser position adjusted such that it was pointing down from the top of the channel, rather than from below. This was done by simply positioning a rail above the channel and flipping the optics 180° such that the laser pointed down from above the channel. Changing the laser orientation was intended to reveal any potential bias with the particles being detected. With the laser pointing up from the bottom, there is the possibility that the particles near the bottom of the channel are more greatly illuminated by the laser compared to the top of the channel, thus skewing the number of detected particles towards one side of the channel, depending on the intensity criteria used in the MATLAB code. If the particle concentration trend is the same regardless of the laser orientation, then it can be concluded that the laser position does not influence particle detection. Similarly, it is important to confirm that the flow within the test section is two-dimensional. This would mean that there is no velocity in the spanwise direction, and thus the shape of the streamwise velocity profile should remain the same across the entire width of the channel. To verify this, the laser sheet was shifted from the center of the channel in both the positive and negative spanwise directions by $z = \pm 30mm$ and $z = \pm 45mm$. The particle concentration profiles and description of the unladen flows should be the same at different points in the spanwise direction if the flow truly is two-dimensional. To maintain consistency the camera was also slightly moved forward and backward to keep relatively the same magnification between the centerline and offset cases. Figure 7 shows a plan view of the test section of the flow loop, with locations of the offset fields of view in the test section. FOV 1 and FOV 2 represent a shift of 30mm and 45mm respectively in the positive spanwise direction, and FOV 3 and FOV 4 are the 30mm and 45mm shifts respectively in the negative spanwise direction.

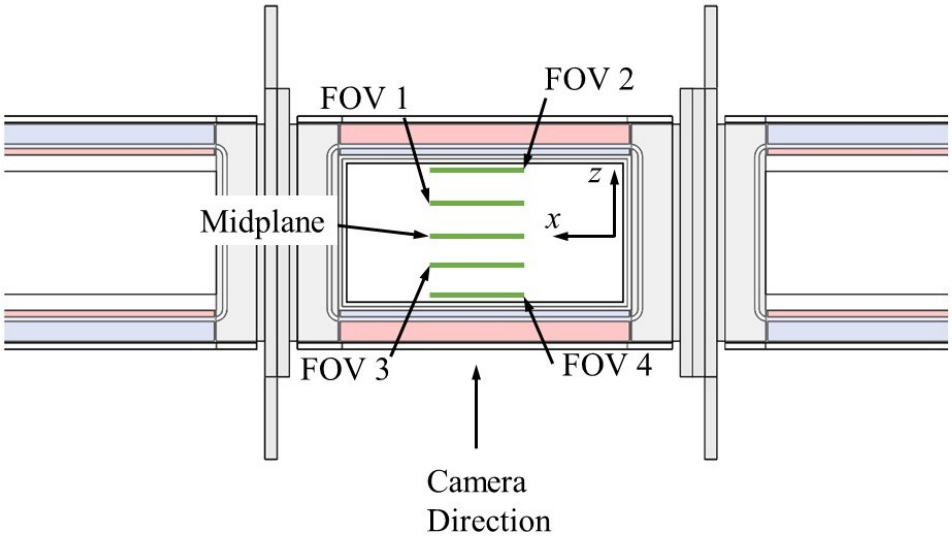

Figure 7: A schematic outlining the laser sheet positions for the different fields of view used to capture images.

A test was also conducted upstream of the test section, just after the transition section, to observe the behavior of the flow and particles just after the transition regime. This laser sheet was positioned at the midplane of the channel at a location 1.65m upstream of the test section shown in Figure 8. It should be noted that the particles used for the cases where the laser sheet was offset within the test section (FOV 1-4) were the 420µm polystyrene particles. However, the particles used in the upstream case were the 1.2mm polystyrene particles. This is because the walls of the rectangular channel sections consist of acrylic panels, unlike the test section which is comprised of glass walls. The cut lines on the acrylic panel made it difficult to decipher the 420µm polystyrene particles. Therefore, the larger 1.2mm particles were used because they were much easier to detect through the acrylic panel.

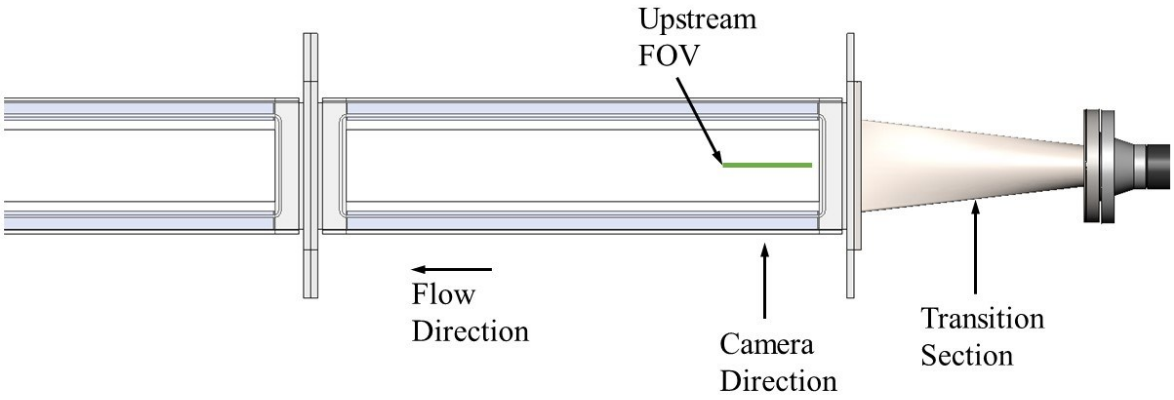

Figure 8: A schematic indicating the position of the upstream channel laser sheet.

Chapter 4. Unladen Flow

This section discusses the properties of the unladen flow. The properties that are investigated are the friction factor as well as the mean and normalized velocity profiles of the flow. These properties are used to characterize the unladen flow and compare the findings with literature to verify the suitability of the flow loop apparatus to obtain measurements of turbulent flows. Multiple tests of the unladen flow were conducted, including offset locations in the spanwise direction.

4.1 Friction Factor

Pressure measurements for the flow loop were obtained using a Validyne DP-15 pressure transducer which is fitted with a 2-psi diaphragm. The pressure drop is measured between a pressure port upstream of the test section to a second port downstream of the test section spanning a distance of 109H. These pressure ports are connected to the pressure transducer using rubber tubes. This difference in pressure is measured based on the deformation of the diaphragm within the transducer and is subsequently recorded using the LabVIEW software. The LabVIEW software also records other parameters such as the fluid density, temperature, and mass flow rate, which are measured by the Coriolis Flow meter. All these parameters are then exported and loaded into MATLAB for processing. The dynamic viscosity was estimated based on the average temperature of the water in the loop while the measurements were recorded. For consistency, the temperature was held around 25±0.2°C using a double pipe heat exchanger. Using these measured variables, the bulk velocity, Reynolds number, and friction factors were calculated using equations 83, 84, and 85 respectively. Equation 83 for the bulk velocity is given as

$$U_b = \frac{\dot{m}}{\rho H b}, \tag{83}$$

where U_b is the bulk velocity, $\dot{m}$ is the mass flow rate, ρ is the fluid density, H is the channel height, and b is the channel width. As previously stated, the mass flow rate was measured using the Coriolis Flow Meter located upstream of the test section, and the height and width have dimensions of 0.015m and 0.12m respectively. The equation for the Reynolds number is given as

$$Re = \frac{\rho U_b H}{\mu}, \tag{84}$$

where Re is the Reynolds number, and μ is the dynamic viscosity. Lastly, the friction factor is calculated using equation 85, which is shown in Pope (2000) as

$$f = \frac{\bar{P} H}{\rho U_b^2 \, dx}, \tag{85}$$

where $\bar{P}$ is the mean pressure drop across the pressure transducer, and dx is the distance between the pressure ports. U_b is again the bulk velocity calculated from equation 83. The friction factor was then plotted against Reynolds number, and compared against two different relationships, the first being Dean's correlation (Dean 1978),

$$f = 0.073 Re_H^{-0.25} \tag{86}$$

and the second being the equation for the friction law in a channel flow,

$$\frac{1}{\sqrt{f}} = \frac{1}{\sqrt{2}\kappa}\left[\ln\left(Re\sqrt{f}\right) - \ln 2\sqrt{2} - 1\right] + \frac{B}{\sqrt{2}}. \tag{87}$$

Equation 87 is obtained by approximating that the velocity profile across the entire channel height follows the log law. A detailed derivation of this equation is shown in Chapter 2. Dean's correlation is one of the most robust observations of turbulent channel flow, which compared observations of multiple authors to determine the correlation between the Reynolds number and other bulk flow parameters, such as skin friction drag. It is for this reason that it is often referenced by other papers,

and why it is used for comparison with the measurements conducted in this experiment. In addition, Dean (1978) shows through the comparison of the various results that there is no consistent evidence to show that the friction factor values were influenced by the aspect ratio for any of the channel sizes examined. The minimum aspect ratio examined in that study was 7, whereas the aspect ratio for the channel used in this experiment is 8, which falls within the range examined by Dean (1978), meaning the friction factor calculated here is not influenced by channel aspect ratio. However, more recent studies, such as the summary put together by Vinuesa et al (2016) show that as more research is conducted, it becomes increasingly prevalent that a higher aspect ratio is required to obtain a two-dimensional flow. Zanoun et al. (2003) investigated flows in a channel with an aspect ratio of 12. Finally, Vinuesa et al. (2016) suggest that an aspect ratio as large as 24 is required if a two-dimensional flow is to be approximated.

As shown above in equation 87, the equation for friction law for channel flow was derived by following the same process as the derivation for Prandtl's friction law for pipes. In equation 87, the values of κ and B are implicit, and thus values are assumed based on agreed upon ranges found in the literature. Here $\kappa = 0.41$ and $B = 5.2$, as is shown in Pope (2000), yielding the final coefficients shown in equation 88,

$$\frac{1}{\sqrt{f}} = 1.72 \ln\left(Re\sqrt{f}\right) + 0.159. \tag{88}$$

When these values are used in the friction law equation for channel flow, the line almost exactly correlates with Dean's correlation, as is shown in Figure 9. Alongside these lines, the calculated friction factor values for multiple unladen tests are also plotted in Figure 9, denoted as Test 1 through Test 6. The purpose of performing multiple tests was to evaluate the ability to consistently model turbulent flow in the flow loop. For all data sets the values were recorded at Reynolds numbers ranging from 10 000 to 80 000, in intervals of 10 000 except for Test 5, which was only

measured up to a Reynolds number of 60 000. From Figure 9 it can be shown that the measurements collected here do follow the trend of both equations, with the friction factor values decreasing as the Reynolds number increases. It should be noted that there is some variance among the friction factor values between the tests, however this variance becomes smaller as the Reynolds number increases, and the data points come closer together. One reason for this variance, and the most likely reason, could be choice of the pressure transducer and diaphragm that were used to collect the measurements. It is possible that the 2-psi diaphragm used for the pressure measurements was not sensitive enough to accurately detect the change in pressure. At a Reynolds number of 10 000, the average recorded pressure drop was approximately 0.04 psi. With the 2-psi diaphragm that is used in this experiment, that only equates to approximately 2% of the total range of pressure that the diaphragm can detect, which might be the cause of the variance at this Reynolds number. On the contrary, as the Reynolds number increases, the average pressure drop also increases, and thus the relative error in the measurements is reduced. This results in the data points coming closer together and almost overlap, indicating consistency between the various measurements taken. For future reference, to obtain a more consistent reading between tests, a more sensitive diaphragm can be chosen to be able to detect the smaller pressure changes more robustly. To continue using the same diaphragm used in this experiment, measuring higher Reynolds numbers such that the pressure drops recorded reach closer to the limit of the diaphragm's sensitivity could also help obtain more consistent readings between Reynolds numbers.

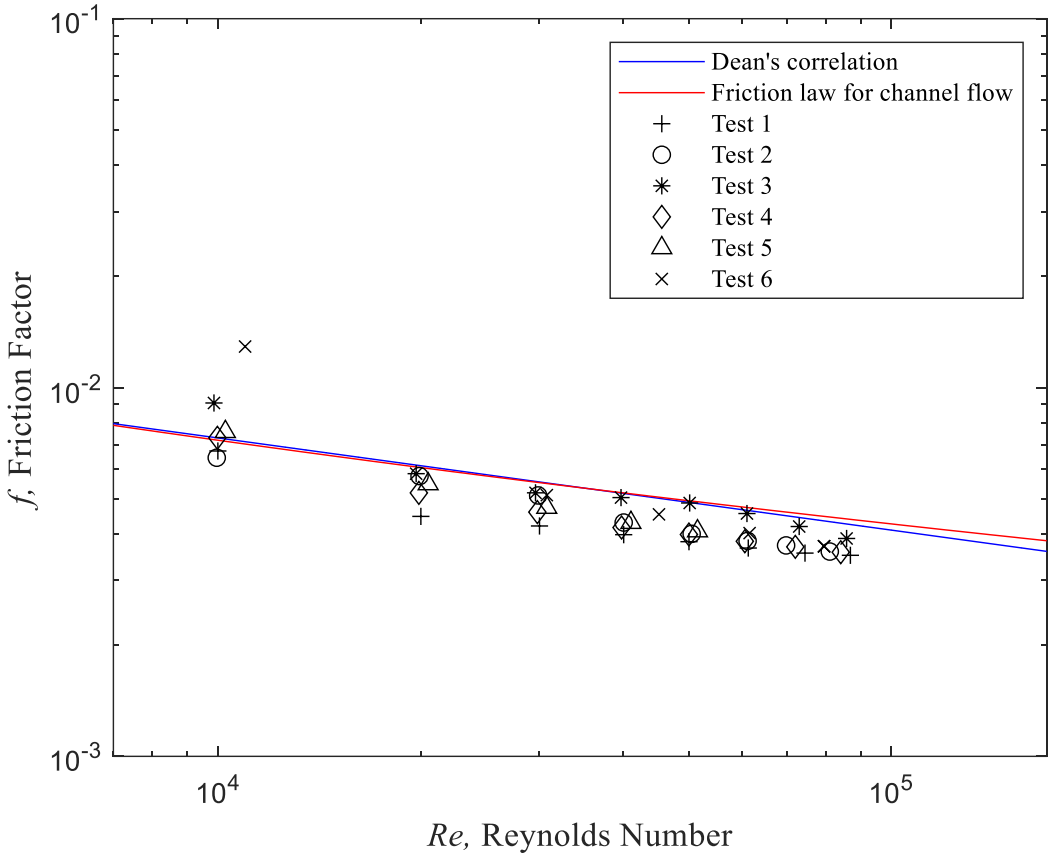

Figure 9: A plot showing the calculated friction factor as a function of Reynolds number for various unladen flow tests, with lines for Dean's correlation and the friction factor for channel flow shown for comparison.

4.2 Mean Velocity Profile

The mean velocity profiles of the unladen flow were plotted to compare the accuracy of the measurements with existing literature, as well as to validate the measurement capabilities of the flow loop itself. To capture the velocity profiles of the unladen flow, the flow was seeded with the 2-micron silver coated seeding particles. A total of six different cases were considered when collecting images of the unladen flow, and three Reynolds numbers were measured for each case

to cover the full range at which the particle laden flow was captured as well. These six cases varied in that the laser sheet used to observe the particles were in different locations. The locations considered are the midplane of the test section, and a 30mm (0.25*b*) and a 45mm (0.375*b*) offset in both the positive and negative *z*-directions, and finally an additional midplane measurement, this time located further upstream of the test section. A schematic of these offset locations was shown previously in Figure 7 in Chapter 3. The reason for choosing the offset positions is to see if the velocity profile is consistent across the width of the channel. At the 0.375*b* offset locations the laser sheet is only 15mm away from the wall, so this position can tell us how the velocity profile behaves in the near wall region. Finally, the upstream midplane position was chosen such that the laser sheet is located directly downstream of the transition section in the flow loop. This transition section is where the flow loop cross section changes from a pipe to the rectangular channel. Examining the flow field in this region of the channel shows how quickly the flow becomes fully developed after the transition section. Figure 10 shows the mean streamwise velocity profiles plotted against the wall normal position of the channel for the midplane, offset, and upstream positions. Of note, the velocity profiles in Figure 10 are not normalized. Here $y = 0$ on the horizontal axis indicates the bottom of the channel and $y = 15$ indicates the top of the channel. To check the symmetry of the velocity profiles, the velocity profiles for each case were flipped about the channel center and plotted along with the normal velocity profile, indicated with the dashed lines. As is shown from the figures, for all the cases aside from the upstream case the flipped velocity profiles show no significant deviation to the normal velocity profile, indicating that the profiles are symmetric about the channel midplane. There is some noticeable deviation in the upstream case which may be attributed to the fact that the section is directly following the transition region, and thus the flow is not yet fully developed. Also represented in Figure 10 is that

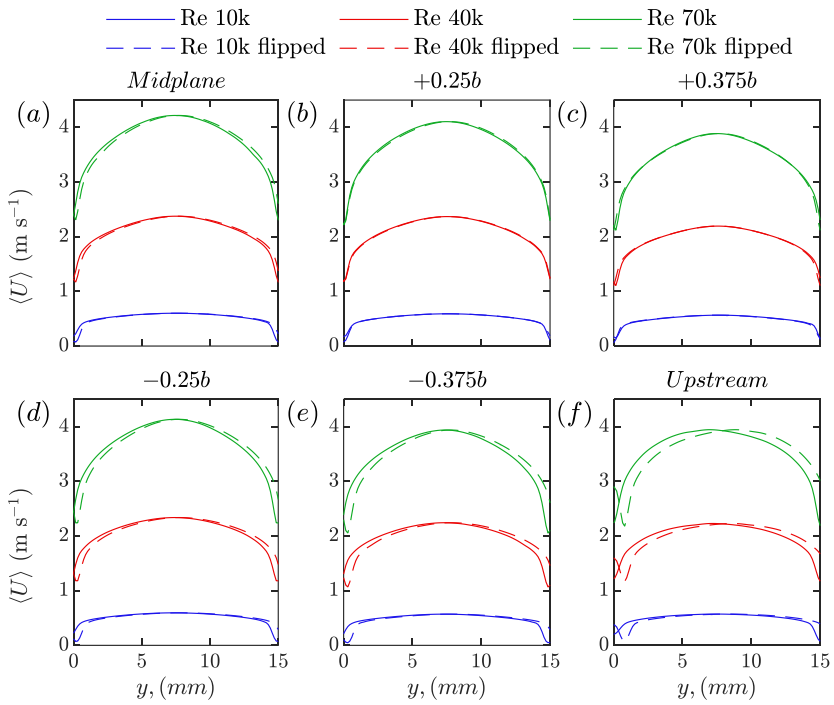

Figure 10: The streamwise velocity profiles for the (a) Midplane, (b) +0.25*b*, (c) +0.375*b*, (d) -0.25*b*, (e) -0.375*b* laser positions along the *z*-axis, (f) and the channel upstream position.

the magnitude of the velocity profiles is consistent across all the subplots, with some deviation in the ±0.375*b* cases. For these cases, shown in Figure 10 (c) and (e), the magnitude of each velocity profile is smaller compared to all the other cases. This is because at these cases, the laser sheet is close to the side walls of the channel, and as a result, the flow velocity is reduced due to the no slip boundary condition at the wall. This difference in magnitude is hard to see for a Reynolds number of 10 000 but becomes much more prominent at Reynolds numbers of 40 000 and 70 000, as the difference of velocity is much more exaggerated.

To compare the differences of the velocity profiles more effectively among each of the offset locations, the mean velocity profiles need to be normalized. To do this, the mean velocity profile <*U*> was divided by the bulk velocity U_b for each respective Reynolds number, and the wall-normal position was divided by the total height of the channel, *H*. This bulk velocity is the mean

bulk velocity calculated from the mass flow rate, which is obtained from the Coriolis Flow Meter. The Reynolds numbers and their respective bulk velocities are shown in Table 5.

Table 5: Bulk flow velocities at their respective Reynolds numbers

Reynolds Number	Bulk Velocity, U_b (m/s)
10 000	0.528
40 000	2.112
70 000	3.696

Figure 11, Figure 12, and Figure 13 show the normalized streamwise velocity profiles for the midplane and offset locations in the test section as a function of wall-normal position for Reynolds numbers of 10 000, 40 000, and 70 000, respectively. From these figures it is much easier to visualize the slight difference in magnitude between each of the offset locations. Across all the figures, the case with the highest magnitude is the midplane case, which makes sense as the center of the channel would have the highest magnitude of velocity following a parabolic profile, due to being least affected by the channel boundary conditions. Then the next highest magnitude profiles are the ±0.25*b* cases, which still closely match in magnitude to the midplane cases. This is expected as this location is still relatively close to the channel center, so the magnitude of velocity would not change greatly. Finally, the ±0.375*b* cases have the smallest magnitude compared to the other locations. The reason for this is that these locations are close to the side walls of the channel, and while the fully developed flow has the highest magnitude of velocity at the channel center, the velocity gradually gets smaller closer to the wall because of friction at the side walls. The profiles are also all symmetric about the streamwise axis at $y/H = 0.5$, indicating that the flow is one-dimensional.

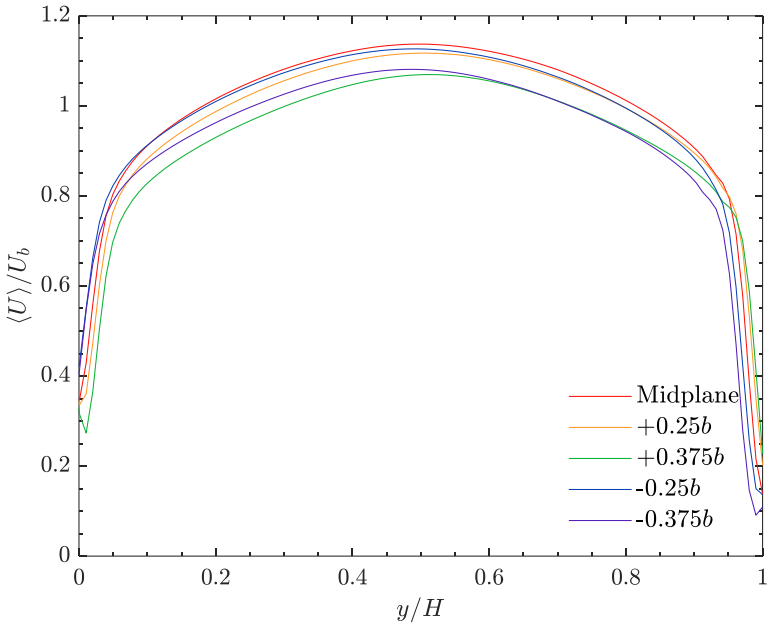

Figure 11: The normalized streamwise velocity profiles of the unladen flow at a *Re* = 10 000.

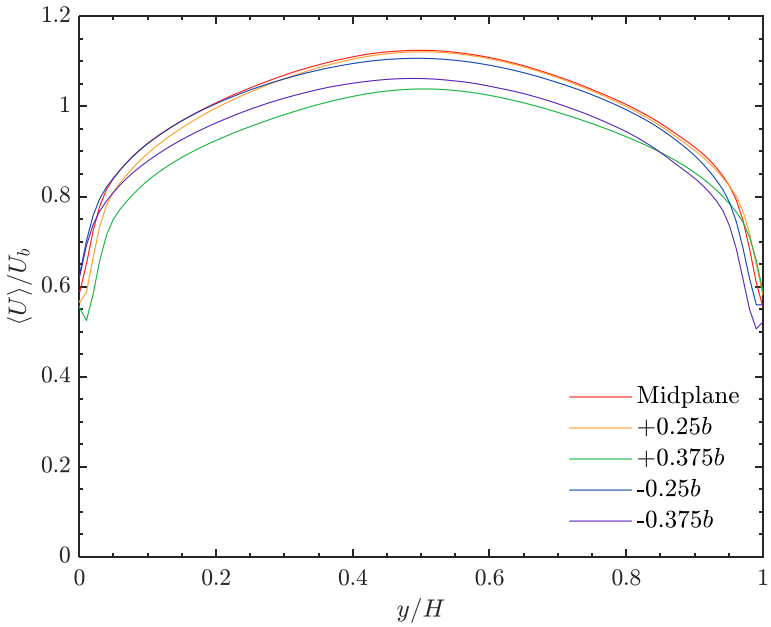

Figure 12: The normalized streamwise velocity profiles of the unladen flow at a *Re* = 40 000.

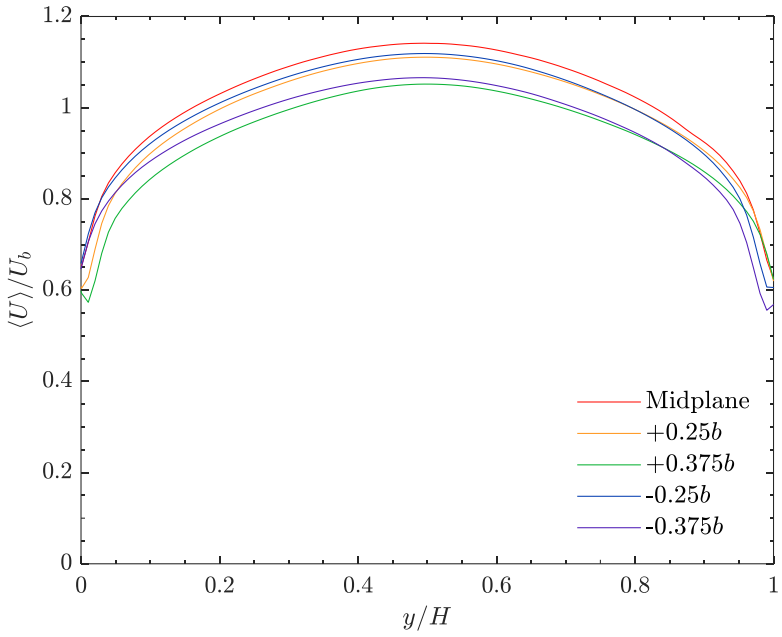

Figure 13: The normalized streamwise velocity profiles of the unladen flow at a *Re* = 70 000.

The magnitude of the offset profiles is consistent with the offset profile in the opposite direction. For example, the magnitude of the +0.25*b* offset is the same as the magnitude of the -0.25*b* offset. The same is true for the ±0.375*b* case. This indicates that the flow characteristics are the same across the channel width, which validates the accuracy of the measurements taken from this flow loop.

Figure 14 through Figure 16 compare the normalized velocity profile at the midplane of the test section to the midplane of the upstream channel section for Reynolds numbers of 10 000, 40 000, and 70 000. These figures can help show how close the upstream profile is to the fully developed profile in the test section. One clear difference between the two cases across all Reynolds numbers is that the upstream velocity profile has a smaller magnitude of velocity compared to that inside the test section. This again is a result of the flow not being fully developed at this location as the measurements were taken close to the transition section. Capturing images at this location also required positioning the camera such that it looks through the acrylic panels of the rectangular

channel section. While less likely to be a source of error, the acrylic panel did create some difficulty in detecting the seeding particles because the images are not as clear as they are through the glass panels in the test section. Images of the seeding particles showed up as streaks instead of distinct particles. Despite this the PIV processing was still able to distinguish particles with good accuracy, allowing the resolution of a full velocity profile. The smoothness of the velocity profile shows that the transition piece connecting the pipe cross section of the loop to the rectangular cross section of the loop does a good job of gradually adjusting the cross-section shape, thus not causing any large disturbances in the flow field. As a result, the flow transitions back to a fully developed flow very quickly following the transition region and reaches the magnitude of the bulk velocity quickly after that point.

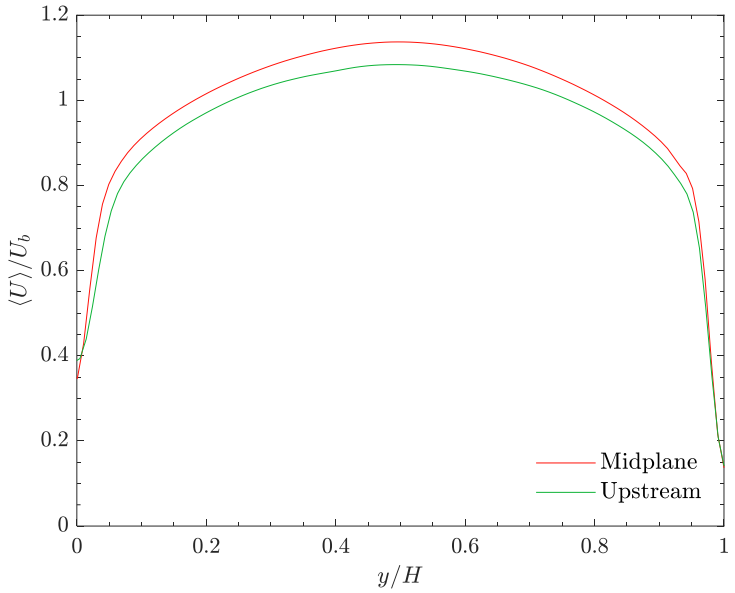

Figure 14: The normalized streamwise velocity profiles for the test section midplane and channel upstream midplane locations at Re = 10 000.

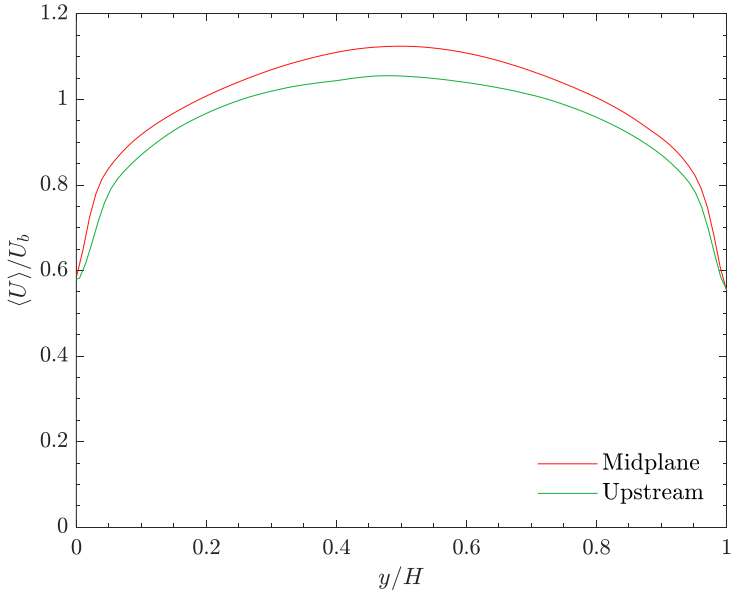

Figure 15: The normalized streamwise velocity profiles for the test section midplane and channel upstream midplane locations at Re = 40 000.

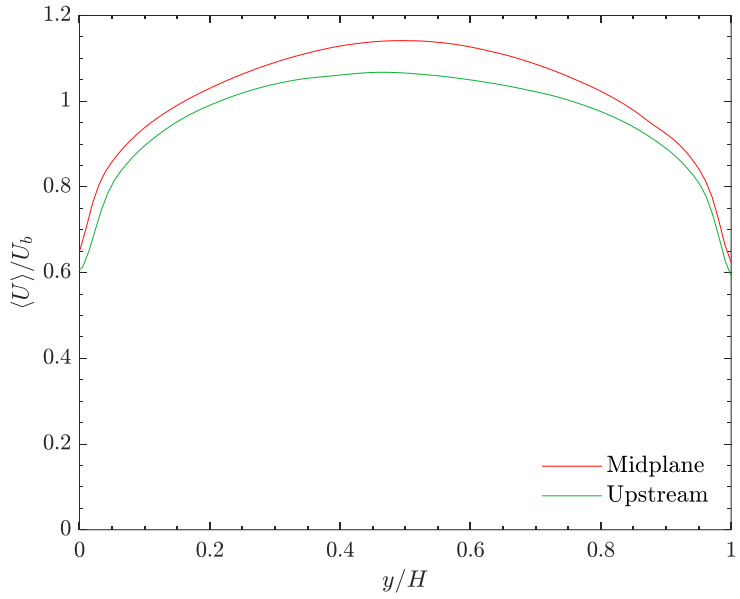

Figure 16: The normalized streamwise velocity profiles for the test section midplane and channel upstream midplane locations at Re = 70 000.

Finally, the wall-normal velocity profiles were also plotted as a function of wall normal position for each respective case in Figure 17. These figures show the if there is any motion of the fluid in the wall-normal direction, and if the motion is symmetric about the half channel height. Like the streamwise profiles in Figure 10, these profiles are also not normalized. The wall-normal profiles can help affirm if the flow can be considered one-dimensional. As is evident from Figure 17, there is some variation that can be observed in the plots for each Reynolds number, but that is because the scale of the magnitude of velocity is magnified significantly to easily visualize the plots. Realistically, this change is magnitude is not large enough to cause any significant change in the motion of the fluid for any of the cases that were observed. Because the wall-normal velocity is close to zero for all the cases, we can confirm that the flow can be considered a one-dimensional flow, and there is also no significant variation in the flow field along the spanwise direction. It is interesting to note that for the cases within the test section, as the Reynolds number is increased,

the profiles are biased towards a negative value. This is contrary to the upstream case where the higher Reynolds numbers yields a slightly positive velocity profile. One possible reason for this difference is that as previously stated, the flow in this region is not yet fully developed. As a result, the increased number of turbulent fluctuations may have caused the seeding particles to be biased in a more upward position. This positive wall-normal velocity is also only seen at the top of the channel across all Reynolds numbers, which may be a result of increased inter-particle collisions. However again these variations are small in magnitude compared to the overall bulk velocity of the fluid, and as such are considered negligible. As the wall-normal profiles are all very close to zero, the validity of the flow loop for measurements is affirmed as the loop can accurately depict one-dimensional flow.

The streamwise velocity profiles shown in this section demonstrate good consistency with existing literature. From the streamwise profiles it is evident that the velocity profile is consistent as the Reynolds number is increased. The wall-normal velocity profiles indicate that there is no significant movement in either the positive or negative y-direction. Additionally, the profiles at the offset locations indicate that the flow field is consistent across the span of the channel as well. These observations help confirm the validity of the flow loop for the use of observing turbulent flows.

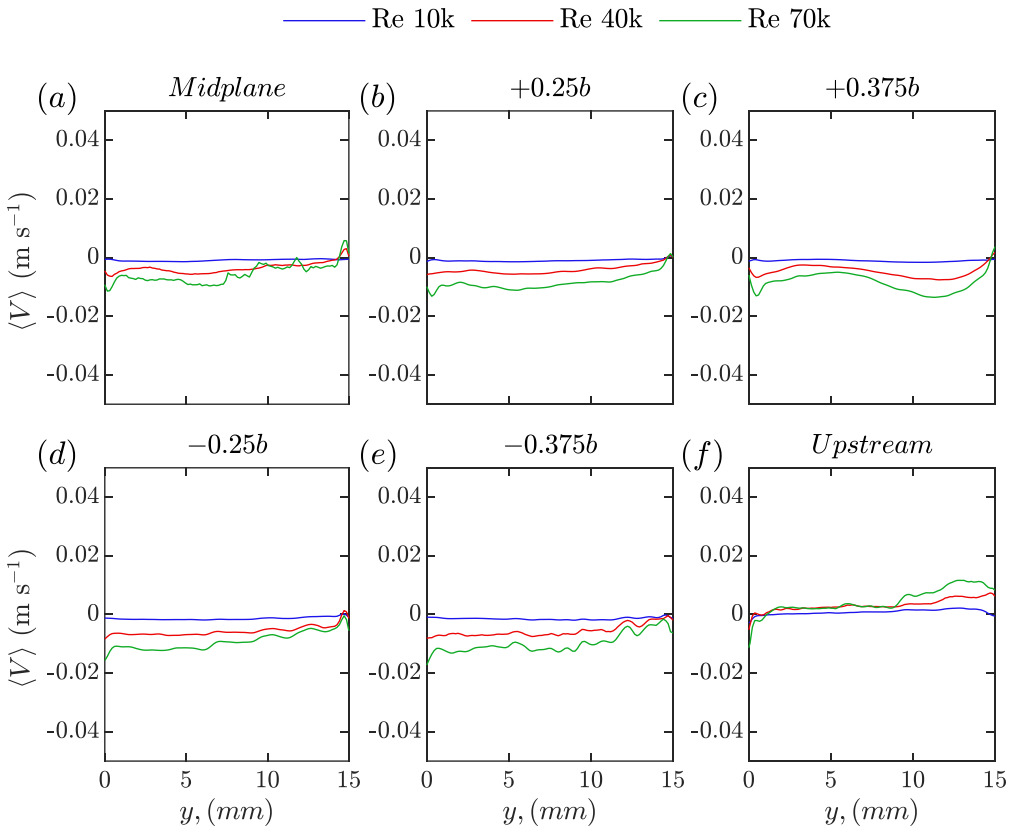

Figure 17: The wall-normal velocity profiles for the (a) midplane, (b) +0.25*b*, (c) +0.375*b*, (d) -0.25*b*, (e) -0.375*b* laser sheet locations along the *z*-axis, (f) and the upstream position.

Based on these observations, the flow loop shows good suitability for the measurement of turbulent flows. When comparing the mean streamwise profiles across the span of the channel, the profiles are consistent in both the positive and negative *z*-directions, indicating that the flow field is consistent in both directions. The midplane profile had the largest magnitude, followed by the ±0.25*b* location, and then the ±0.375*b* location had the smallest magnitude. This makes sense as the overall flow velocity becomes slower closer to the wall due to the no-slip condition at the wall. At the upstream location the profile has overall smaller magnitude compared to the test section as the flow is not fully developed in this region.

Chapter 5. Particle Laden Flows

This section discusses the observations made of the particle laden flows. In Section 5.1 the particle concentration plots for the various particle types are discussed. The figures show the particle distributions along the wall-normal direction at various Reynolds numbers and channel spanwise directions. Three different particle types were considered, including two different sizes of polystyrene particles, and one size of glass particles from Manus Abrasive Systems. The observations from this investigation are intended to explore the particle distribution within the channel, if they tend to migrate towards the channel walls, and how the distribution varies with particle type and Reynolds number. In the following Section 5.2 the velocity profiles of the particle laden flows in both the streamwise and wall-normal directions are examined to see if they are consistent with the unladen case, verify that the flow within the test section is truly one-dimensional, and to see how the velocity profiles may potentially impact the particle distribution within the channel.

5.1. Particle Distributions

Particle detection was facilitated using the code previously described in Chapter 3. For all particle types, the particle distribution figures have the number of particles detected along the vertical axis, and the wall normal position normalized by the total channel height along the horizontal axis. The horizontal axis ranges from 0 to 1, with 0 being the bottom of the channel, and 1 being the top of the channel, which is consistent for all the images of the different cases explored here. Each plot is divided into subplots for each concentration that was examined, and within those concentrations a total of nine Reynolds numbers are plotted. The Reynolds numbers ranged from 10 000 to 80

000. For each case, images were captured starting at *Re* = 10 000, and then increased by increments of 10 000 each time. After the *Re* = 80 000 case was completed, the flow velocity was dropped back down to *Re* = 10 000 and recorded for a second time, which is indicated by the 'Re 10k Down' label on all the figures. This second measurement is intended to check the consistency of the flow field as the flow is decelerated, and that the measurements being obtained are consistent by comparing it with the first round of *Re* = 10 000 data. For the first 3 particle cases (Sections 5.1.1. to 5.1.3.) the laser sheet was shone from the bottom of the channel, and for the last two cases (Sections 5.1.4. and 5.1.5.) the laser sheet was pointed from the top of the channel. Changing the direction from where the laser points is intended to detect if there is any bias in particle detection, namely if there are significantly more particles detected on the side of the channel where the laser is pointing from.

5.1.1. 420µm Polystyrene Particles

The first set of particles that were examined are the smaller polystyrene particles. These particles had a mean diameter of 420µm, and a calculated density of approximately 1070.92 kg/m^3. This density is close to the density of water at 25°C (997.05 kg/m^3) as the particles are meant to be approximately neutrally buoyant, thus indicating that they should disperse evenly in the flow field. The particles were illuminated with a collimated laser from the bottom of the channel, and a total of 10 000 images were captured with the camera oriented in the spanwise direction, capturing images in the *x*-*y* plane. The three concentrations that were examined in this case are 0.1%, 0.3%, and 0.5%, shown in Figure 18. It is evident from the 0.1% and 0.3% concentrations that most of the particles tend accumulate more near the channel center and form a parabolic profile. However, for the 0.5% case, the concentration peak is located closer to the top of the channel, indicating

some variance caused by the increase in concentration. This bias towards the upper section of the channel is not expected and may be caused by a phenomenon such as particle-wall lubrication or turbophoretic drift. When looking across the varying Reynolds numbers, the number of detected particles is relatively constant in the 0.1% case. At concentrations of 0.3% and 0.5%, it is evident that as the Reynolds number increases, the number of particles that were detected decreases. This again would mean that the detection algorithm may have needed to be further adjusted to detect more particles. The outlier is that even when the flow velocity is reduced again in the 'Re 10k Down' case, the number of detected particles is lower than the initial 'Re 10k' case. As the particle detection parameters are the same as the initial 'Re 10k' case, the reduction in particle detection may indicate some greater inconsistency in the flow field itself in this case or be the result of the intensity of the laser not being consistent.

Figure 19 shows the same plots but this time the detected particles are normalized by the total number of detected particles at each Reynolds number. These normalized plots show what percentage of the total detected particles were detected at each point along the height of the channel. For all three concentrations the shape of the normalized concentration profile is parabolic across all Reynolds numbers. Looking at the 0.1% and 0.3% cases shows that most of the particles detected in these cases were close to the center of the channel. While the raw number of particles detected varies between these cases, shown in Figure 18, the normalized plots show that the fraction of particles detected along the channel height is consistent across Reynolds numbers. The 0.5% case is an exception where the shape of the profile is still parabolic, but in this case the normalized peak is closer to the top of the channel, and not the center. This trend is not consistent with observations of neutrally buoyant particles in literature, such as in Zade et al. (2018) and Fornari et al (2016). Their observations both show a flat profile shape across the channel height,

and no profile peak near the walls at similar concentrations. It is only at much larger concentrations that they observe a near-wall profile peak. Thus, as previously stated this profile shift may be caused by particle-wall lubrication. This phenomenon as discussed in Ahmadi (2020), is when a particle is close to the wall there is an increase in pressure between the particle and the wall. Conversely the pressure reduces as a particle moves away from the wall. This increase and decrease in pressure create a repulsive and attractive force on the particle respectively. This combination of forces along with inter-particle collisions results in particles being unable to move away from the near wall region, resulting in the increased local concentration.

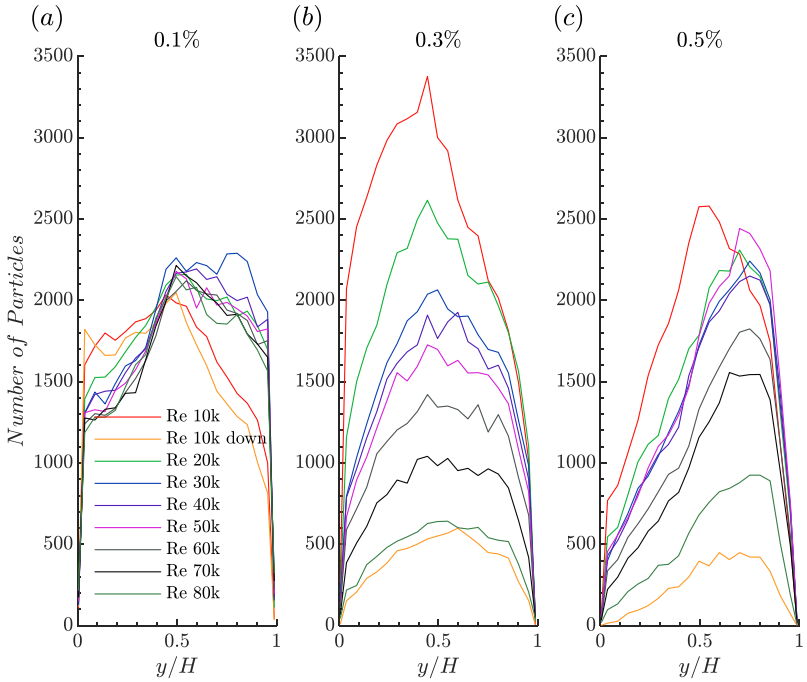

Figure 18: The 420µm particle distribution plots.

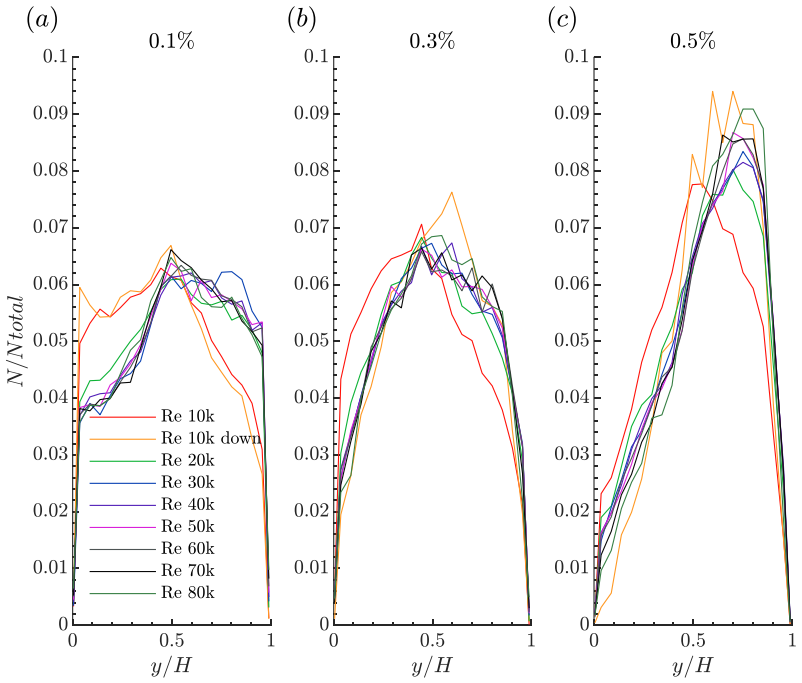

Figure 19: The normalized 420µm particle distribution plots.

5.1.2. 1.2mm Polystyrene Particles

The next set of particles that were examined were the 1.2mm polystyrene particles. For this set a total of six concentrations were examined ranging from 0.1% to 1.1% in increments of 0.2%, with the same camera and laser orientation as the first 420µm case. Starting from this case and for the rest of the results discussed in this paper, a total of 15 000 images were captured to ensure statistical convergence and increase the total number of detected particles. Because the particles in this case are larger compared to the other cases, the number of particles required to reach the volume for each desired concentration is less compared to the other smaller particle cases. Therefore, compared to the smaller particle cases, the overall number of detected particles is lower in this 1.2mm particle case. To try and account for this, higher concentrations were examined to try to obtain consistent data with a higher number of particles. For this case specifically, after a certain

point as the concentrations were increased, the water became murky, which obscured the images of the particles. As a result of the darker images, the particle detection code needed to be adjusted to increase the detection threshold, which increased the brightness across the entire image and sometimes made some particles undetectable. Therefore, there is a reduction in the overall number of detected particles starting from the concentration of 0.7%. The issue was rectified in subsequent measurements.

Figure 20 shows the particle distributions along the wall-normal direction in a manner like the previous test. These particles are also comprised of the same material as the previous case, and their density was calculated to be approximately neutrally buoyant at 1042.24 kg/m^3. From Figure 20 at low Reynolds numbers across all concentrations the particles typically tend to collect near the bottom of the channel. With Reynolds numbers of 30 000 and above, the concentration profile peak is closer to the channel center, apart from the 0.5% and 0.7% cases. In these cases, the concentration peak is closer to the top of the channel for the higher Reynolds numbers. Like the smaller polystyrene particles, this behaviour appears to be reminiscent of particle-wall lubrication, with the particles accumulating near the upper wall. The 0.9% and 1.1% concentration cases appear to be outliers comparted to the other cases due to them having the smallest number of detected particles despite having the highest bulk concentrations. As previously stated as more particles were added the water in this case because increasingly murky, possibly because some other contaminant got mixed in, which made the particle detection more difficult. Future measurements could rectify this by ensuring that no other contaminants are mixed in with the particles on in the channel.

Figure 21 shows the normalized plot of the 1.2mm particle distributions, with the number of particles being normalized by the total number of detected particles at each Reynolds number. The

figure shows that for all the concentrations, at a Reynolds number of 10 000 and 20 000, most particles were detected near the bottom of the channel, likely a result increased gravitational settling due to the higher Stokes numbers of these particles. This trend became less prominent as the Reynolds number was increased despite this also increasing the Stokes numbers for these cases as well. At larger Reynolds numbers, the increase of turbulent diffusion as mentioned in Ahmadi et al (2020) results in the particles moving further away from the walls. This is observed for all cases aside from the 0.1% and 0.3% cases, which show a relatively uniform distribution, consistent with the fact that the particles are approximately neutrally buoyant and other observations in existing literature. For the remaining cases, a similar trend to the 420μm particles starts to appear in that the profile peak is starts to move closer to the upper wall. Likewise, this trend is consistent with the behaviour of particle-wall lubrication, like the smaller polystyrene particles. This deviation could possibly be the result of increased inter-particle interactions that occur due to the larger particle size and concentration, which restricts the movement of the particles away from the near wall region, and thus creating a particle layer with a higher concentration.

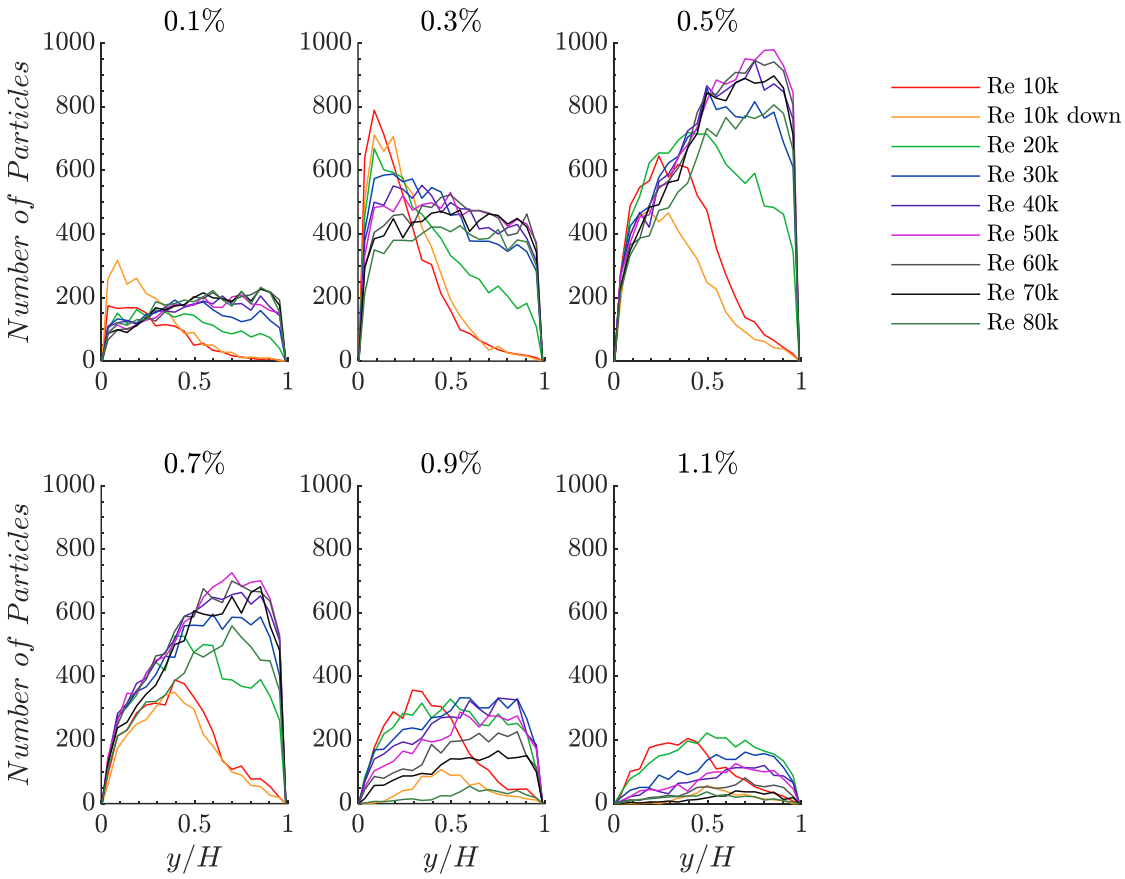

Figure 20: The 1.2mm particle distribution plots.

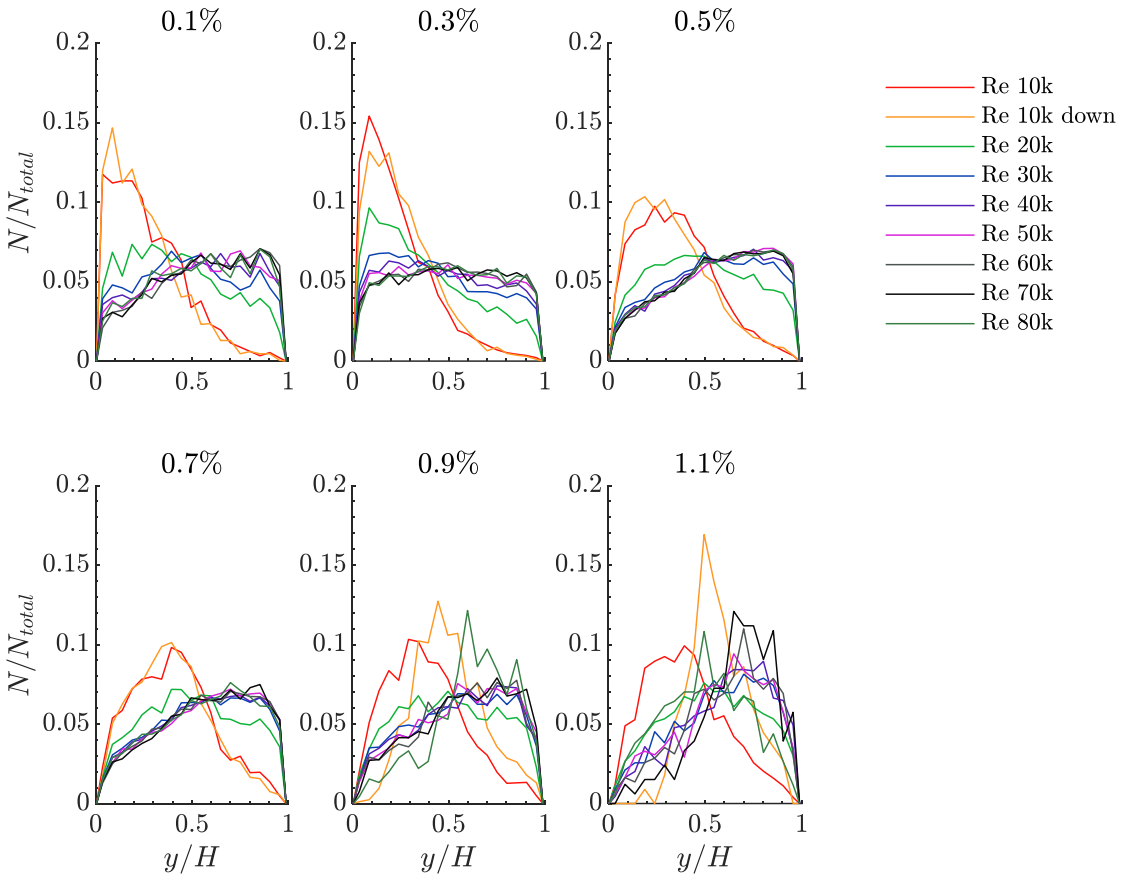

Figure 21: The normalized 1.2mm particle distribution plots.

5.1.3. 420µm Glass Particles

Next, the set of particles that were examined were the glass particles that had a mean diameter of 420µm, like the first case. These particles are of particular interest because they are made of a different material and have a density much higher than that of water, which was calculated to be approximately 2511.25 kg/m^3. This increased density means that a smaller mass of particles was required to reach the desired concentrations, and so the overall number of detected particles is smaller than the 420µm polystyrene particles, despite having the same approximate size. Also, because of the higher density these particles have a larger Stokes number, so it is expected that

more particles should accumulate near the bottom wall, especially at lower Reynolds numbers. In this case, only five concentrations were examined, ranging from 0.1% to 0.9% in increments of 0.2%. Figure 22 shows the particle distributions with respect to the wall-normal location. It is evident that in almost all the cases, there is a higher concentration of particles towards the bottom wall of the channel. As the Reynolds number increases, the peak of the particle distribution moves closer to the channel center. However, we also see that as the flow rate is reduced, the particles settle along the bottom of the channel very quickly, which is shown when comparing the upstroke and downstroke cases for Re = 10 000 for each concentration. In these lower Re cases, the number of detected particles is significantly less than the other Reynolds numbers. With many particles accumulating near the bottom wall, it is inevitable that some particles will be blocked by other particles in front of the camera path, which would contribute to the overall reduction in the number of detected particles. Looking at Figure 22, it seems that the 0.9% concentration case is an outlier compared to the other concentrations as the overall number of particles detected across all Reynolds numbers is much smaller compared to the other cases. The detection threshold was adjusted such that spots in the images were not accidentally detected, but in this case, it may have been too strict, resulting in the smaller number of detected particles. Improving either the detection algorithm or the image quality would help refine the consistency of the number of detected particles throughout all these experiments. For the rest of the concentrations most of the particles accumulate near the bottom of the channel at lower Reynolds numbers, and only start moving to the channel center as the flow velocity is increased. The 0.3% case is unique in that the profile shapes for every Reynolds number is almost the exact same in shape, just with varying magnitudes. Here all the profiles are all wall-peaking towards the bottom wall with a very sharp decline as the profile reaches the mid-channel height. As the Reynolds number is increased, the magnitude of the

peak gets smaller, and the overall profile shape starts becoming flatter. Although the shape of the profile is quite different, the behaviour of particles moving away from the bottom wall is consistent with the other concentrations.

Figure 23 is the same plot normalized by the total number of detected particles. Across all concentrations there is a clear trend of gravitational settling as particles accumulate near the bottom wall at lower Reynolds numbers. There is one outlier in the plot of the downstroke case when *Re* = 10 000 for a concentration of 0.1%. The line for this case is very jagged, because not many particles were detected in this instance, so this plot is not a good approximation of overall the concentration profile at this Reynolds number. Improving the particle detection in this case could be facilitated by either increasing the laser intensity or also adjusting the detection code parameters to allow for a higher number of particles to be detected. Overall, the behaviour of these particles close to the bottom wall is a bit trivial, as the higher density means that the particles require more force for them to move with the flow and against the force of gravity. It is only at the higher Reynolds numbers that the increase of turbulent diffusion causes the particles to disperse more, which moves the profile peak closer to the channel center. This general trend was also observed in other experiments looking at glass particles, such as in Ahmadi et al (2020). In Ahmadi et al (2020) a large near-wall peak is observed for all concentrations. As the Reynolds numbers increases, there is still a near-wall peak, but the overall concentration profile becomes flatter and more uniform across the channel height.

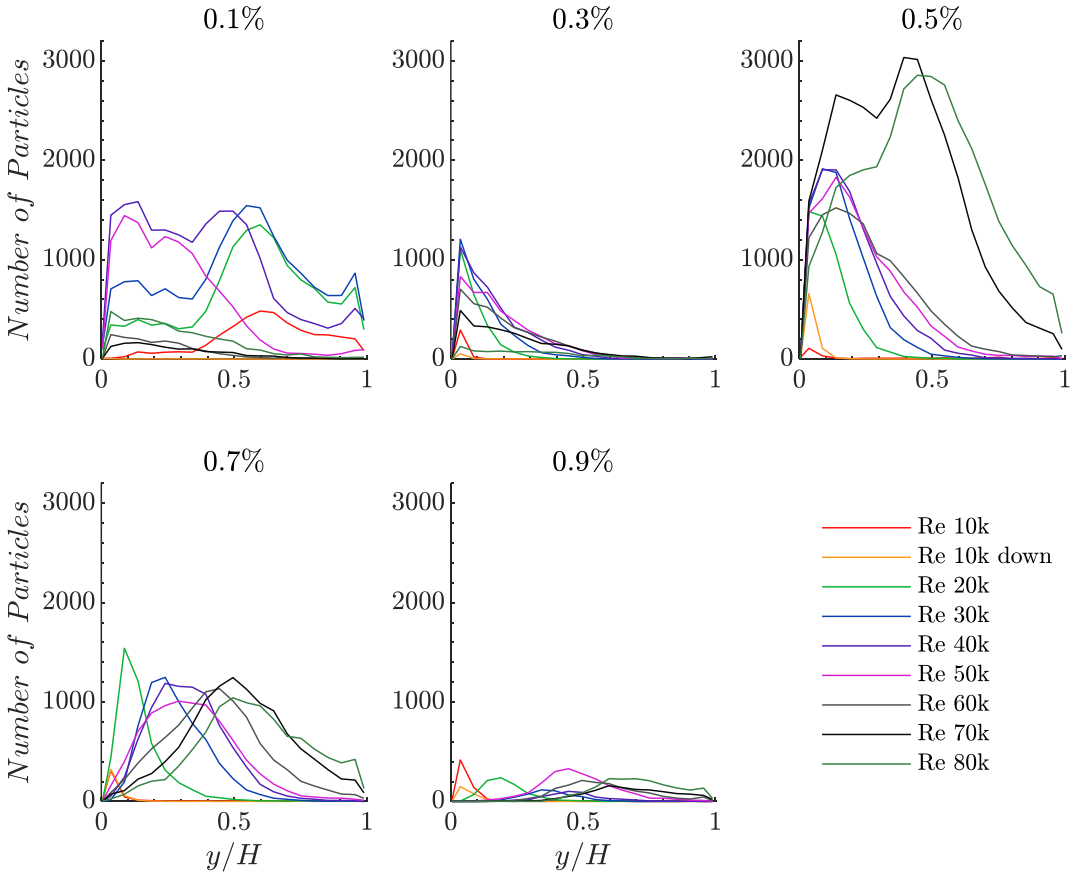

Figure 22: The 420µm glass particle distribution plots.

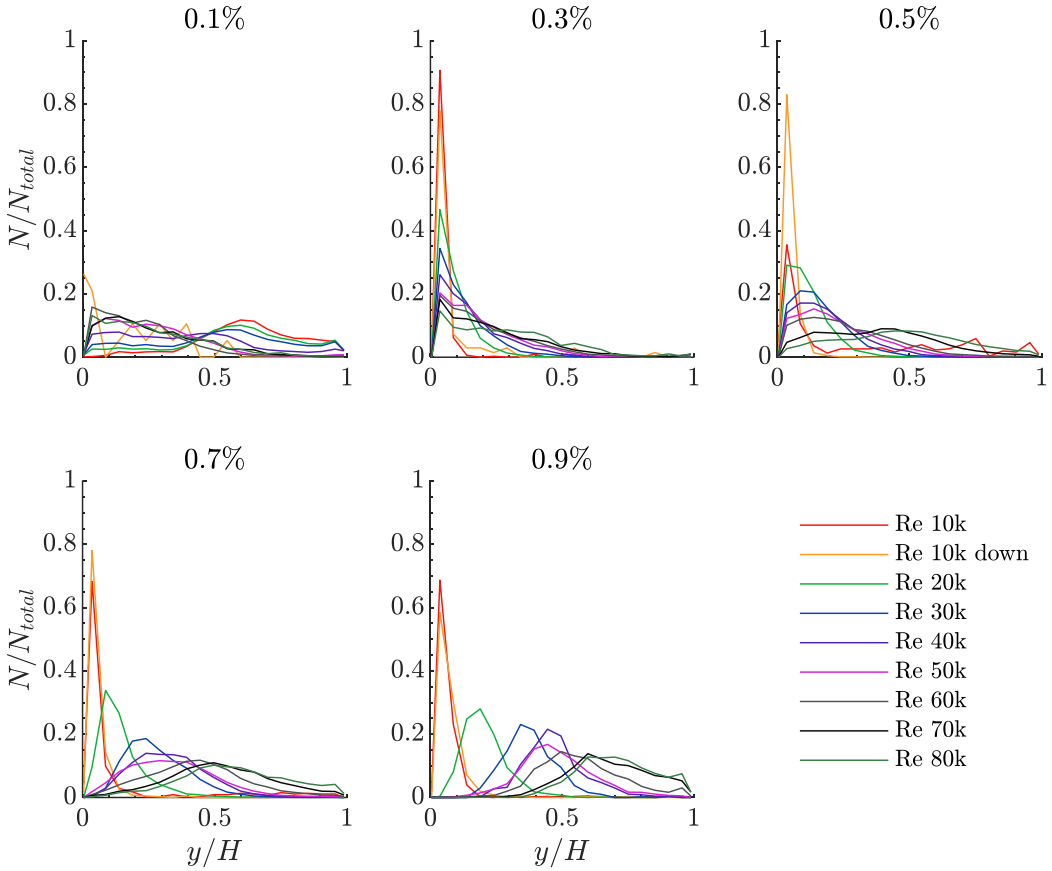

Figure 23: The normalized 420µm glass particle distribution plots.

5.1.4. Effect of Measurement Location

After the initial tests of the three particle types, another test was conducted using the same 420µm polystyrene particles to check the consistency of the data. In this case, the laser was positioned such that it was pointing down in the negative *y*-direction, from above the test section. These measurements were intended to check for any potential bias in the particle detection based on the direction of the laser, and to see if any of the particles are being illuminated unevenly. For the sake of brevity, only a 0.1% particle concentration was considered here. In addition to adjusting the laser direction, the location of the laser sheet in the test section was also adjusted along the *z*-axis

of the test section. A total of five different laser sheet positions were considered including the channel midplane, and then 30mm (0.25b) and 45mm (0.375b) offsets in both the positive and negative directions along the z-axis. Looking at the channel from a top-down perspective, the positive z-direction means that the laser sheet is moved farther away from the camera, while the negative z-direction means that the laser sheet is moved closer to the camera. A detailed schematic of the laser sheet positions is available in Chapter 3.4. Checking these offset positions was intended to verify that the flow did not vary along the spanwise direction, and to validate if the particle distributions are consistent across the width of the channel.

Particle distributions for the midplane and offset locations are shown in Figure 24. Starting with the midplane plot in Figure 24 (a) and comparing to the first case of 420µm particles we can determine if the orientation of the laser influences particle detection. Here the particle distribution is uniform across the channel height, with a local maximum close to the location where $^{y}/_{H} = 0.5$. Comparing back to the initial 0.1% distribution plot in Figure 18 (a), there are some differences between the midplane plots shown here. While the distribution in Figure 18 (a) shows a peak at the mid-height of the channel, in the case shown in Figure 24 (a) the number of detected particles is much more constant across the height of the channel for all Reynolds numbers. Looking at the normalized plot in Figure 25 (a), the percentage of the total particles detected is roughly constant across the channel height for lower Reynolds numbers. On the contrary, at higher Reynolds numbers, specifically Re = 50 000 and above, the profiles start lower near the bottom of the channel and increases towards the top of the channel. This trend is also seen in the normalized plots in Figure 19 (a), with a lower percentage of detected particles near the bottom wall, and an overall higher percentage of detected particles near the upper wall for Reynolds numbers of 20 000 and above. However, in the cases where Re = 10 000 the opposite trend is observed. With the

laser pointing from above in Figure 24 (a), the profiles for the Re = 10 000 cases at the midplane are much more constant across the height of the channel. Comparison of these plots shows that the changing of the orientation of the laser did not significantly affect the total number of particles detected, but it did affect the overall shape of the profile. With the laser positioned above the channel, the profiles observed are much flatter, showing greater consistency with profiles in discussed previously in existing literature such as Zade et al (2018). These profiles indicate that obtaining observations with the laser pointing down from above the channel should result in more accurate results and may explain some of the inconsistencies in profile shape observed for the previous cases at higher bulk concentrations.

To test the offset positions, first the laser sheet was moved in the positive z-direction by 0.25b from the midplane, and then another 15mm so that it was 0.375b from the midplane. The positive z-direction correlates to moving the laser sheet farther away from where the camera is positioned. With a total channel width of 120mm, in the 0.375b offset cases the laser sheet was only 15mm away from the channel wall, which is useful to see if there is any change in the particle distribution profile near the wall. At the +0.25b case shown in Figure 24 (b), we see a slight increase in the bias of the particle distribution to accumulate at the top of the channel, along with a high variation in the number of detected particles between Reynolds numbers. At the +0.375b case, shown in Figure 24 (c), the number of detected particles is much more consistent across most Reynolds numbers, with a wall-peaking profile appearing for Reynolds numbers of 10 000 to 40 000, like results observed in the 0.1% case of the 1.2mm particles. In the next two subplots, Figure 24 (d) and (e), the laser sheet was again moved by the same distances relative to the channel centerline, but this time in the negative z-direction, meaning that this time the laser sheets are closer to the camera. Figure 24 (d) and (e) are both very consistent in terms of profile shape, as well as the

number of particles detected for both the -0.25*b* and -0.375*b* cases. They both show a profile that has a higher particle concentration near the bottom wall, with the concentration decreasing towards the upper half of the channel.

Looking at the normalized profiles in Figure 25 we see a similar trend across all the profiles. Starting with the +0.25*b* case, we again see a trend where the lower Reynolds numbers have a relatively flat profile, and as *Re* increases, the peak moves slightly towards the upper half of the channel. At the +0.375*b* location the profile is relatively flat across all Reynolds numbers, indicating good correlation with existing literature. Lastly, the -0.25*b* and -0.375*b* normalized plots are both very similar to the concentration plots, showing very close consistency between all the Reynolds numbers, and a higher percentage of detected particles near the bottom of the channel.

Looking at all the offset profiles, there appears to be some variance in the particle distributions based on the location of the laser sheet relative to the camera. When compared to the observations with the laser pointing from the bottom of the channel, these observations overall have a much flatter profile across the span of the channel, indicating that taking measurements with the laser positioned above the channel is better to obtain results which are consistent with existing literature. As the laser sheet is moved further away, the distribution between Reynolds numbers becomes tighter. This trend is present when looking at the profiles in both the positive and negative *z*-direction. The shape of both near wall profiles (±0.375*b*) are slightly different, which may be attributed to their distance within the channel. For the -0.375*b* case, the laser sheet was much closer to the camera, and there is a smaller chance of other particles blocking the view to the laser sheet. On the contrary, at the +0.375*b* case, the camera is viewing the laser sheet across almost the full width of the channel. While the camera is focused on the laser sheet, there may be instances where out of focus particles passing between the camera and laser sheet cause some discrepancy in the

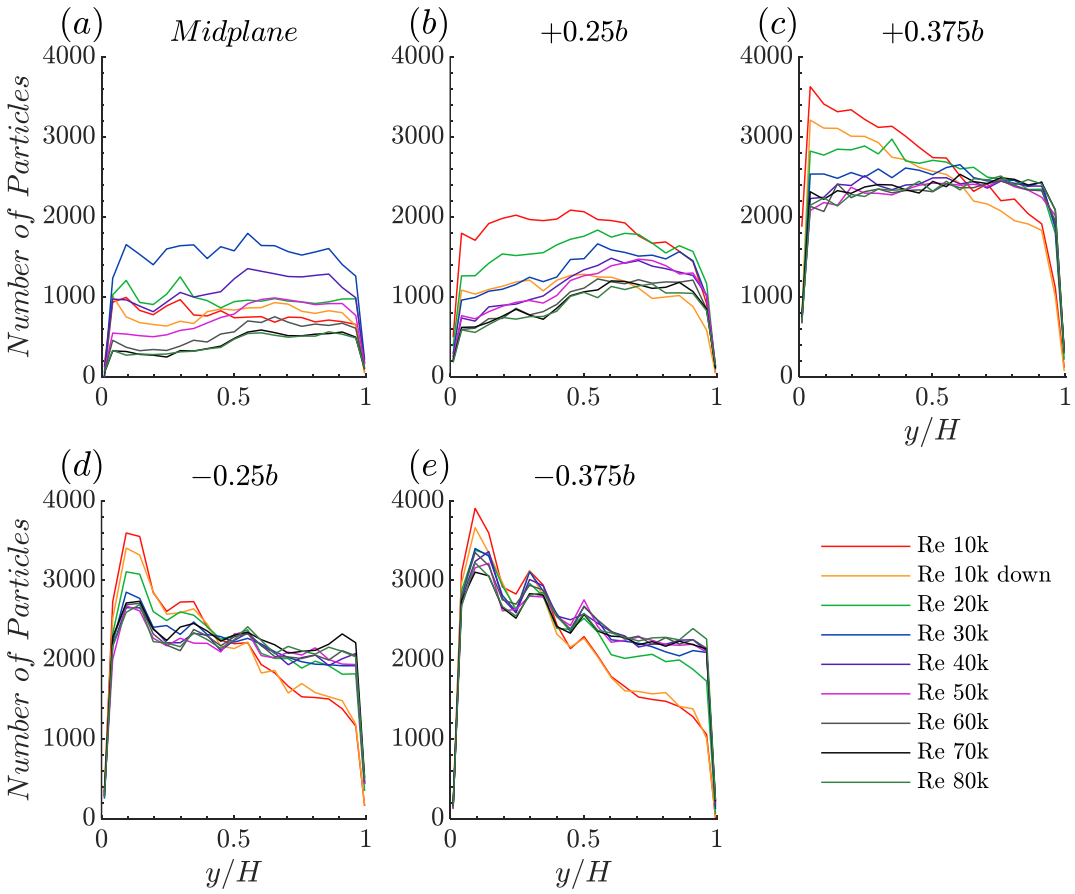

Figure 24: The 420µm particle distribution plots with the laser pointing from the top.

particle detection, which may be the reason the lower Reynolds number cases at this position have a different profile shape compared to the higher Reynolds number cases. When comparing the offset locations to the midplane location in Figure 25, it is evident that the offset locations have much less variation between the Reynolds numbers compared to the midplane. A possible reason for this could be that the bulk velocity close to the side walls is slower due to the no-slip condition at the wall, thus resulting in less variation between the velocity of the particles, and so the distributions are observed to be much closer together.

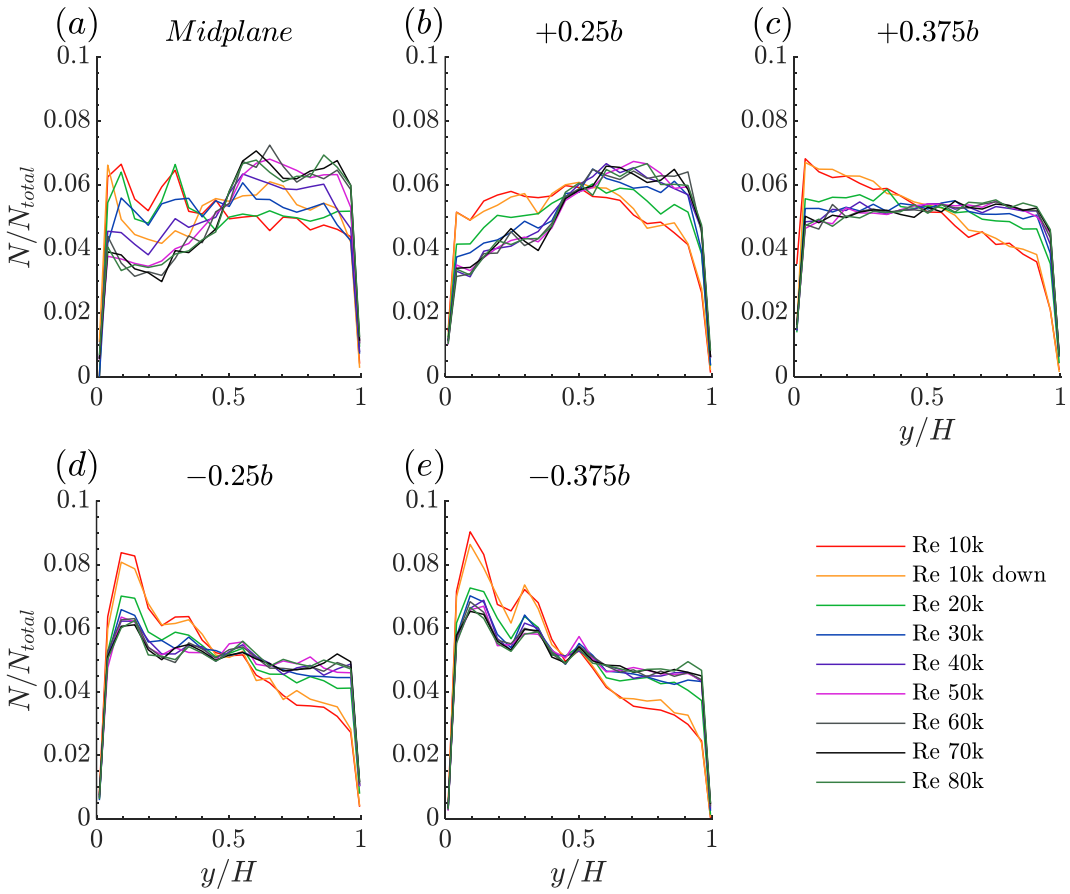

Figure 25: The normalized 420µm particle distribution plots with the laser pointing from the top.

5.1.5. Channel Upstream

Lastly, an additional set of data was collected with the camera and laser sheet positioned further upstream of the test section. The camera was focused on a section of the horizontal channel directly following the transition section of the flow loop. As the flow is just exiting the transition from a pipe cross section to a rectangular cross section, the flow has not yet become completely fully developed. For this reason, the observation of the behaviour of particles in this section is useful to observe whether trends such as preferential particle accumulation are present at different flow

regimes. For this test, the 1.2mm polystyrene particles were used to observe the flow. This decision was made since the side panels of this section are made of acrylic and are not clear like the glass panels of the test section, which makes observing the particles more difficult. Due to the slightly opaque nature of the acrylic, and cut lines on the panel, the smaller 420μm particles would show up distorted in the images, often showing up as streaks or lines instead of distinct particles. As a result, accurate particle detection and velocity calculations were not possible. To work around this, the larger 1.2mm particles were used because their size allowed the particle shape to show clearly through the acrylic panel and allow for sufficient particle detection. The larger size of the particles created a bigger contrast with the surrounding flow, making particle detection much more consistent. Again, in this case only a particle concentration of 0.1% was considered for the sake of brevity. If we compare Figure 26 to the initial 0.1% concentration plot of the 1.2mm particle test, it is shown that the particles are distributed much more evenly across the height of the channel, following the fact that they are approximately neutrally buoyant, with a small bias towards the bottom of the channel. The results of this comparison are like that of the offset locations, meaning that the laser being oriented above the channel here also results in more consistent particle detection across the channel height when compared to the initial measurements of the 1.2mm particles. There are only slight differences being that the initial test showed a bias towards the upper half of the channel, whereas here in the upstream case, across all Reynolds numbers there is a bias towards the bottom of the channel. In this instance there is a much larger number of detected particles as well, likely a result of the adjustments to the particle detection algorithm.

Figure 27 shows the same particle distribution normalized by the total number of detected particles. Again, we see that all the particles were distributed evenly across the channel height, with the only outliers being the cases where Re = 10 000, where the profile exhibits a wall-peaking shape. The

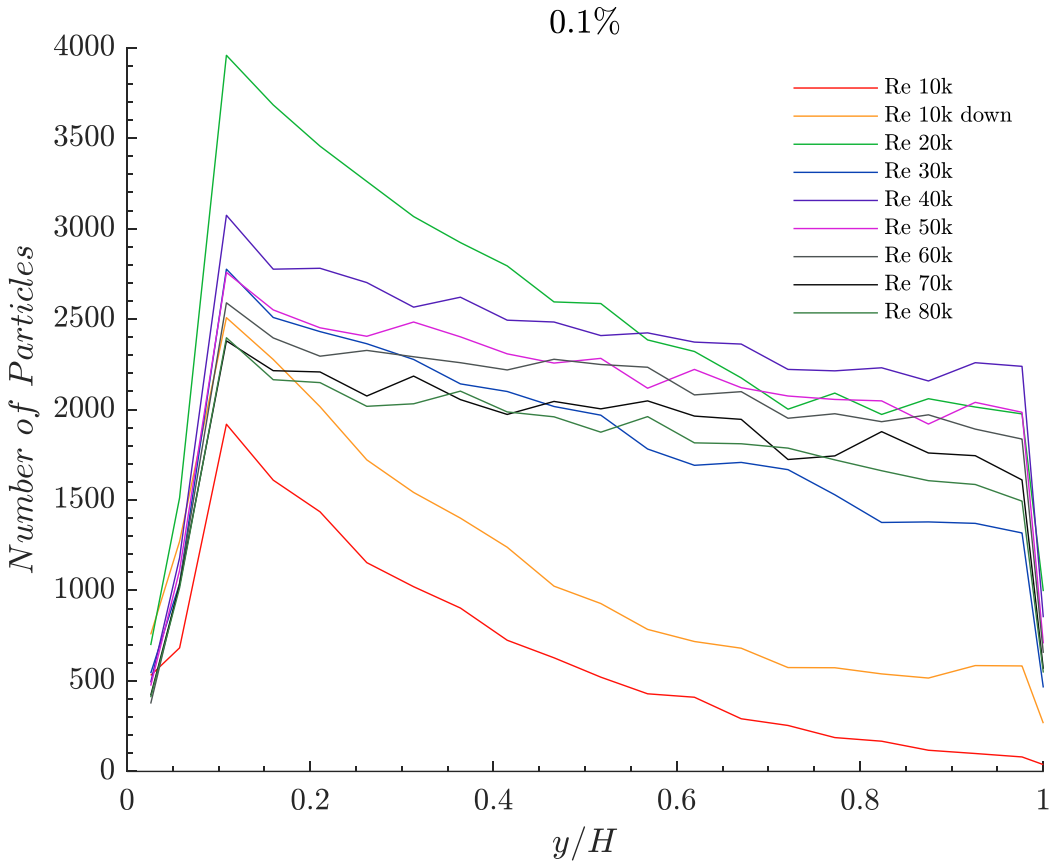

Figure 26: The particle distribution plot for the upstream channel section.

reason for this may be that the larger *St* of these particles means that they are influenced more slowly by changes in the fluid flow. Of note, this trend is also present in the initial 0.1% case where the 1.2mm particles were examined, shown previously in Figure 20 and Figure 21. By comparing the plots between Figure 21 and Figure 27, there are similarities among the lower Reynolds number scenarios. However, as previously stated in the test section the concentration profile shows a peak closer to the top of the channel, and here the concentration profile has a much flatter shape, showing good consistency with other observations in existing literature such as Zade et al (2018). Additionally, the slight bias of particles in the bottom wall may be a result of the fact that the flow is not fully developed in this section of the channel.

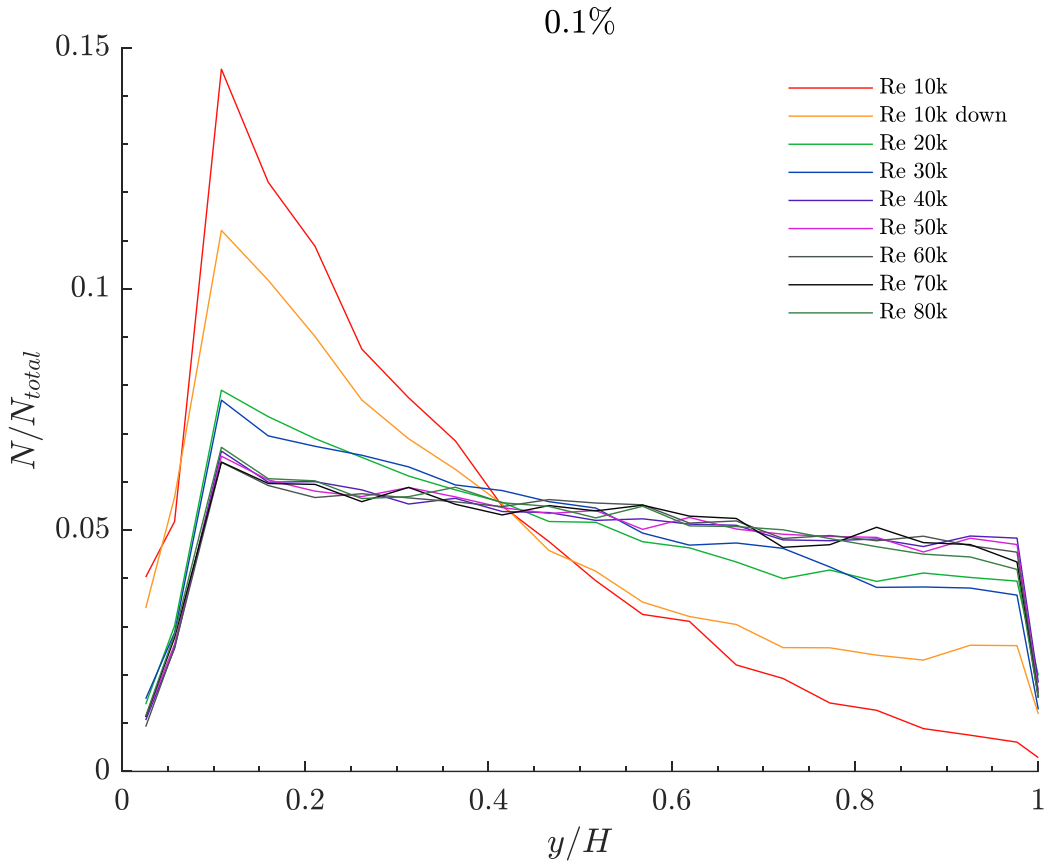

Figure 27: The normalized particle distribution plot for the upstream channel section.

5.2. Particle Laden Velocity Profiles

For all particle cases considered, the streamwise and wall-normal particle velocities were also determined using the MATLAB code. These velocities were calculated in pixels by measuring the displacement of the particles across the two image frames. Then the pixel displacement was converted into units of meters per second to plot the data in a presentable manner. This was done by discretizing the data across the wall-normal coordinate of the channel, and then calculating a moving average across each bin to produce a mean velocity profile. Next, the velocity profile was multiplied by the digital resolution of the image to convert the particle displacement from pixels

to meters, and divided by the time difference between frames to obtain the velocities in units of m/s. Like the particle distribution plots, the velocities were plotted against the normalized wall-normal coordinate, with 0 indicating the bottom of the channel, and 1 indicating the top of the channel. One complication with measuring the velocity this way is that it depends on consistent detection of particles and ensuring that the same particle is detected between frames 1 and 2. Of course, this is not always the case, and sometimes different particles are detected across frames, or possibly a particle is detected in one frame and not detected at all in the other. In these situations, it is not possible to calculate the velocity for that respective image pair, and as a result there are some instances where number of velocity data points are not high enough to be able to plot a smooth velocity profile. The root cause of this issue is the laser itself that was used, and the variation in power between the laser pulses for each frame resulting in the same particle being detected inconsistently between frames. Before collecting data at each concentration, a set of sample images were taken while adjusting the laser pulse intensity to try and obtain the most consistent image quality across both frames. It is not possible to verify the consistency of the laser power for each image pair, especially when the number of images required is 15000 image pairs, so some variation is expected. While this did help for most of the situations examined, there are still the occasional concentration cases where the number of detected velocity points is not enough to produce a smooth plot. Those cases will be discussed in this section as they appear.

The figures are organized similarly to Section 5.1, with the tests divided by particle type, then the subplots further divided by the particle concentrations. To validate the data, the velocity profiles should resemble a parabolic shape to indicate fully developed flow. The mean wall-normal velocities should be zero, indicating that there is no net flow in either the positive or negative y-direction. For cases where an asymmetric particle distribution is observed, for example a higher

particle concentration near the upper channel wall, it is useful to see if the wall-normal profiles are a possible contributor. If their magnitude is sufficiently small, then the particle concentrations would be the result of something else, such as particle-wall lubrication.

5.2.1. 420µm Polystyrene Particles

Once again, the first set of particles to be considered are the 420µm polystyrene particles. The streamwise velocity profiles for all concentrations considered are plotted in Figure 28. All three plots show parabolic profiles across all Reynolds numbers, indicating a fully developed flow. The data for the 0.5% case is less smooth compared to the other two cases, especially at the higher Reynolds number cases where Re = 70 000 and Re = 80 000. Particle detection at these higher velocities compared to others was slightly lower, and as a result less velocity points were able to be calculated. Having less data points makes it difficult to discretize the velocity across all the bins and means that a statistically significant average velocity could not be calculated for those bins considered, which results in a more jagged velocity profile. However, despite this, the overall trend of the streamwise velocity is still consistent with what is expected for fully developed flow. We can still observe a larger velocity at the centerline of the channel, with the magnitude of velocity reducing closer to the upper and lower walls, which is indicative of the no-slip boundary condition. When compared to the unladen velocity profiles explored in Section 4, we see that the shape as well as the maximum velocity between the examined Reynolds numbers are consistent. It is interesting to note that the shapes of the velocity profiles also generally follow the shape of the concentration profiles for the 0.1% and 0.3% cases. In other words, more particles were detected in the part of the channel where there is a higher velocity. This makes sense as the higher velocity means that more particles are moving through that part of the channel at any given time, meaning

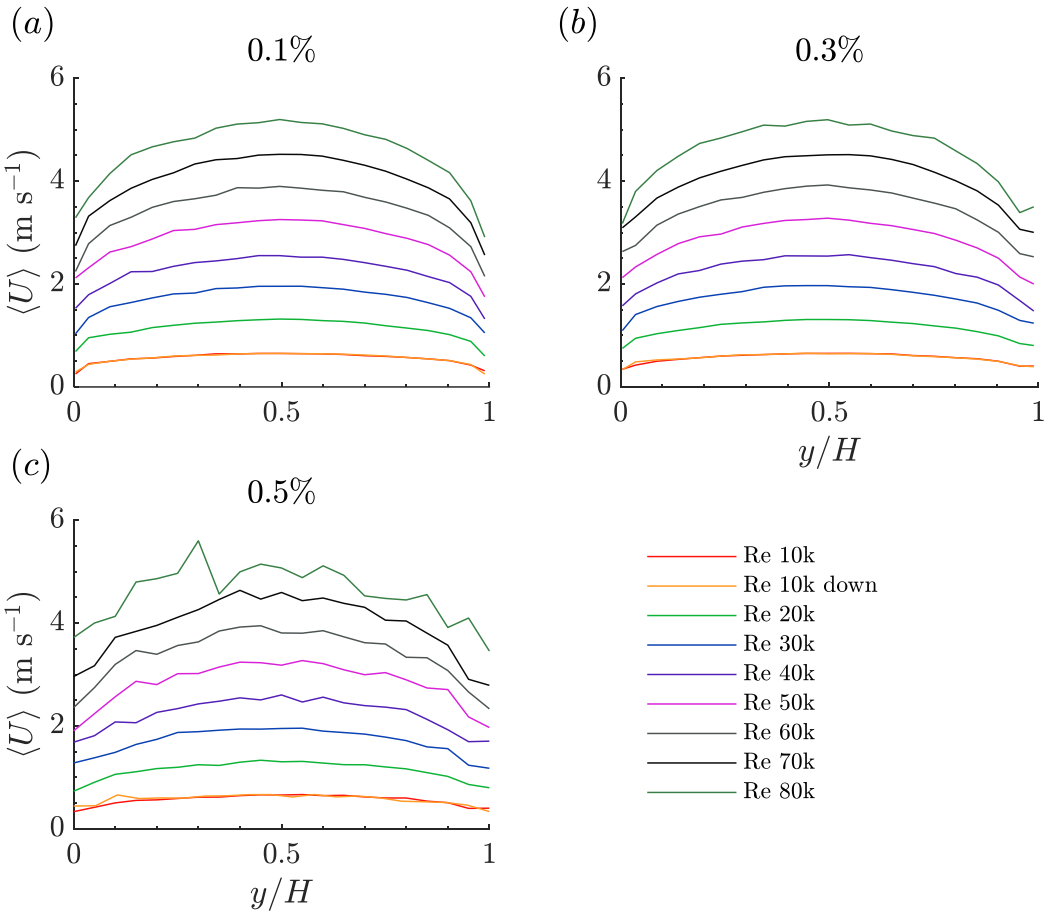

Figure 28: The streamwise velocity profiles for the 420µm particle case.

more are detected. For the 0.5% concentration case on the other hand, while the velocity profiles are symmetric about the channel center, the particle distribution is skewed towards the top of the channel. With no significant change present in the velocity profile, this may indicate that another mechanism is present at this higher concentration, which is causing the skewed particle distribution.

5.2.2. 1.2mm Polystyrene Particles

Figure 29 shows the streamwise velocity profiles for the 1.2mm particle case. The streamwise velocity profiles for the 0.1%, 0.3%, 0.5% and 0.7% concentration cases show good correlation

with the unladen flow profiles. Their shapes are parabolic affirming that the flow is fully developed. The velocity profiles between the two Re = 10 000 cases correlate well with each other for all concentrations, indicating that there is no permanent change in the flow properties as the measurements were taken. From the figure it is also evident that the resolution of the profiles drops at the higher particle concentrations cases of 0.9% and 1.1%, especially at the higher velocities. This is again since the velocities could not be consistently calculated for image pairs because of inconsistent particle detection among image frames. Particle detection at the 0.9% and 1.1% case is much lower at the higher velocities due to the water becoming murky and obstructing the particles from the camera. Even if the particles are visible in the image, the MATLAB code had difficulty detecting them because the intensity change between the particle and the background was so minimal. The number of velocity points that were able to be calculated for the 0.9% case where Re = 80 000 was so low that it could not even be discretized and plotted on the figure, hence the missing line in that case. This trend continues with the 1.1% concentration case, as the profiles for the higher Reynolds numbers are very inconsistent, and only slightly resembles the parabolic shape that is expected. Even with the sharp edges, an argument can be made that the slightly parabolic shape of the velocity profiles shows a consistent trend with the velocity profiles of the unladen flow, as well as the other particle laden cases. To rectify this issue for future measurements a higher laser power could be used to give more contrast between the particles and the flow, which would allow for increased particle detection at the higher concentrations.

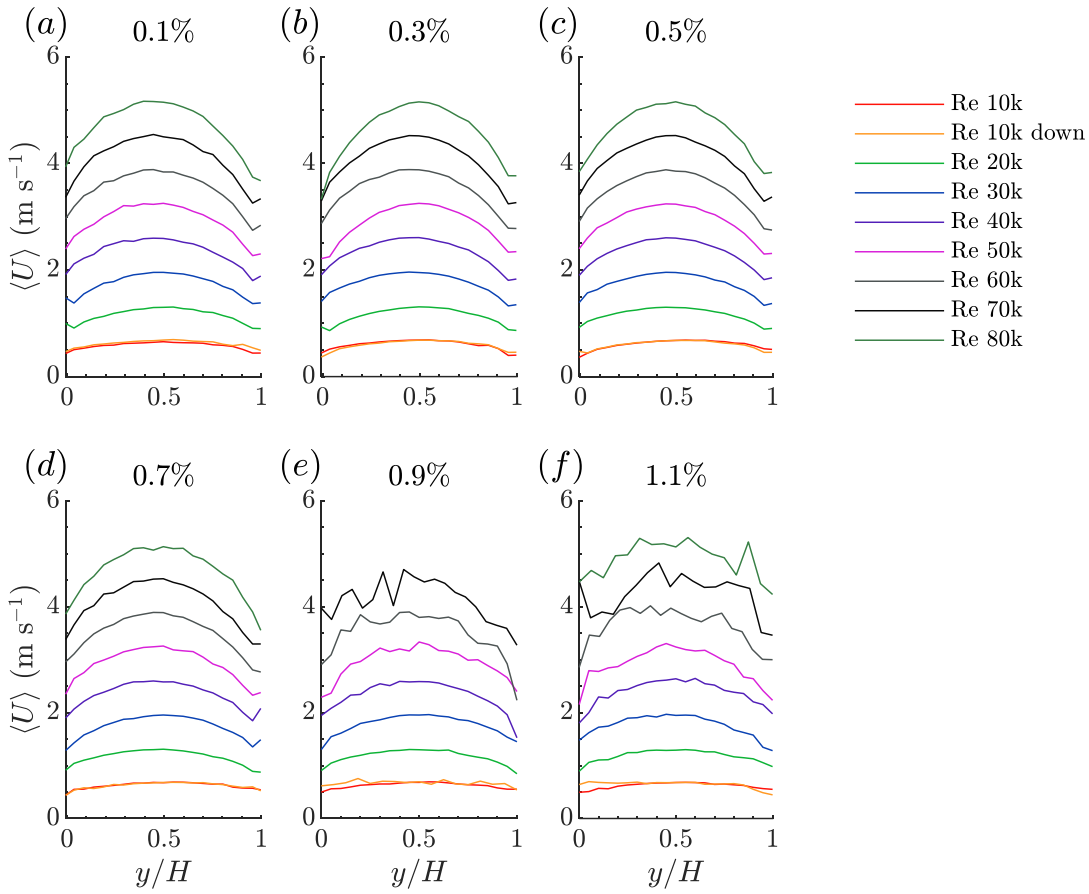

Figure 29: The streamwise velocity profiles for the 1.2mm particle case.

5.2.3. 420µm Glass Particles

The streamwise velocity profiles for the 420µm glass particles case are shown in Figure 30. From the figures it is shown that there is good correlation across the different concentrations, however these plots are distinctly less smooth when compared to the other particle cases. One obvious outlier is the case where Re = 50 000. In both the 0.1% and 0.3% concentration cases, there is a large spike in the profile near the top of the channel. The spike is not consistent with any of the distribution plots, and a velocity spike such as this is unrealistic in a channel flow and would have a noticeable effect on the particle statistics. Therefore, the most likely cause of the spike could be

an insufficient number of data points present to calculate the mean velocity of the discretized bin. Referring to the particle distributions in Figure 22, we can see that the number of detected particles for this case is very low near the top of the channel, meaning that there are less data points that can be used to calculate the velocity. We see this trend consistent across all profiles, leading to a reduced number of velocities in each bin that can be used to calculate the average velocity in that bin. Because of this, all the profiles are not smooth curves and show some inconsistency. Even with the jagged profiles, the overall profile shape for most Reynolds numbers somewhat resembles a parabola, with a maximum value near the channel center. The two cases where Re = 10 000 are also consistent with each other, indicating no permanent change in the flow as the Reynolds number is increased. As previously stated, these glass particles have a much higher density than water, so at the lower Reynolds numbers the particles tend to accumulate near the bottom of the channel, as is shown in Figure 23. As the velocities are calculated based on the movement of particles across the frames, the velocity profiles are not fully resolved in areas where there are not many particles, such as the top of the channel for most concentrations.

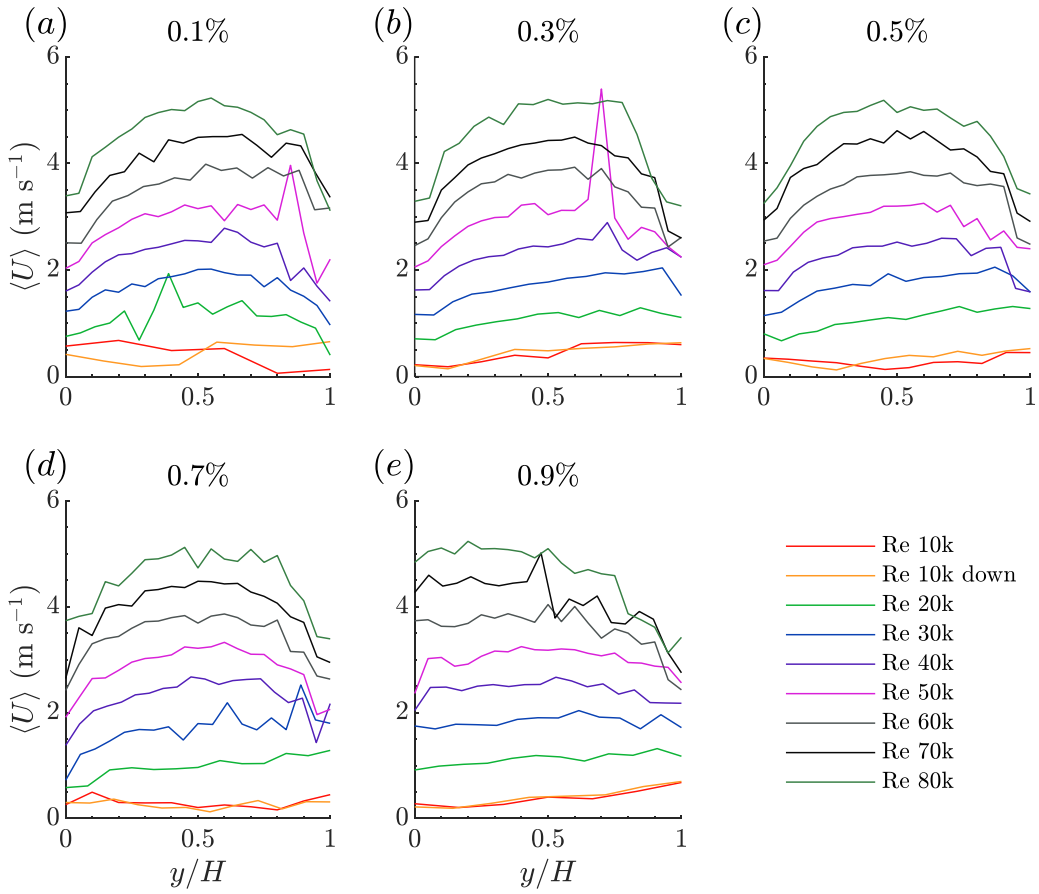

Figure 30: The streamwise velocity profiles for the 420µm glass particle case.

5.2.4. Effect of Measurement Location

Mean streamwise velocity profiles for the channel at the varying laser sheet positions are shown in Figure 31. Examining the velocity profiles across the spanwise direction of the channel is intended to verify that there is no crossflow in the channel, and that the flow can be considered a one-dimensional flow. The velocity profiles were examined at the same spanwise locations as the particle distribution plots and plotted against the normalized wall-normal location. From Figure 31 it is shown that the velocity profiles are consistent across the different offset positions, with similar profiles for all Reynolds numbers. This indicates that there is no net flow in the spanwise

direction, which affirms the fact that the flow is one-dimensional and only varies with the wall-normal position. It also shows that the flow loop used for these measurements can accurately depict the flow field of channel flow. The profiles are also all parabolic, meaning that the flow is fully developed across the entire width of the channel. Furthermore, the profiles are very smooth because the increased number of detected particles results in a larger number of calculated velocities. Because of this we can be confident that the average velocities calculated in each of the bins is statistically significant, and accurate with all the unladen flow profiles. One distinction among these profiles is that at both $\pm 0.375b$ cases the overall magnitude of the velocity is slightly smaller for each Reynolds number compared to the rest of the cases. This is most likely a result of the laser sheet being close to the wall in these cases. Thus, the detected particles that were used to calculate the velocity had a slightly slower magnitude of velocity due to the no-slip boundary condition at the wall.

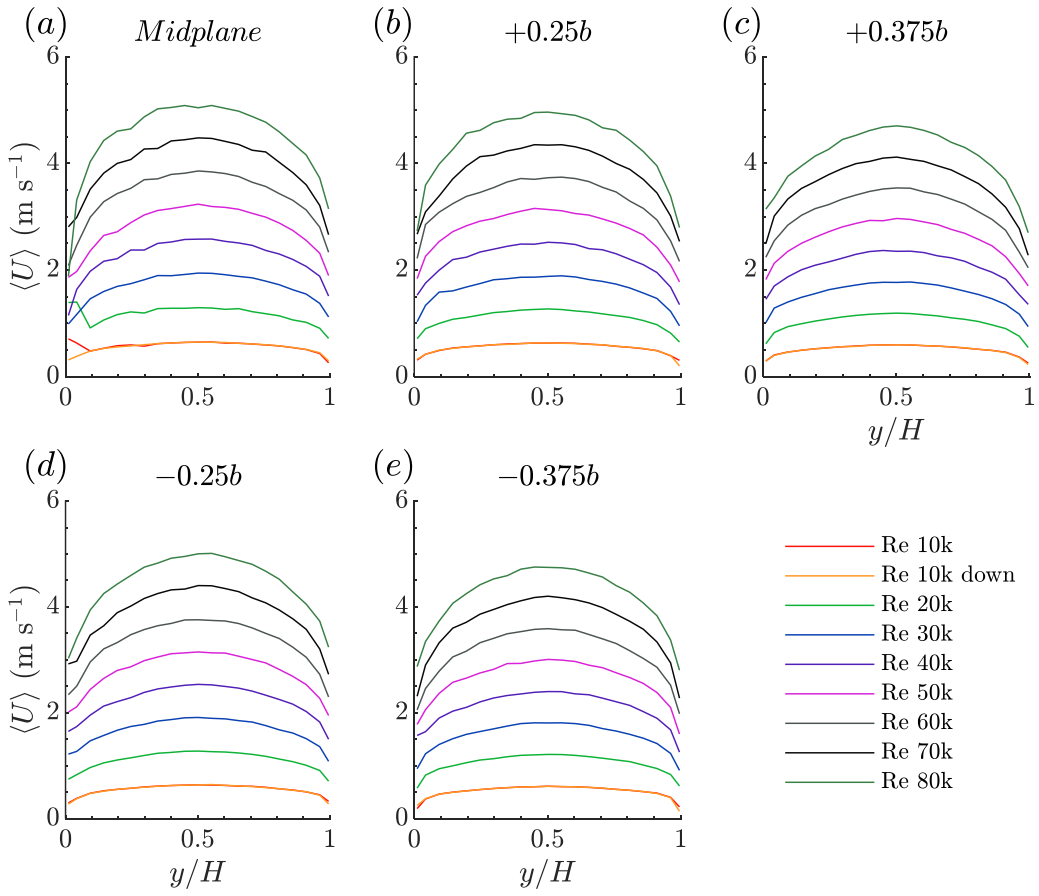

Figure 31: The streamwise velocity profiles for the 420µm particle case with the offset laser sheet positions.

5.2.5. Channel Upstream

Figure 32 shows the streamwise velocity profiles taken further upstream from the test section. This section of the channel follows directly after the transition section which changes the loop from a pipe cross section to a rectangular channel cross section. Across all Reynolds numbers, we see a consistent parabolic velocity profile. The only difference in this case is that the profiles are slightly flatter when compared to the streamwise velocity profiles within the test section. This is simply because the flow is not fully developed yet, meaning that the velocity statistics still vary with

respect to the *x*-direction. As the Reynolds number is increased, the profile begins to represent a fuller parabola indicating that the flow is closer to becoming fully developed at this point. The magnitude of the profiles here is also very close to the profiles within the test section. This means the transition section allows the flow to not be greatly disturbed because of the changing cross-section, allowing the flow to become fully developed again within a very short distance. Again, the two *Re* = 10 000 cases correlate very closely, showing no permanent change in the flow throughout the measurements.

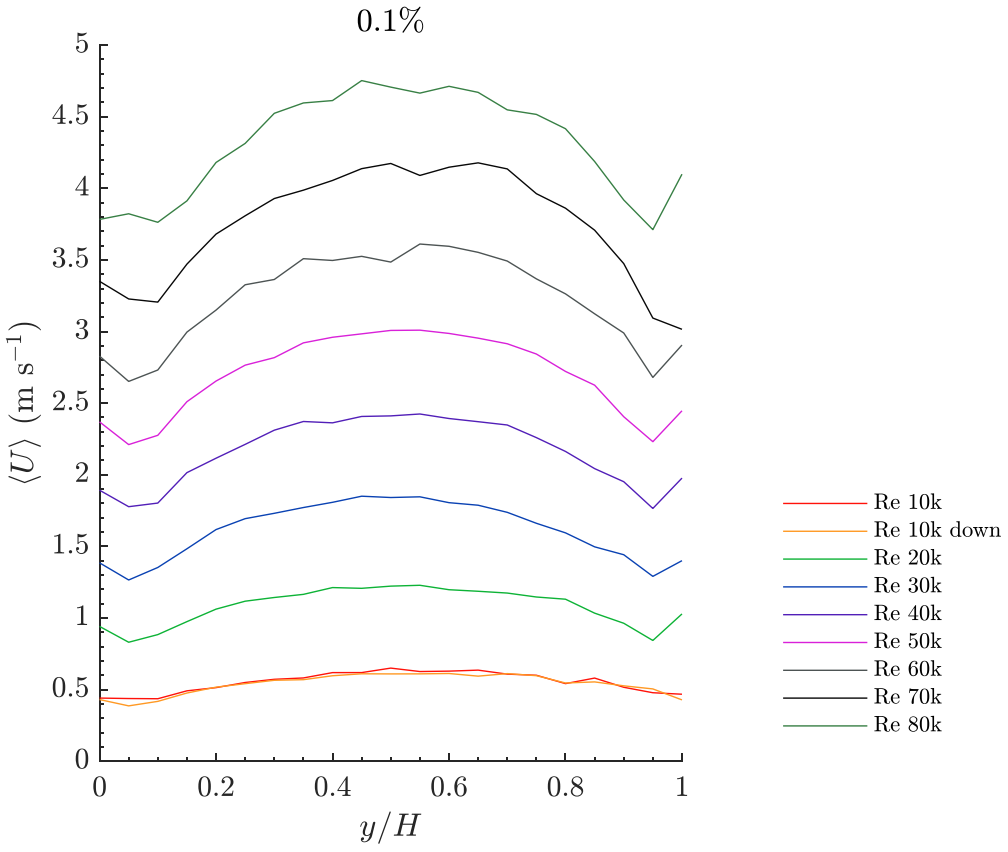

Figure 32: The streamwise velocity profiles of the upstream channel section.

5.2.6. Wall-Normal Velocity Profiles

Lastly the wall-normal velocity profiles are plotted for each of the respective particle cases. These profiles were calculated based on the average movement of the particles along the wall-normal direction. For the flows considered in this experiment the mean wall-normal velocity should be zero across the entire channel height, as the flow is considered one-dimensional flow and there should only be a velocity in the x-direction. Analyzing the wall-normal velocity for the cases where the particle distribution is biased towards one section of the channel is crucial to determine whether the cause of the skewed particle distribution is due to a net flow in the y-direction or for some other reason.

For all the cases considered, it is evident that the mean wall-normal velocity is very small, and thus does not significantly contribute to the motion of the particles towards the upper or lower channel walls. The variation observed in the following figures is only a result of the scale being zoomed in to see the different profiles. Overall, the magnitude of these profiles is not large enough to cause some net flow in the wall-normal direction. We can see this in Figure 33, which shows the wall-normal velocity profiles of the neutrally buoyant 420μm polystyrene particles. The 0.1% concentration is very close to zero, so we see an even distribution of the particles along the vertical coordinate of the channel. Alternatively, in the 0.3% case, the wall-normal velocity profiles increase positively as the Reynolds number also increases, so we should expect a slightly higher particle concentration near the top of the channel. Looking back at Figure 18, we can see this is not exactly the case, and that the particle distributions are symmetric about the channel centerline. The higher particle distribution in the 0.5% case at the top of the channel should make more sense with that type of profile, but we see here in Figure 33 that the profiles are only slightly positive above zero, indicating no significant velocity in the y-direction. Realistically, as previously stated

these magnitudes of wall-normal velocity are still very small, and thus it is unlikely that they may have caused a significant shift in the concentration profiles.

Similar trends are present across the 0.1%, 0.3%, and 0.5% concentration cases for the 1.2mm polystyrene particle size, shown in Figure 34. These profiles are all close to zero, with the profiles increasing in magnitude positively as the Reynolds number is increased. Moving to the 0.7% and 0.9% concentrations, the profile data is much less consistent and there are high spikes in the positive direction. Again, this high variance is due to the reduced particle detection at these concentrations, meaning that the mean velocities could not be accurately calculated for each bin. In the 1.1% concentration case, the profiles shown vary in both the positive and negative direction depending on the Reynolds number. For example, cases such as a Reynolds number of 20 000 or 30 000 are higher than zero, whereas cases such as 50 000 and 70 00 are below zero. While these profiles appear to be somewhat centered around zero, the trend of a net negative flow in the *y*-direction appears to only be present in this case. It is unlikely that the velocity profiles for this concentration are significantly different from the others, and the difference is most likely due to the insufficient number of velocity data points available to calculate a statistically significant mean wall-normal velocity. If we refer to the particle distribution plots in Figure 20, we can see that aside from a Reynolds number of 10 000, most of the particles for this 1.2mm case tend towards the top of the channel. All the profiles do not indicate a magnitude high enough to have a significant impact on particle concentration, and as a result this bias towards the top of the channel is likely due to the increased frequency of inter-particle collisions caused by turbulent fluctuations.

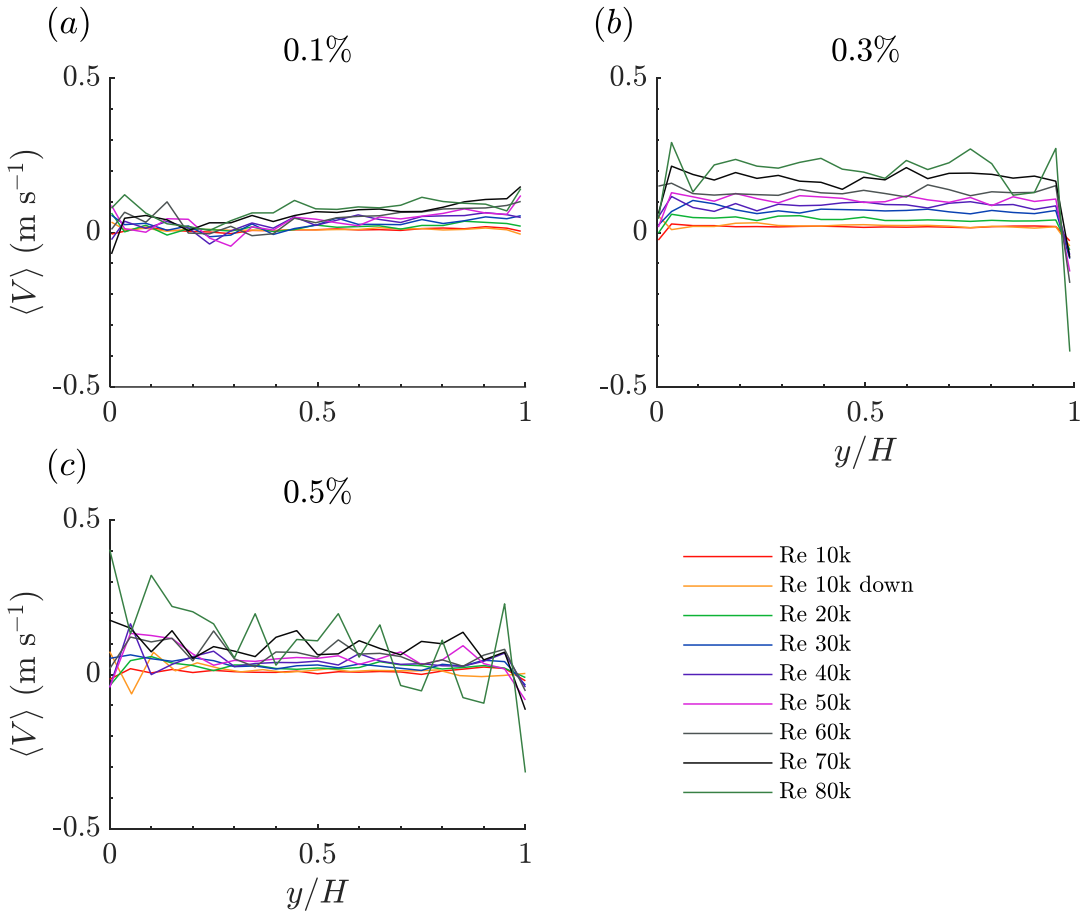

Figure 33: The wall-normal velocity profiles for the 420μm particle case.

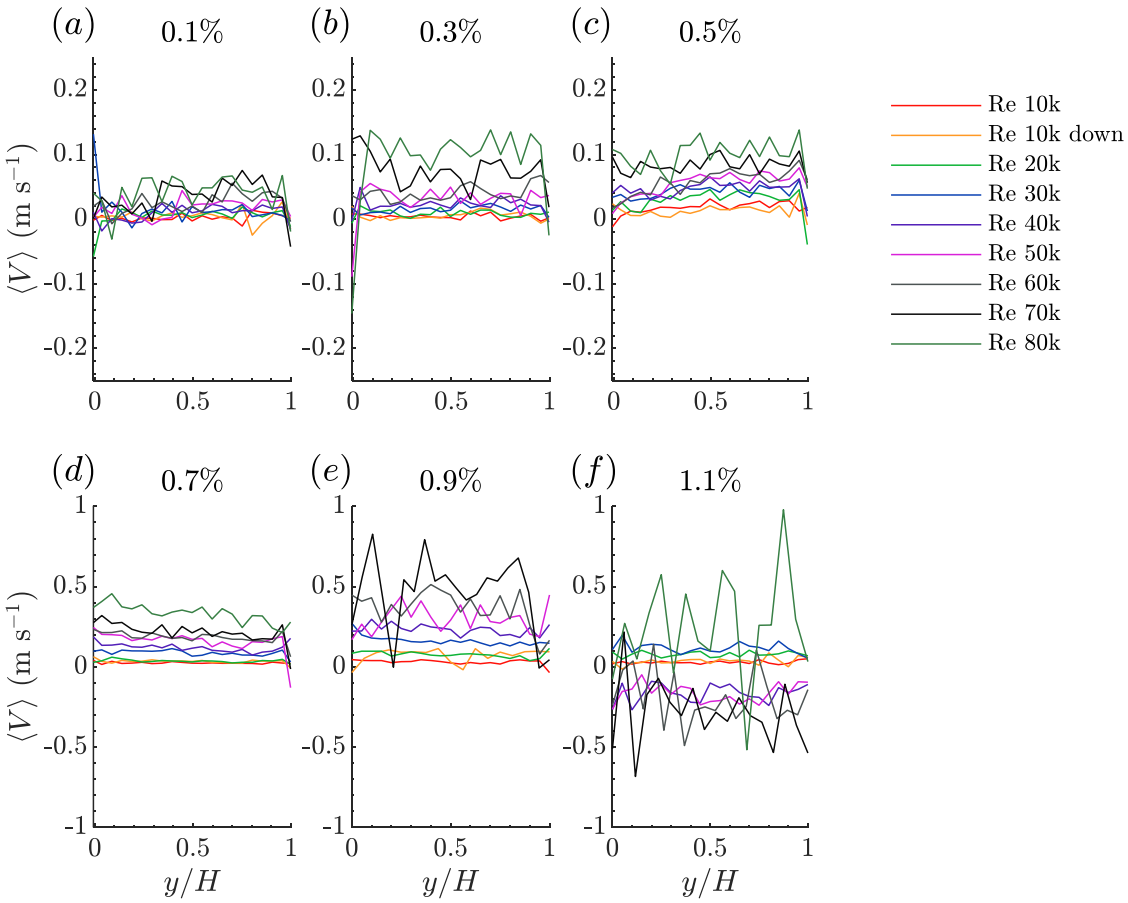

Figure 34: The wall-normal velocity profiles for the 1.2mm particle case.

Figure 35 shows the wall-normal velocities for the glass particle case. These plots exhibit much less variance for all concentrations compared to the other cases, with outliers primarily near the top of the channel. Again, this is due to the reduced number of particles not being detected in that region, and so sections of the profile show sharp peaks. Despite the sharp peaks in the profiles, they all are still centered closely around zero, which gives a strong indication that there is no net flow in the *y*-direction in this case either. One case that stands out is the 0.3% concentration case. While the mean velocity profiles suggest that there is no significant velocity in the positive or negative *y*-direction, the particle distribution plot in Figure 22 detects many of the particles near the bottom of the channel across all Reynolds numbers. These glass particles have a density which

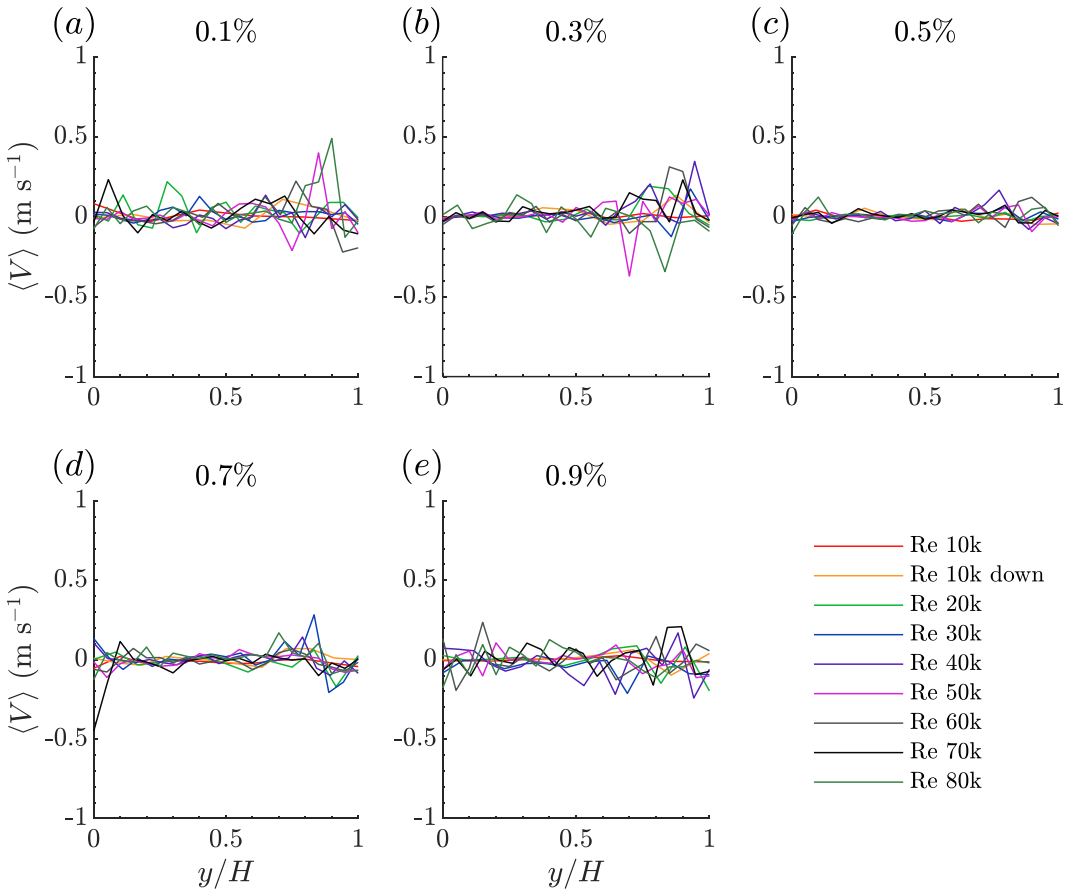

Figure 35: The wall-normal velocity profiles for the 420μm glass particle case.

is much higher than water, so while there is no net downward velocity, the particles are still heavy enough to accumulate near the bottom of the channel. One way to improve the detection of these particles would be to further refine the particle detection algorithm to detect particles more accurately across the channel. This could be done by further refining the laser intensities to be more consistent among different cases, and perhaps better control other sources of light pollution which may have been present and distorted some of the images.

Next the wall-normal velocity profiles for the 420μm particles with adjusted laser sheet positions were plotted. The concentration considered here is only 0.1%, so particle detection and velocity calculations were robust enough to obtain a relatively smooth velocity profile. These are shown in

Figure 36 with the same offsets being ±30mm (±0.25*b*) and ±45mm (±0.375*b*) in the *z*-direction from the midplane of the channel. As shown from the figure, across the entire span of the channel, all of the plots show a positive profile as the Reynolds number is increased. Again however, the magnitude of these profiles is not significant enough compared to the streamwise magnitudes to have a significant impact on the particle statistics. All the profiles are close to zero, representative of a one-dimensional flow. From the particle distribution plots shown previously for this case we see a slight increase in the number of particles at the top of the channel at the midplane and +0.25*b* cases, a relatively flat profile for the +0.375*b* case, and somewhat of an opposite trend with an increased number of particles near the bottom wall for the -0.25*b* and -0.375*b* cases. Because these magnitudes are so small, the preferential distributions of the particles are again likely caused by turbulent fluctuations along with inter-particle collisions.

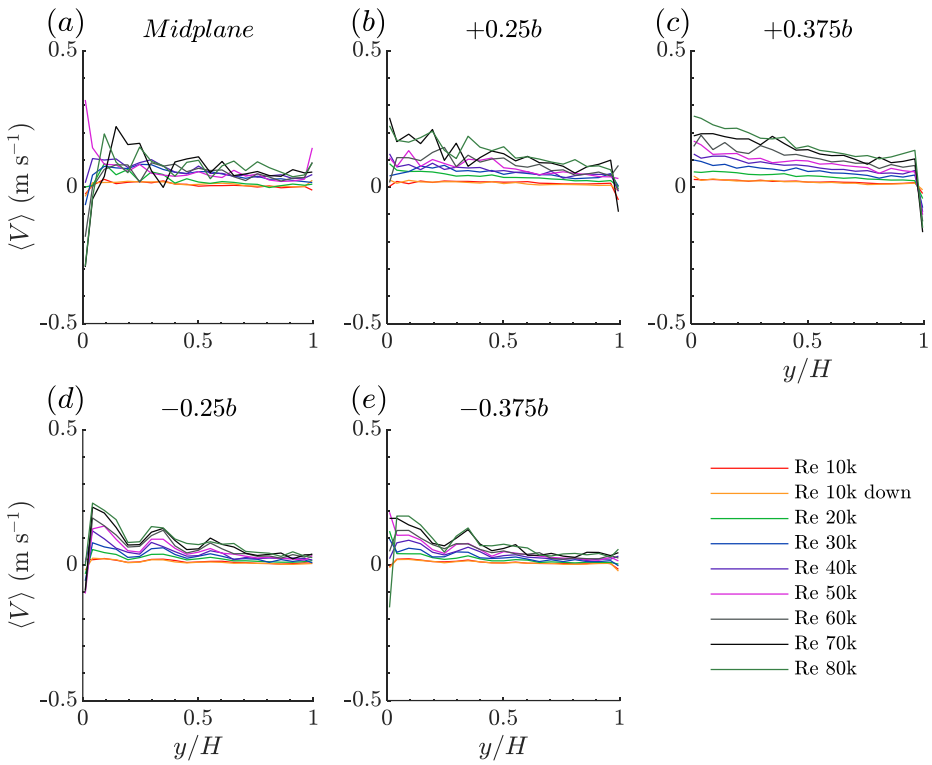

Figure 36: The wall-normal velocity profiles for the 420µm particle case with the offset laser sheet positions.

Finally, the last case considered is upstream channel case, shown in Figure 37. This case again only considered a concentration of 0.1% and is intended to observe the particle behavior before the flow is fully developed. From the figure it is shown that the wall-normal profiles are all centered around zero, with any deviations having a negligible magnitude. From Figure 27, the particle distribution is even across the channel height. Both factors can reinforce that the flow is one-dimensional, and the particles are not biased toward a particular direction in the near-fully developed regime.

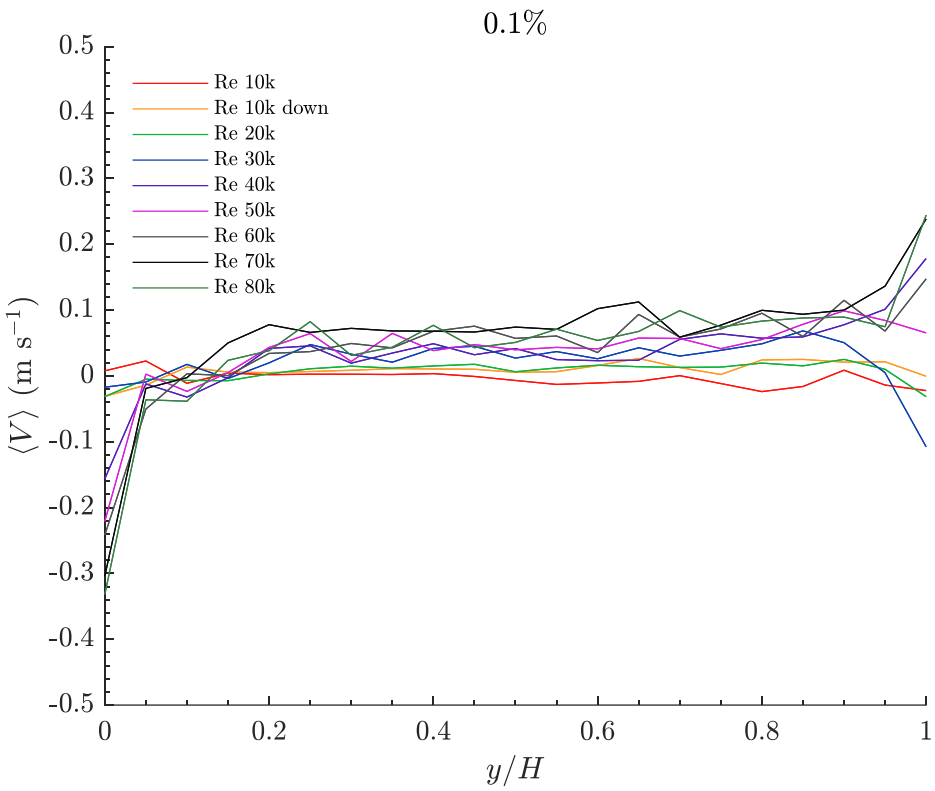

Figure 37: The wall-normal velocity profiles for the channel upstream section.

Looking at the profiles of the streamwise velocities for each scenario, there is good consistency between all the cases. The magnitude of the profiles is consistent across concentrations as well as particle types. When considering the offset profiles, the magnitude of the velocity is slightly reduced as the profiles move closer to the walls, due to the no-slip boundary condition at the walls. A smaller magnitude profile is also shown in the upstream location due to the profile not being fully developed at that location. All the wall-normal profiles show that there is negligible velocity in the wall-normal direction across all concentrations and particle types, which indicates that the flow is one-dimensional, which affirms the suitability of the flow loop for measurements of particle laden flows.

Chapter 6. Conclusion

This study was conduced to obtain a better understanding of the behavior of particle laden flows at various parameters, and additionally evaluate the suitability of the flow loop to conduct measurements of particle laden flows. Through the measurements collected in this investigation, it is shown that the particle type, concentration within the flow, as well as the location of the measurement domain in the channel, can influence the concentration profile. A total of three different types of particles were considered; 420µm polystyrene particles, 420µm glass particles, and 1.2mm polystyrene particles. Each particle type was immersed in the turbulent channel flow, and images were captured to obtain the particle distribution across the channel height. In addition, the velocity profiles for the particle laden flow were also calculated to ensure that the flow is one-dimensional. All the streamwise velocity profiles for the particle laden flows show a parabolic profile across all Reynolds numbers.

Starting with the 420µm particles, the concentration profiles followed a parabolic shape for all concentrations. These profiles were centered at the midplane of the channel for the 0.1% and 0.3% cases. However, at the higher concentration of 0.5% the profile peak is biased towards the top of the channel. Existing literature show that neutrally buoyant particles should have a relatively flat profile across the channel height, so this deviation could be the result of particle-wall lubrication. One interesting observation of the 0.3% and 0.5% cases are that the overall number of detected particles decreased as *St* increased. Increasing the power of the laser or adjusting the detection algorithm could help rectify this issue by making the particles easier to detect at the higher Stokes numbers. The 420µm particles were also examined at various locations across the span (*z*-axis) of the channel at a concentration of 0.1%. These observations were done with the laser pointing down

from above the channel, as opposed to the bottom of the channel with which the first test was conducted. Overall, in this scenario, all the observed profiles showed a much flatter concentration profile, indicating that the laser orientation influences particle detection. There is only some slight deviation when the laser sheet is moved closer to the camera, as the concentration profile becomes slightly biased towards the bottom of the channel across all *St*. These observations show that observations should be made with the laser oriented above the channel to obtain the most consistent results.

The larger 1.2mm polystyrene particles observed with the laser sheet pointing up from the bottom of the channel have a relatively uniform concentration profile at the lower concentrations. At the lower Reynolds number, the profile peaks at the bottom wall due to increased gravitational settling caused by the higher Stokes numbers. As the concentration is increased to 0.5% or higher, the concentration profile peak shifts towards the top of the channel as *St* increases. The shift in the profile peak could again be indicative of particle-wall lubrication, like the smaller polystyrene particles, causing them to accumulate near the wall. Observations of the 1.2mm polystyrene particles in the upstream channel shows a relatively uniform profile for all Stokes numbers, indicating good consistency with existing literature. A slight bias at the bottom wall could be the result of the flow here not being fully developed, and as such the flow does not have enough momentum to lift the particles off the bottom of the channel.

For the observations obtained for the glass particles, the concentration profiles showed a significant bias of particles accumulating near the bottom wall across all concentrations. It is only at the higher *St* that the concentration profile does start to shift and moves the concentration peak closer to the channel center. This behaviour makes sense as the glass particles' higher density results in an increase in the particles settling due to gravity, and it is only because of the increase

of turbulent fluctuations that occur at the higher flow velocities that the profile peak moves further away from the wall. As the Stokes number is reduced the glass particles settle to the bottom of the channel almost immediately. The 0.3% concentration case is a unique case as the profile shapes here are different comparted to the other concentrations. Despite this, the general trend of a large peak at the wall which reduces as the *St* is increased is still present here. This trend is consistent with observations of existing literature, with the movement of the particles here being heavily influenced by the Reynolds number.

The observations obtained in this thesis suggest that the concentration profiles are affected by the orientation of the laser, as well as the location of the measurement domain in the channel. For both sizes of polystyrene particles, at higher concentrations and larger *St,* a general trend of particles accumulating near the top wall of the channel as *Re* increases was observed. This behavior has been observed in existing literature as cases of particle-wall lubrication, which can cause a layer of particles to be trapped in the near wall region. Additionally for the glass particles, inconsistencies were observed with the shape of the 0.3% concentration profile, but the remaining profiles showed good correlation with other experiments, with the profiles becoming less wall-peaking as *St* was increased. These observations were also intended to validate the suitability of the flow loop for the use of measuring particle laden flows. Based on the results obtained, there is good correlation with the profile shapes obtained here and the behaviour of particles observed and discussed in existing literature. Some improvements can still be made to further optimize the particle detection to help in obtaining better results, but the data collected is still consistent. Therefore, the flow loop apparatus used here is determined to be suitable for the measurements of particle laden flows.

Future Work

When considering future examination into this subject, some recommendations can be made to improve on the current work. The largest area of improvement based on the observations obtained here are improvements to the measurement system. Ensuring that the laser intensity is more consistent between frames as well as more constant across the height of the channel will allow for more consistent particle detection. The particle detection was one of the main sources of measurement error in this experiment and so fixing that would result in more consistent concentration profiles across all particle types. In the case examining the concentration profile across the width of the channel, only one concentration and particle type was considered here. Using the larger polystyrene particles as well as increasing the concentration for both particle types can be useful to observe if the same trend is present at the different locations. Also, this scenario would increase the understanding of the particle behavior in the near wall region, and whether the wall peaking profile is also present at higher concentrations. Another extension of this study could be to consider other particle types or shapes. This may include other materials, such as hydrogels, or particle shapes such as oblate spheroids. The particles within most particle laden flows in industry are likely not spherical in nature, so the understanding of differently shaped particles would be of great interest.

References

[1] Aggarwal, Suresh, Y. Xiao, and J. Uthuppan. “EFFECT OF STOKES NUMBER ON PARTICLE DISPERSION.” Atomization and Sprays 4, no. 2 (1994): 223–36.

[2] Ahmadi, Farzad, R. Sean Sanders, and Sina Ghaemi. “Spatial Distribution of Particles in Turbulent Channel Flow of Dilute Suspensions.” *International Journal of Multiphase Flow* 135 (February 2021): 103538. https://doi.org/10.1016/j.ijmultiphaseflow.2020.103538.

[3] Baker, Lucia J., and Filippo Coletti. “Experimental Study of Negatively Buoyant Finite-Size Particles in a Turbulent Boundary Layer up to Dense Regimes.” *Journal of Fluid Mechanics* 866 (May 10, 2019): 598–629. https://doi.org/10.1017/jfm.2019.99.

[4] Çengel, Yunus A., and John M. Cimbala. *Fluid Mechanics: Fundamentals and Applications*. Third edition. New York: McGraw Hill, 2014.

[5] Dabiri, Dana. “Cross-Correlation Digital Particle Image Velocimetry – A Review,” n.d.

[6] Dai, Wei, Selen Cremaschi, Hariprasad J. Subramani, and Haijing Gao. “Uncertainty Quantification in Erosion Predictions Using Data Mining Methods.” *Wear* 408–409 (August 2018): 108–19. https://doi.org/10.1016/j.wear.2018.05.009.

[7] Das, Prashant, and Sina Ghaemi. “Light-Scattering of Tracer Particles for Liquid Flow Measurements.” *Measurement Science and Technology* 32, no. 6 (June 1, 2021): 065302. https://doi.org/10.1088/1361-6501/abf25c.

[8] Dean, R. B. “Reynolds Number Dependence of Skin Friction and Other Bulk Flow Variables in Two-Dimensional Rectangular Duct Flow.” Journal of Fluids Engineering 100, no. 2 (June 1, 1978): 215–23. https://doi.org/10.1115/1.3448633.

[9] Durham, Michael D., and Dale A. Lundgren. “Evaluation of Aerosol Aspiration Efficiency as a Function of Stokes Number, Velocity Ratio and Nozzle Angle.” *Journal of Aerosol*

Science 11, no. 2 (January 1980): 179–88. https://doi.org/10.1016/0021-8502(80)90033-6.

[10] Fong, Kee Onn, Omid Amili, and Filippo Coletti. "Velocity and Spatial Distribution of Inertial Particles in a Turbulent Channel Flow." *Journal of Fluid Mechanics* 872 (August 10, 2019): 367–406. https://doi.org/10.1017/jfm.2019.355.

[11] Fornari, W., A. Formenti, F. Picano, and L. Brandt. "The Effect of Particle Density in Turbulent Channel Flow Laden with Finite Size Particles in Semi-Dilute Conditions." *Physics of Fluids* 28, no. 3 (March 2016): 033301. https://doi.org/10.1063/1.4942518.

[12] Gillissen, J. J. J. "Turbulent Drag Reduction Using Fluid Spheres." *Journal of Fluid Mechanics* 716 (February 10, 2013): 83–95. https://doi.org/10.1017/jfm.2012.510.

[13] Hamdi, M., M. Havet, O. Rouaud, and D. Tarlet. "Comparison of Different Tracers for PIV Measurements in EHD Airflow." *Experiments in Fluids* 55, no. 4 (April 2014): 1702. https://doi.org/10.1007/s00348-014-1702-z.

[14] Johnson, Perry L. "Predicting the Impact of Particle-Particle Collisions on Turbophoresis with a Reduced Number of Computational Particles." *International Journal of Multiphase Flow* 124 (March 2020): 103182. https://doi.org/10.1016/j.ijmultiphaseflow.2019.103182.

[15] Knight, Donald W., and Harish S. Patel. "Boundary Shear in Smooth Rectangular Ducts." *Journal of Hydraulic Engineering* 111, no. 1 (January 1985): 29–47. https://doi.org/10.1061/(ASCE)0733-9429(1985)111:1(29).

[16] Kundu, Pijush. "Fluid Mechanics Fifth Edition." In Fluid Mechanics, ix. Elsevier, 2012. https://doi.org/10.1016/B978-0-12-382100-3.10023-X.

[17] Picano, Francesco, Wim-Paul Breugem, and Luca Brandt. "Turbulent Channel Flow of Dense Suspensions of Neutrally Buoyant Spheres." *Journal of Fluid Mechanics* 764 (February 10, 2015): 463–87. https://doi.org/10.1017/jfm.2014.704.

[18] Pope, Stephen B. Turbulent Flows. Cambridge, UK: Cambridge University Press, 2000.

[19] Rhodes, David G., and Donald W. Knight. “Distribution of Shear Force on Boundary of Smooth Rectangular Duct.” *Journal of Hydraulic Engineering* 120, no. 7 (July 1994): 787–807. https://doi.org/10.1061/(ASCE)0733-9429(1994)120:7(787).

[20] Sciacchitano, A. “Uncertainty Quantification in Particle Image Velocimetry.” *Measurement Science and Technology* 30, no. 9 (September 1, 2019): 092001. https://doi.org/10.1088/1361-6501/ab1db8.

[21] Tien, Chi, and B.V. Ramarao. “MECHANISMS OF PARTICLE DEPOSITION.” In *Granular Filtration of Aerosols and Hydrosols*, 117–68. Elsevier, 2007. https://doi.org/10.1016/B978-185617458-9/50005-1.

[22] Vinuesa, Ricardo, Eduard Bartrons, Daniel Chiu, Jean-Daniel Rüedi, Philipp Schlatter, Aleksandr Obabko, and Hassan M. Nagib. “On Minimum Aspect Ratio for Experimental Duct Flow Facilities.” In *Progress in Wall Turbulence 2*, edited by Michel Stanislas, Javier Jimenez, and Ivan Marusic, 23:201–11. ERCOFTAC Series. Cham: Springer International Publishing, 2016. https://doi.org/10.1007/978-3-319-20388-1_18.

[23] Westerweel, J. “Fundamentals of Digital Particle Image Velocimetry.” *Measurement Science and Technology* 8, no. 12 (December 1, 1997): 1379–92. https://doi.org/10.1088/0957-0233/8/12/002.

[24] Young, John, and Angus Leeming. “A Theory of Particle Deposition in Turbulent Pipe Flow.” *Journal of Fluid Mechanics* 340 (June 10, 1997): 129–59. https://doi.org/10.1017/S0022112097005284.

[25] Zade, Sagar, Fredrik Lundell, and Luca Brandt. “Turbulence Modulation by Finite-Size Spherical Particles in Newtonian and Viscoelastic Fluids.” arXiv, November 28, 2018.

http://arxiv.org/abs/1811.11824.

[26] Zanoun, E.-S., F. Durst, and H. Nagib. “Evaluating the Law of the Wall in Two-Dimensional Fully Developed Turbulent Channel Flows.” *Physics of Fluids* 15, no. 10 (2003): 3079. https://doi.org/10.1063/1.1608010.

[27] Zeng, Yue, Zhuang Ma, and Yan Feng. “Determination of Best Particle Tracking Velocimetry Method for Two-Dimensional Dusty Plasmas.” *Review of Scientific Instruments* 93, no. 3 (March 1, 2022): 033507. https://doi.org/10.1063/5.0073342.